UNIVERSITY OF SOUTHAMPTON

FACULTY OF PHYSICAL AND APPLIED SCIENCES
Physics and Astronomy

Mesoscopic Transport and Control of Light through Disordered Nanowire Mats

by

Thomas I. Strudley

Thesis for the degree of Doctor of Philosophy

August 2014

UNIVERSITY OF SOUTHAMPTON

ABSTRACT

FACULTY OF PHYSICAL AND APPLIED SCIENCES
Physics and Astronomy

Doctor of Philosophy

MESOSCOPIC TRANSPORT AND CONTROL OF LIGHT THROUGH DISORDERED NANOWIRE MATS

by Thomas I. Strudley

In this thesis the transport of light through disordered, densely packed semiconductor nanowire mats is studied. It is found that the extremely high photonic strength of these samples leads to corrections to the traditional diffusion picture of light transport due to mesoscopic interference. Such effects are characterised by large intensity fluctuations and correlations, and it is found the transport is dominated by only a few independent transmission channels, close to the Anderson localisation regime. In addition to the strongly scattering nanowire samples, comparatively weakly scattering samples of ZnO are investigated, demonstrating mesoscopic effects in a less exotic, isotropic multiple scattering material. Control is obtained over the transmission by a combination of shaping the incident wavefront and harnessing the intrinsic nonlinearity of the semiconductor with ultrafast optical excitation.Through these techniques, a bright focus at an arbitrary point through the nanowires is created which can be modulated by up to 60% in a demonstration of a reconfigurable photonic switch.

Contents

List of Figures

List of Tables

Declaration of Authorship

I, Thomas I. Strudley , declare that the thesis entitled *Mesoscopic Transport and Control of Light through Disordered Nanowire Mats* and the work presented in the thesis are both my own, and have been generated by me as the result of my own original research. I confirm that:

- this work was done wholly or mainly while in candidature for a research degree at this University;
- where any part of this thesis has previously been submitted for a degree or any other qualification at this University or any other institution, this has been clearly stated;
- where I have consulted the published work of others, this is always clearly attributed;
- where I have quoted from the work of others, the source is always given. With the exception of such quotations, this thesis is entirely my own work;
- I have acknowledged all main sources of help;
- where the thesis is based on work done by myself jointly with others, I have made clear exactly what was done by others and what I have contributed myself;
- parts of this work have been published as: [2],[3],[4]

Signed:..

Date:..

Acknowledgements

The work in this thesis would not have been possible without the contributions of many different people. First, I would like to thank my supervisor Prof. Otto Muskens for his patient advice, assistance and many late hours in the lab. Without his contributions this thesis would not exist, and I am very grateful for being given the opportunity to do some exciting science. Thanks must also go to the examiners for my viva, Prof. Hendrik Ulbricht and Prof. Juan Jos Senz, both for their time and for their suggestions which have really helped to improve this thesis.

During my PhD, I have been fortunate to be part of two productive collaborations in the Netherlands. The nanowires used in this project were grown by Tilman Zehender in the group of Prof. Erik Bakkers at Eindhoven university over the course of two visits, and the work done in this thesis would not have been possible without their expertise. Thanks must also go to W.G.G. Immink at the Phillips High Tech Campus in Eindhoven for his assistance with the nanowire growth. The other collaboration was with Duygu Akbulut and Prof. Allard Mosk of the Complex Nanophotics group at the University of Twente, during which promising wavefront shaping experiments were made. The many discussions and the knowledge gained from this collaboration was invaluable in performing the wavefront shaping experiments in this thesis.

It has been a pleasure to work with Dr. Roman Bruck on the ultrafast wavefront shaping experiments in this thesis. These experiments were carried out using the FAST Lab laser facilities of the Optoelectronics Research Center (ORC), and the contribution of Dr. Ben Mills of the ORC in developing the wavefront shaping setup and assistance with the laser facilities is gratefully acknowledged. My limited work in the clean room would not have been possible without the assistance of Zondy Webber, and thanks must also go to Rute Fernandes and Amelie Heuer-Jungemann for their assistance with the etching of the Gallium Phosphide wafers used for the growth of the nanowires in this project.

I must also add thanks to all of my friends and fellow group members for making the past three and a half years as enjoyable as they have been. It has always been a pleasure coming into work in the morning, and I am already missing the friday Crown lunches. Finally, I would like to thank my parents for all of their support and wise words, and my best friend Hollie for making me so happy even during the inevitable stressful times.

Thomas Strudley, June 2014

Chapter 1

Introduction

1.1 Disordered Photonics

According to the United Nations, 2015 will be the 'International year of light and light-based technologies' [5], recognising the increasingly important role of photonics to society. Our understanding of how light interacts with matter underpins a whole range of applications including medical imaging, telecommunications and photovoltaics. Understandably, the vast majority of devices are based on precisely designed, ordered structures through which the propagation of light is predictable. The presence of disorder in such systems is considered detrimental to performance, and great advances have been made minimise or compensate for naturally occurring randomness. While this approach has been the basis of many technological advances so far, there is growing interest in harnessing the effects of disorder instead of fighting against it [6].

So why is disorder interesting? While light can pass through random multiple scattering media such as skin or a layer of white paint, they appear opaque because over several scattering events any information about objects behind or within the layer is scrambled. Consequently, the most recognisable feature of coherent light propagating through such a medium is the seemingly chaotic distribution of intensities known as a 'speckle pattern' arising from the interference of many light paths of different lengths. Originally considered a limiting factor in the use of lasers for imaging, speckle in fact conserves a surprisingly large amount of information. One example of this is the so called 'memory effect' [7], a short range correlation in which the original direction of the incident light is remembered even after a large number of scattering events. Recently this property has been used to image objects concealed behind an opaque screen [8, 9].

The ability to image and focus light through disordered media is of great interest, especially the prospect of using lasers for medical diagnosis and treatment. This is possible because the elastic multiple scattering process does not destroy information, and due to reciprocity, it should be completely reversible. As long ago as 1966, this property was exploited using optical phase conjugation to retrieve an image transmitted through a diffusive medium [10]. More recently, considerable advances have been made in time reversal experiments using acoustic [11, 12], electromagnetic [13, 14] and even water [15] waves. In these studies the complex wavefront generated by the multiple scattering process is recorded, inverted, then played back to recreate the original source.

A closely related approach is to find the transmission matrix coupling the incident and outgoing fields to the medium. If the transmission matrix is known it is, in principle, possible to compensate for the scrambling effect of the medium by controlling the incident wavefront. Naturally, calculating the transmission matrix of a real multiple scattering sample is a daunting task. However, great advances have been made in recent years using spatial light modulators to control the transmission through random media without prior knowledge of the transmission matrix. By monitoring the outgoing light from the medium while iteratively changing the incident wavefront, it is possible to create a sharp focus at an arbitrary point that can exceed the diffraction limit for traditional optics in so called 'perfect focusing' [16, 17]. By the same approach the total transmission can be increased by coupling only to modes with high transmission coefficients [18, 19] and the transmission matrix itself can be measured [20, 21]. The ability to measure the transmission matrix means that the disordered photonic media hold great promise as reconfigurable optical devices [22, 23].

Due to the random walk like nature of diffusion, light can be trapped within a disordered structure for a relatively long time. This property is of considerable interest in the development of photovoltaics, as the trapping of light close to the active material in solar cells can improve efficiency [24]. Another notable developing field harnessing this property is that of random lasers, in which a disordered collection of scatterers is used to confine light within a gain medium instead of a traditional cavity [25]. The principle advantage of this technique is the potential to easily and cheaply create small, robust lasers. While the initial output from such devices is random, it has been shown that by applying wavefront shaping techniques to the pump light it is possible to control the selection of both spatial and spectral lasing modes [26, 27].

As well as the relatively recent interest for applications, the effect of disorder on wave propagation has long been a subject of more fundamental studies. For sufficiently high scattering strength, the classical diffusion picture of wave transport breaks down and several new interesting phenomena can occur. Perhaps the most well known of these mesoscopic effects is that of Anderson Localisation, in which diffusion is completely halted by disorder. The term 'mesoscopic' refers to physics at the interface between the classical and quantum worlds, and it is more commonly encountered in the field of solid state electronics. Indeed, Anderson Localisation was first proposed as a new conductor-insulator transition for electrons propagating in disordered conductors in 1958 [28].

The underlying physics of mesoscopic effects is that of interference, which is equally applicable to classical wave propagation [29]. Anderson Localisation has been observed in many different classical systems including acoustic waves [30], microwaves in quasi-one dimensional (Q1D) waveguides [31], cold atom systems [32], and light in one and two dimensions [33–35]. However, conclusive demonstration of Anderson Localisation of light in 3D remains somewhat of a holy grail of mesoscopic physics. Several pioneering studies have reported its observation [36–38]. However, effects such as absorption can mimic those of localisation [39] and some debate remains of the interpretation of the results and whether localisation of light is even possible [40] in three dimensions.

1.2 Thesis outline

In this thesis, light propagation through densely packed disordered mats of semiconductor nanowires is investigated. Such samples exhibit two properties of interest: they are amongst the strongest optically scattering materials available, and are intrinsically non-linear due to their semiconductor composition. In the last section of this chapter the theoretical background of multiple scattering in random media is introduced, while the growth and optical characterisation of the nanowire samples used is detailed in chapter 2.

In the presence of strong scattering, it is expected that the traditional diffusive picture of light transport breaks down due to mesoscopic interference effects. In chapter 3, it is demonstrated that the transmitted light through strongly scattering nanowire mats exhibits relative fluctuations in intensity greater than predicted by diffusion. By examining the full statistical distribution of intensities, it is found that the transport is governed by a minimum of only 4 transmission channels on average [2]. This is a record low for a 3D photonic medium and close to the Anderson Localisation transition. In agreement with this interpretation, long range correlations are found in the transmission in Chapter 4.

The non-linearity of the nanowires offers an opportunity to achieve an additional degree of control over the transmission using optical pumping in combination with wavefront shaping techniques. In chapter 5 a digital micro-mirror display (DMD) based spatial light modulator (SLM) is used to focus through the nanowire mat by binary amplitude modulation of the incident wavefront. The non-linearity of the nanowires is then exploited using pulsed laser excitation to achieve control over the optimised spot in chapter 6. It is found that the intensity of the optimised spot can be modulated by up to 63% due to a combination of induced absorption and dephasing. It is also found that the effect of the dephasing can be reversed to give an enhancement in the peak to background intensity of 18%. A summary of the work undertaken in this thesis is then given in Chapter 7.

1.3 Theoretical Background

In this section, the aim is to provide an introduction to the theory of multiple scattering, and how so called 'mesoscopic' interference effects can modify classical diffusion in the presence of strong scattering. Here the term mesoscopic is a consequence of the origin of the theory in solid state electronics. For an electron, such interference is a truly quantum effect as it arises due to its wave-like properties. However, for classical waves there are no quantum implications unless single photons are considered, and the term refers to the interference of propagating light paths that is negligible in the diffusive limit. The treatment of the theory is brief with an emphasis on highlighting the parts relevant to this thesis. For readers desiring a more thorough analysis, the author recommends the book of Akkermans and Montambaux [41] as an excellent reference.

1.3.1 Multiple scattering

When considering the propagation of waves through a disordered collection of scatterers, the concept of a scattering mean free path, l_s, is important. This is defined as the average distance a wave travels before being scattered, which is related intuitively to the average scattering cross-section of the scatterers σ_s and the scatterer density ρ:

$$l_s = \frac{1}{\rho \sigma_s}. \tag{1.1}$$

Throughout this thesis, it will be assumed that scattering is purely elastic (ie no momentum is transferred from the light to the medium) and absorption is negligible. The probability of a wave being traveling for a distance L through such a medium without being scattered decays exponentially as per the Lambert-Beer law (Equation 1.1). As a result, for a medium more than a few mean free paths thick the coherent transmission T_c is vanishingly small:

$$T_c = e^{-L/l_s}. \tag{1.2}$$

In the weak scattering limit ($L > l_s > \lambda$), light takes paths that can be approximated as a set of random walks. As shown in Figure 1.1 (a), the path taken depends upon the exact position and angle of incidence of the incoming wave. Typically many such paths are available to an incident wavefront such as a plane wave. Due to the variation in propagation lengths, the relative phase between each path is randomised. As the result, the outgoing wavefront either in transmission or reflection is a complex interference pattern known as speckle (Figure 1.1 (b)).

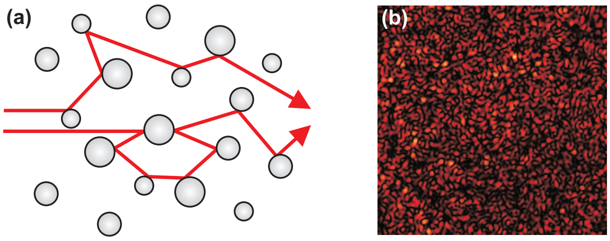

Figure 1.1: (a) Examples of light following random walks within a medium. (b) Image of a transmitted speckle pattern

The mean free path l_s defines the length scale of the random walk. However, it is important to note that this is only strictly true in the case of isotropic scattering. Otherwise, the transport mean free path $l*$ should be used:

$$l* = \frac{l_s}{1 - < Cos[\theta] >}, \tag{1.3}$$

which includes the average of the cosine of the scattering angle θ. This accounts for the effect of the existence of a preferred scattering direction upon the transport, and can be considerably greater or smaller than l_s in the cases of strongly preferential forward or backward scattering respectively [42]. In this thesis, scattering will largely be assumed to be isotropic meaning l_s and $l*$ can be considered to be equivalent and the mean free path will be referred to simply as l.

A speckle pattern can be considered as a unique fingerprint of a specific sample realisation, as small changes in the position of scatterers can dramatically change the resulting interference pattern. Even if the exact form of the scattering potential of a diffusive medium is known (unlikely for real samples), precisely calculating the speckle is a daunting task. However, the average properties can be calculated formally using Green's functions. Otherwise known as intensity propagators, Green's functions describe the evolution of a wave between two points ($\mathbf{r}$ and $\mathbf{r}'$) as the product of the complex amplitudes $\mathbf{a_j}$ and $\mathbf{a_i}*$, where the subscripts indicate the path taken. The complex conjugate $\mathbf{a_i}*$ represents the amplitude of the time reversed path i. These amplitudes can be represented diagrammatically as in Figure 1.2.

Even without knowing the exact form of the intensity propagator, which depends upon the details of the scattering medium, it is still possible to gain some insight into the problem of multiple scattering through this approach. To asses the overall probability of diffusion between two points, the contribution of all possible paths must be considered. By taking the average after summing over all paths, the average probability $P(\mathbf{r}, \mathbf{r}')$ can be defined:

$$P(\mathbf{r}, \mathbf{r'}) \propto \overline{\sum_{i,j} a_i^*(\mathbf{r}, \mathbf{r'}) a_j(\mathbf{r}, \mathbf{r'})}. \tag{1.4}$$

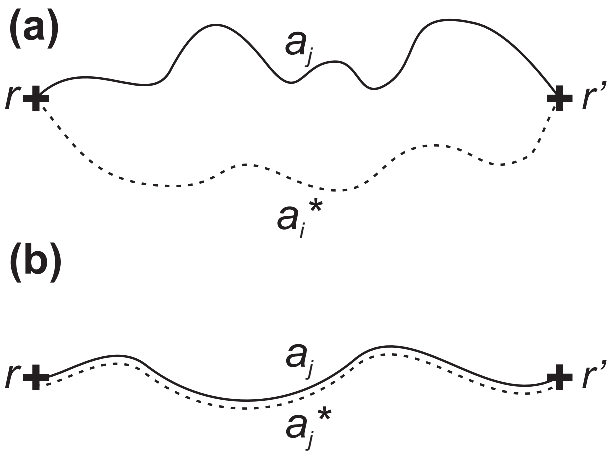

Figure 1.2: (a) Examples of light following random walks within a medium. (b) Image of a transmitted speckle pattern

It is instructive to split this sum into the contributions of when the paths are different ($i \neq j$) and identical ($i = j$), corresponding to the cases shown in Figure 1.2(a) and (b) respectively:

$$P(\mathbf{r},\mathbf{r'}) \propto \overline{\sum_j |a_j(\mathbf{r},\mathbf{r'})|^2} + \overline{\sum_{i\neq j} a_i^*(\mathbf{r},\mathbf{r'})a_j(\mathbf{r},\mathbf{r'})}. \tag{1.5}$$

The first term of Equation 1.5 survives averaging over disorder as the phases are equal and therefore cancel out. In the classical diffusion picture it is assumed that, on average, the contribution from the second term vanishes because of the random dephasing between different paths. This approximation results in the purely classical probability P_{Cl}:

$$P_{Cl}(\mathbf{r},\mathbf{r'}) \propto \overline{\sum_j |a_j(\mathbf{r},\mathbf{r'})|^2}. \tag{1.6}$$

This probability is otherwise known as a 'Diffusion', and under this approximation light transport follows the well known diffusion equation:

$$[\frac{\partial}{\partial t} - D\nabla]P_{Cl}(\mathbf{r},\mathbf{r'},t) = S(\mathbf{r},\mathbf{r'},t). \tag{1.7}$$

Here the source is represented by $S(\mathbf{r},\mathbf{r}',\mathbf{t})$, and the diffusion constant $D = vl/d$ is introduced where v is the group velocity of the propagating light and d is the dimensionality of the medium. For a finite system of volume L^d, the characteristic time for light to diffuse from one boundary to another is given by the Thouless time $\tau_D = L^2/D$. This illustrates one of the key properties of diffusion- it is much slower than ballistic transport (which scales with L instead of L^2). This means that even in thin layers of material such as white paint, light can be trapped for surprisingly long times. As a rough example, a layer of white paint 1 mm thick may have a mean free path of 1 μm, resulting in a typical transport time of the order of 10 ns (depending on the effective refractive index). This is orders of magnitude greater than the 3 ps required for light to transverse this distance in free space.

1.3.2 Transmission channels and conductance

It is helpful at this point to introduce the concept of channels. In this thesis we are interested in a slab geometry of width L and area $A = W^2$, where W is the length of one side. In a transmission experiment, any medium can be described as a transmission matrix t with elements t_{ab} coupling ingoing mode a to outgoing mode b. This situation is shown in Figure 1.3(a). The number of ingoing and outgoing modes is simply defined by the number of degrees of freedom at the respective interfaces. The number of transverse modes, N, in the slab is given by $N \approx Ak_n^2$. Here the refractive index dependent wavevector $k_n = 2\pi n/\lambda$ has been introduced, meaning that there is approximately one mode per square wavelength in the slab.

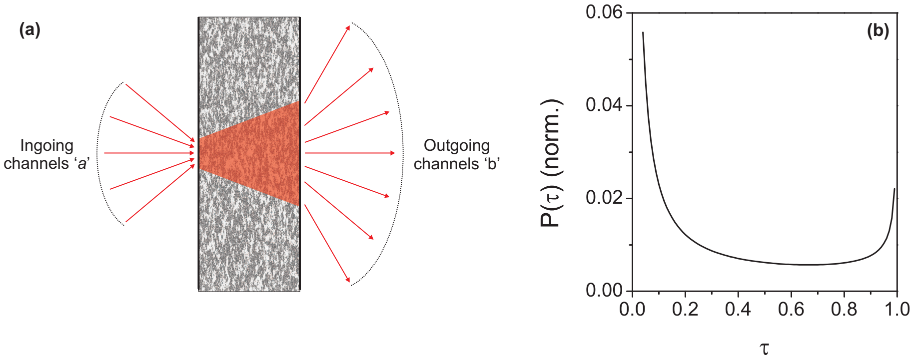

Figure 1.3: (a) Ingoing and outgoing channels to an infinite slab. (b) Bimodal distribution of transmission coefficients

The concept of a transmission channel is an independent way for light to get from ingoing mode a to outgoing mode b. Formally, these are the Eigenchannels of the transmission matrix. A key result from random matrix theory is that the distribution of transmission channels τ follows a bimodal distribution [43], given by $P(\tau) \propto 1/(\tau\sqrt{1-\tau})$ [44] as in Figure 1.3(b). A large number of channels are 'closed' with negligible transmission, meaning the transport is dominated by 'open' channels with close to unity transmission. Consequently, the number of open channels g' is approximately equivalent to the optical analogue of the dimensionless conductance: $g' \approx g = \sum_{a,b} t_{ab}$ [45]. Throughout this thesis, the number of open transmission channels will be referred to simply as 'g'. However, readers should be aware that this is only an effective conductance, and in particular the definition of the true optical conductance through a three dimensional slab is a difficult problem for the reason that increasing the area of the slab will always increase the number of transmission channels. As a result, much of the theory has been developed for quasi-1D waveguide geometries, in which the analogy between the transport of light and electrons is well defined.

By applying appropriate boundary conditions to the diffusion equation (Equation 1.7) the average transmission from a to b, $< T_{ab} >$, can be obtained:

$$< T_{ab} >= \frac{l}{NL}. \tag{1.8}$$

Following from this, the average total transmission from one incident mode $< T_a >$ can be found by summing over all outgoing degrees of freedom b:

$$< T_a >= \sum_b < T_{ab} >= N\frac{l}{NL} = \frac{l}{L}. \tag{1.9}$$

This dependence of the total transmission on l/L is well known, and is a form of Ohm's law. In effect, a multiple scattering medium acts as an optical resistor, a further demonstration of the strong analogy between wave transport and electronics. Similarly, the average conductance can also be derived by summing over all outgoing degrees of freedom b:

$$< g >= \sum_{a,b} < t_{ab} >= N^2\frac{l}{NL} = N\frac{l}{L}. \tag{1.10}$$

From this it is possible to find the average number of open transmission channels through the slab:

$$< g >\approx N\frac{l}{L} = \frac{Ak_n^2 l}{L}. \tag{1.11}$$

This result is only strictly correct for a waveguide geometry ($W > L$). In a typical optical experiment, light is incident on a small portion of the overall area of a slab, and spreads transversely due to diffusion. This point is addressed further in chapter 3. Typically diffusive media have a large number of open transmission channels due to a low scattering strength, characterised by values of $k_n l >> 1$.

1.3.3 Mesoscopic interference

The diffusive picture of light transport in disordered media presented so far is a theory that is extremely successful in describing the majority of multiple scattering effects. However, it is based upon the assumption that the second term in Equation 1.5 goes to zero when it is averaged over disorder. This term contains the interference between different paths. Contrary to the argument that the phase differences between these different paths are large and random, it is quite easy to see that there exists a possible set of paths which are similar but not identical. An important example is the case of a Diffusion crossing with itself, shown in Figure 1.4, in which the paths share the same scattering events but propagate in opposite directions around a loop.

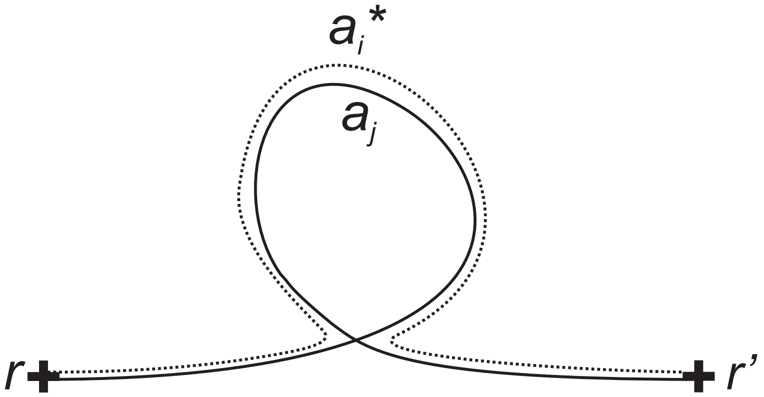

Figure 1.4: Scattering loop in which propagators share scattering events but travel in opposite directions.

Due to time reversal symmetry the two paths in Figure 1.4 will have identical phases, interfere constructively and survive averaging over disorder. As a result the 'mesoscopic' interference term in Equation 1.5 would not go to zero, and light transport could no longer be described purely by the classical diffusion process. As the interference is constructive, there is a reduced probability of diffusion away from the point of interference. This provides a negative correction to the conductivity, and in extreme conditions leads to Anderson localisation as the probability of diffusion goes to zero. A system can be said to be localised for $g < 1$, corresponding to an average of less than 1 open transmission channel. This is the point of transition between a conductor and insulator induced by disorder, as per Anderson's original proposal.

However, due to the success of diffusion in describing multiple scattering, the correction must be small for everyday phenomena. The probability of this happening in a system of volume Ω is strongly connected to the probability of return $Z(t)$ of a diffusion to the same point:

$$Z(t) = \int d\mathbf{r} P_{cl}(\mathbf{r}, \mathbf{r}, t) = \frac{\Omega}{(4\pi D t)^{d/2}}. \tag{1.12}$$

It can be seen from Equation 1.12 that both dimensionality and scattering strength have an impact on the likelihood of return. In three dimensions the probability of a Diffusion returning to the origin is small, whereas in one and two dimensions the probability is high given a large enough system. For this reason, strong disorder is not a requirement for the observation of Anderson localisation in one and two dimensional disordered mediums, which can be considered to always be localising if of sufficient size. However, in order to observe mesoscopic interference effects in three dimensions it is expected that the mean free path must be smaller than optical wavelengths to trap light sufficiently close to the origin. This can be understood intuitively by considering that scattering several times over the space of one wavelength results in the wave description of light losing some meaning. This expectation leads to the Ioffe-Regel criterion for localisation of $kl \approx 1$.

There are other possible sets of paths that survive averaging over disorder, resulting in corrections to classical diffusion. In these 'crossings', two Diffusions share a scattering event and exchange amplitudes. Examples containing 1 and 2 such crossings are shown in Figure 1.5.

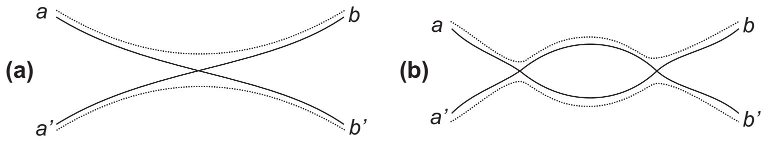

Figure 1.5: Two diffusions interacting through (a) 1 and (b) 2 crossings, exchanging amplitudes.

Again, in order for the dephasing between the two paths to be smaller than 2π, a mean free path shorter than optical wavelengths ($l < \lambda$) is required. The probability of such crossings occurring, $p_\times$, is closely related to the probability of return. By assigning a characteristic volume to a diffusion $\lambda_{d-1} v \delta t$ as it explores a medium of volume L^d, this probability can be expressed as the ratio of volumes:

$$\delta p_\times(t) = \frac{\lambda_{d-1} v \delta t}{L^d} \approx \frac{1}{g} \frac{\delta t}{\tau_D}. \tag{1.13}$$

By integrating over the Thouless time, the probability of a crossing in the time it takes for light to diffuse through the medium can be obtained:

$$p_\times(\tau_D) = \int_0^{\tau_D} \delta p_\times(t) \approx \frac{1}{g}. \tag{1.14}$$

As long as the crossings are independent, it follows that the probability of two crossings is of the order $1/g^2$. In the weak scattering limit ($\lambda < l$), the contribution of mesoscopic interference to light transport can then be considered to be a power series in $1/g$ depending on the number of crossings. As the conductance is typically large the classical diffusion picture is retained, with small corrections due to mesoscopic interference. These crossings serve to correlate transmission channels, resulting in an overall reduction in the number of independent transmission channels.

Both the crossing of a diffusion with itself and the crossing of two Diffusions can be considered to have the same effect of lowering the dimensionless conductance g. The overall probability of transmission with one crossing $p_0(\tau_D)$ is a combination of both effects, given by Equation 1.15:

$$p_0(\tau_D) \approx p_\times(\tau_D) \int_0^{\tau_D} Z(t) \frac{dt}{\tau_D} = \frac{1}{g} \frac{Z(\tau_D)}{\tau_D}. \tag{1.15}$$

Experimentally measurable consequences of such crossings include increased correlations [46, 47] and relative fluctuations in transmission [48–50], discussed further in chapters 3 and 4. Such measurements have been made for light in three dimensions, generally using samples consisting of Titanium Dioxide powder. These studies found typical values of g' in the range of 100-1000 [51–53], and as a result the effect of mesoscopic interference was measurable but subtle. This approach was also adopted in the demonstrations of localisation of ultrasound and microwaves, demonstrating that such effects survive the localisation transition. Assessment of transmission fluctuations and correlations to find g' is a useful tool to characterise mesoscopic effects, and is the approach adopted in this thesis.

1.3.4 Anderson Localisation

As may be expected for a phase change between a conductor and an insulator, Anderson localisation results in behaviour markedly different from that of diffusion. One key difference is the dependence of the transmission on sample thickness. While for diffusion the total transmission decays linearly with L as in Equation 1.5, when localised it decays exponentially.

$$T_a = e^{-\frac{L}{\xi}} \tag{1.16}$$

Here the localisation length ξ has been introduced, which is the characteristic distance required for a wave to become localised within the medium. For $L > \xi$ the average number of open channels is less than 1 and the medium becomes a perfectly reflecting insulator in the absence of absorption. As this is a clear, measurable effect, the first report of Anderson localisation of light was based on the observation of an exponential drop in transmission through layers of Gallium Arsenide powder [36]. However, it has been suggested that absorption could have been responsible for this effect [39].

This reflects the problem of conclusively demonstrating Anderson localisation of light in three dimensions. It is difficult to make samples with sufficient scattering strength, and other phenomena have effects that can mimic localisation. Other studies have shown anomalously long dwell times of light in a thick layer of Titanium Dioxide [37], recently backed up by the observation of a halt in the diffusive spread of light at long times [38].

While seemingly strong evidence of localisation, it has been suggested that florescence could have similar effects [54].

As a result, the current state of the field is that there is no undisputed demonstration of Anderson localisation of light in three dimensions, despite several pioneering studies. There is even some debate over whether it is even possible due to the vector nature of light as much of the theory considers the case of scalar waves [40]. Other studies have demonstrated localisation of both acoustic [30] and matter waves [32] in 3D, as well as localisation of microwaves and light in lower dimensional systems [31, 34, 33].

The fundamental nature of mesoscopic transport and the ongoing theoretical development is what makes the field exciting. However, in the experience of the author it also leads to some confusion due to the interplay between precisely defined theory and experiments which are by their very nature less controlled but at times equally complex. To a newcomer to the field it is not immediately obvious that Anderson localisation of light in three dimensions is still an open question, and as in this section a certain amount of caution is often employed in its discussion. By no means does the work presented in chapters 3 and 4 of this thesis settle the issue. However, the strong mesoscopic effects found show that it is at least possible to get close to the localisation transition in a 3D photonic medium.

Chapter 2

Nanowires

2.1 Nanowire materials

Semiconductor nanowires are a material of great technological promise, with a host of potential applications including the important area of light harvesting and photovoltaics [1, 55–60]. State of the art methods can grow high crystal quality nanowires over a large area with a high degree of homogeneity. Some of the benefits of using III-V semiconductor nanowires include compatibility with current silicon based semiconductor technologies, precise control over the composition and crystal structure, high surface area to volume ratios and access to the interesting physics of nanoscale structures.

Of particular interest here is the effect of a nanowire diameter comparable to optical wavelengths on its light scattering properties. It has been shown previously that disordered, densely packed mats of Gallium Phosphide (GaP) nanowire are amongst the strongest scattering materials available [61]. Optical mean free paths as low as 0.2 μm can be achieved due to a combination of a high refractive index (around 3.5 in the visible), tuning the diameter to achieve resonant scattering and high volume packing fraction. This is of obvious interest for studies of mesoscopic effects in three dimensions which depend on light being scattered on a length scale smaller than the wavelength, and such nanowire mats form the basis for the work in this thesis. The intrinsic nonlinearity due to the semiconductor material used is also of interest, as it offers the possibility of optically controlling the scattering properties of the nanowires.

2.2 Growth of nanowire mats

2.2.1 MOPVE

The nanowires in this project were grown using metal-organic vapour phase epitaxy (MOPVE) by Tilman Zehender in the group of Erik Bakkers at the University of Eindhoven during two visits by the Author. Here a brief overview of the process described in Ref. [1] is presented. Firstly the GaP wafer to be used as a substrate was prepared for insertion into the MOPVE reactor. A 200-300 nm SiO2 layer was deposited on the back side of the wafer in order to protect it during the rest of the process. The substrate was then etched using Aqua Regia for 2 minutes in order to remove the surface oxide layer from the front of the wafer. Immediately after this step, a thin layer of gold was evaporated onto the exposed GaP surface.

The substrate was then placed into the MOPVE reactor chamber, which is heated to cause the gold film to melt and form randomly distributed droplets over the surface in the first stage of the process. The precursor gasses TriMethylGallium (TMGa) and Phosphine (PH3) were then passed over its surface while the substrate was rotated. The gold droplets absorb Gallium and Phosphor from the precursor gasses. Once a droplet becomes saturated, a single layer of GaP is deposited on the substrate, and in this way a nanowire is grown upwards with the gold remaining on its tip. This growth process is illustrated by Figure 2.1.The direction of the nanowire growth is controlled by selection of the crystal orientation of the substrate. A [100] orientation was used in order to achieve nanowires in a 'crossed' configuration, growing at an angle to the surface normal in order to create a 3D disordered medium. This occurs because the preferred growth direction is [111] direction, roughly at 35 degrees to the [100] orientation.

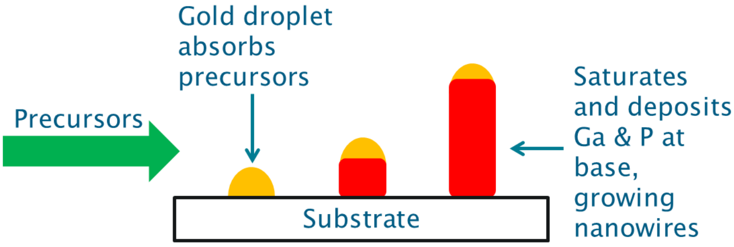

Figure 2.1: Cartoon representing nanowire growth scheme.

It is possible to switch between this axial growth to a radial growth by increasing the temperature in the reaction chamber, altering the chemistry of the interaction of the gasses with the gold. By iterating between axial and radial growth schemes, arrays of long, thick wires with precisely controlled diameters can be grown over a large area. In growing nanowire samples for this project, the intention was to use different numbers of cycles between axial and growth to produce nanowire layers of different thickness but otherwise similar properties. This is of interest for the study of mesoscopic effects, specifically whether the Anderson localisation transition in three dimensions can be reached by increasing the thickness of a strongly scattering material. The samples used fall into two groups: those grown using a 1 nm thick gold film, and those using a 2 nm thick layer. The use of a 2 nm gold film was due to an issue with the gold evaporator on the Authors second visit. Despite this being unintentional, these samples displayed some interesting behaviour, as seen below.

The samples grown using a 1 nm gold film form the basis for most of the investigations in this thesis. Three different nanowire layer thicknesses were grown: 1.5, 4.5 and 6 μm corresponding to 1, 2 and 5 growth cycles respectively. The 1 and 2 cycle samples were grown before the start of the project, and correspond to the samples numbered 10 and 11 in Ref. [61]. Scanning electron microscope (SEM) images of the 5 cycle sample are shown in Figure 2.2.

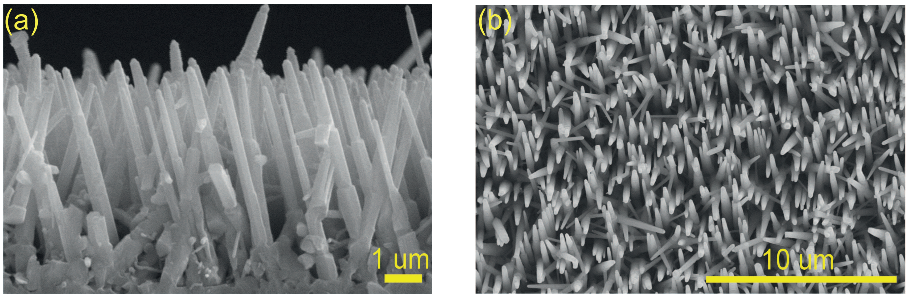

Figure 2.2: (a) side and (b) top view scanning electron microscope images of the 6 μm thick 5 cycle nanowire sample.

It can be seen from Figure 2.2 that the growth process produces a very densely packed disordered nanowire mat, 6 μm thick with a nanowire diameter of approximately 200 nm. This diameter is slightly larger than that of the 1 and 2 cycle samples (around 120 nm), as a consequence of a larger number of radial growth cycles. This is also likely to be the cause of the porous layer that can be seen at the base of the wires. The top view image shows that a uniform layer is produced over a large area, which is important for optical experiments.

Samples were also grown using the same growth parameters but with a 2 nm gold film, with 1.5, 10 and 15 growth cycles used. The intention was to create very thick layers of nanowires to investigate the possibility of Anderson localization of light in such samples. Figure 2.3 shows SEM images of these nanowires. Dramatically different results are seen for the 10 and 15 cycle samples, which appear extremely chaotic with a range of wire diameters from 500-1000 nm. Some exceptionally long nanowires can be seen protruding from the more densely packed body of these samples. It is the denser region that is expected to give the thickness of these layers once pressed against glass, as the longer nanowires will break off. The depth of these layers was estimated to be 25 and 30 μm respectively. However, the difference in diameter to the 1 nm film samples means that the scattering behaviour of the two sets of samples is not expected to be directly comparable.

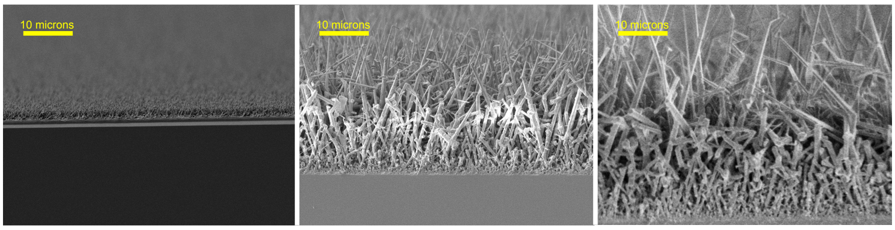

Figure 2.3: Side view SEM images of nanowires grown using a 2nm gold film with (a) 1 (b) 10 and (c) 15 growth cycles.

The large difference in nanowire properties seen using the same growth recipe with gold films differing by only 1 nm highlights the sensitivity of the growth process. An overview of the dependence of the thickness of the nanowire layer with number of growth cycles is given in Figure 2.4.

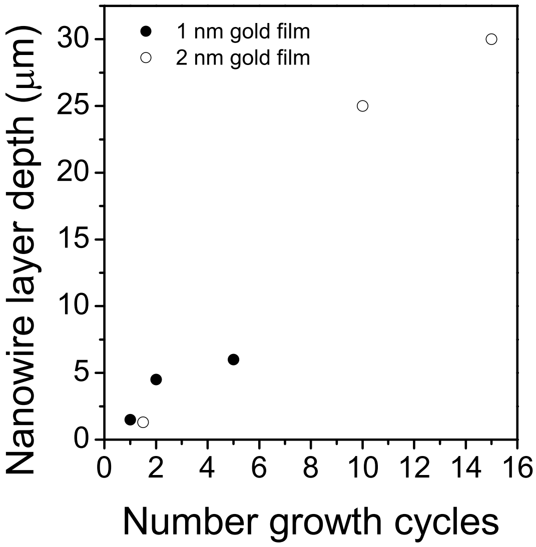

Figure 2.4: Dependence of sample thickness on number of growth cycles for both the 1 and 2 nm gold seed layer.

While the number of data points is too small to make concrete conclusions about any trends, it appears that the layer growth using a 1 nm gold film slows dramatically after 2 cycles. This, along with the porous layer of GaP seen on the 5 cycle sample,s is an indicator the limit of this specific growth recipe has been reached. The 2 nm gold film appears to support much longer layers. While the 1.5 cycle sample is relatively ordered, the nanowire growth for the 10 and 15 cycle nanowires appears essentially random indicating that control over the growth process has been lost. From the samples grown for this project, it appears that in order to produce thicker nanowire layers with high scattering strength in a controlled fashion a new growth recipe may be needed.

The nanowire samples used in this thesis are summarised in Table 2.1. In order to facilitate further discussions, the samples are assigned a reference number.

Label	**Gold thickness**	**Growth cycles**	**Nanowire diameter**	**Layer thickness**
1	1 nm	1	120 nm	1.5 μm
2	1 nm	2	120 nm	4.5 μm
3	1 nm	5	200 nm	6.0 μm
4	2 nm	1.5	250 nm	1.3 μm
5	2 nm	25	500-1000 nm	25 μm
6	2 nm	30	500-1000 nm	30 μm

Table 2.1: Summary of nanowire samples.

2.2.2 Pressing against cover slip

Before use in optical experiments, the 2 inch wafer the nanowires were grown on was cleaved into sections of approximately 1 cm^2, and the nanowires were then pressed against a 170 μm thick glass cover slip. This serves the function of slightly compacting the nanowire layer, increasing its homogeneity and also protecting the nanowire sample. The pressing was done by hand until a colour change was observed indicating good contact between the nanowires and the glass, after which the sample was glued in place.

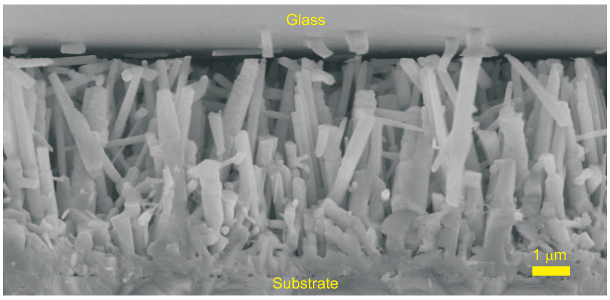

Figure 2.5: Nanowire sample after pressing against a glass cover slip.

An image of sample 3 after pressing is shown in Figure 2.5. This image may not be representative of the entire sample as the nanowires along the edge may also have been broken by the cleaving process.

2.3 Optical characterisation

The scattering properties of samples 1 and 2 were previously extensively characterised in Ref. [61], finding a minimum optical mean free path of 0.2 μm. Figure 2.6 shows the dependence of the mean free path, diffusion constant and group velocity on wavelength of sample 2 measured by Dr O.L. Muskens using the broadband spectroscopy methods detailed in [61].

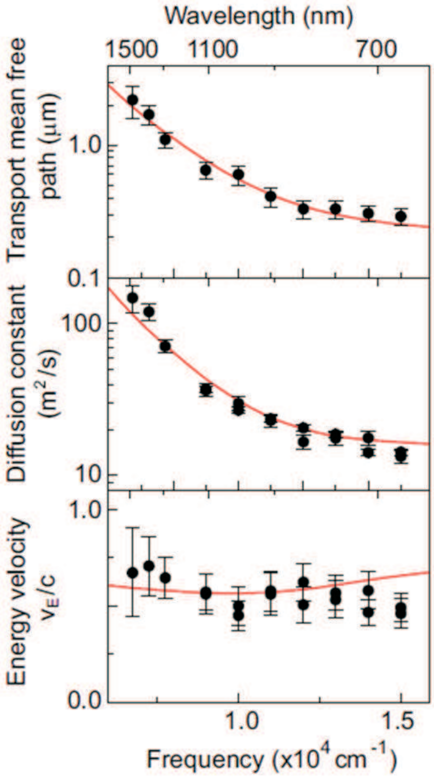

Figure 2.6: Optical properties of sample 2 measured by Dr. O.L. Muskens.

While the nanowires grown for this thesis were grown using nominally the same recipe, the results differed by varying amounts to samples 1 and 2 grown previously using the same recipe. Sample 3, grown with 5 growth cycles using a 1 nm thick gold film, is similar and expected to have similar scattering properties. In contrast samples 5 and 6, grown with 10 and 15 growth cycles using a 2 nm gold film, are clearly very different. Further optical characterisation is required in order to see how the behaviour of the nanowire samples compare.

2.3.1 Total transmission

A good starting place for the optical characterisation of the nanowire mats is by investigating their total transmission as a function of wavelength. By comparing the total transmission of layers with different thicknesses, it is possible to check that the scattering mean free paths are roughly consistent between samples. The setup used to measure the total transmission is shown in Figure 2.7. A variable wavelength coherent light source was obtained using a Fianium supercontinuum laser in conjunction with a prism based monochrometer. An integrating sphere collected a large proportion of the transmitted light, which was then detected by either a Silicon (Si) or Indium Gallium

Arsenide (InGAs) photodiode mounted on the sphere. An optical chopper and lock-in detector were used to increase the signal to noise ratio. By scanning the slit in the monochrometer (mounted on a computer controlled stage) the spectral dependence of the total transmission was obtained, normalised to a reference scan with the sample removed.

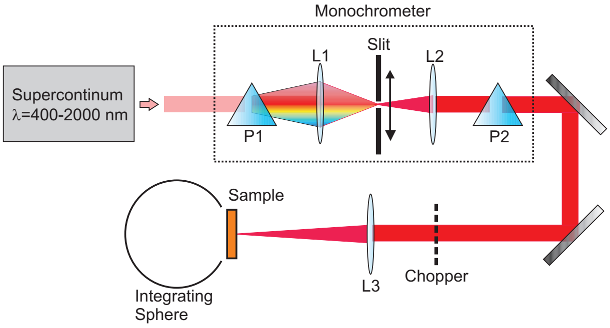

Figure 2.7: Experimental setup for measuring the spectral dependence of the total transmission through the nanowire samples.

The total transmission of the nanowires grown using a 1 nm gold film (Figure 2.8 (a)) shows broadly similar features for all the samples. The effect of absorption due to the bandgap around 550 nm can be seen clearly, and the transmission increases towards the infrared as the Rayleigh scattering regime is approached. The transmission drops as the layer thickness increases. As discussed in Chapter 1, this is consistent with the prediction of Ohms law, and suggests the scattering properties of the samples are similar. However, it should be noted that absorption will also result in a drop in transmission with an exponential dependence so this cannot be taken as conclusive evidence that the mean free path of sample 3 is similar to that of samples 1 and 2. In order to investigate this further, coherent backscattering experiments are carried out later on in this chapter.

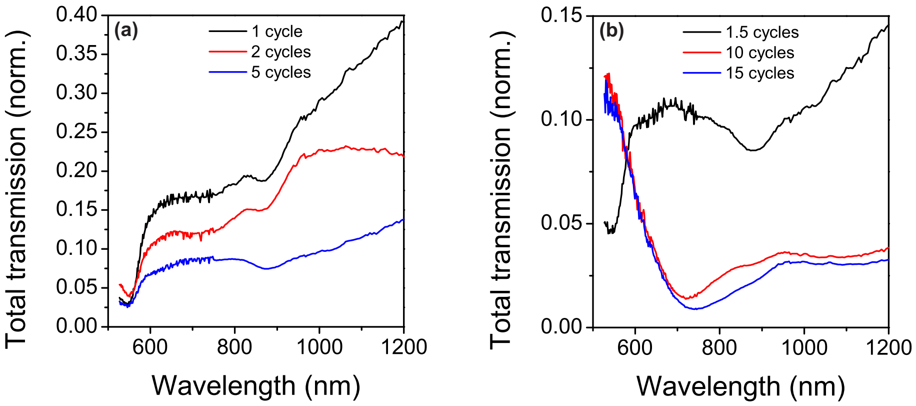

Figure 2.8: Total transmission measured through nanowire samples grown using (a) 1nm and (b) 2 nm gold films.

In contrast to the nanowires grown using a 1 nm gold film, samples 5 and 6 show a remarkable drop in transmission around 730 nm. Additionally, the transmission of these samples around the bandgap is significantly higher that of the much thinner sample 4 also grown using a 2 nm film. Both behaviours are unexpected and repeatable over several sample positions. The large dip in transmission around is interest as these samples were grown with the intention of seeing if the Anderson localisation regime could be reached by increasing the thickness of the nanowire samples. However, as discussed in Chapter 1, a drop in transmission is not sufficient evidence of Anderson localisation due to the similar signature of absorption. Indeed, in such thick nanowire mats for which the growth process appears to have been relatively uncontrolled, the presence of absorption is a real possibility.

2.3.2 Coherent backscattering

Another characterisation technique of interest is that of analysing the coherent backscattering (CBS) cone in order to obtain information about the scattering mean free path l of the medium. CBS is a universal and robust phenomenon seen in multiple scattering of coherent light in which reflected light paths interfere constructively in the exact backscattering direction to give a cone higher than the expected diffusive intensity. It is often referred to as a weak localisation effect due to its dependence on the interference of time reversed paths [62, 63].

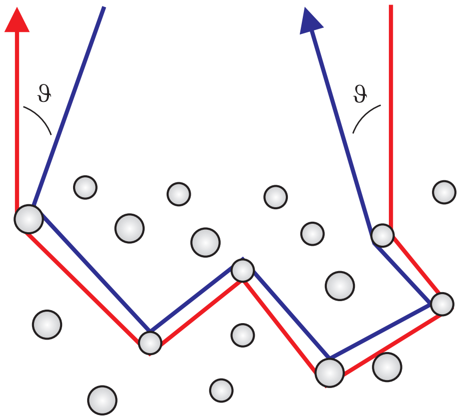

Figure 2.9: Diagram showing the geometry of the coherent backscattering effect. The counter propagating paths indicated by the red and blue arrows constructively interfere resulting in a cone of enhanced reflected intensity in the backscattering direction.

As illustrated by Figure 2.9, due to time reversal symmetry each light path in reflection has an equal chance of propagating in the opposite direction, accumulating the same phase and interfering constructively to give twice the expected intensity in the exact backscattering direction. As the angle ϑ between the counter propagating paths increases from zero, the dephasing between the two paths grows and the interference effect reduces towards the expected value of the diffuse reflection, creating a cone. The width of the cone itself is proportional to $1/kl$ [64], meaning strongly scattering materials exhibit a wider cone due to the reduced dephasing between light paths. This makes CBS a useful tool for characterising multiple scattering media [1], indeed the mean free paths of samples 1 and 2 in Ref. [61] were measured using this technique.

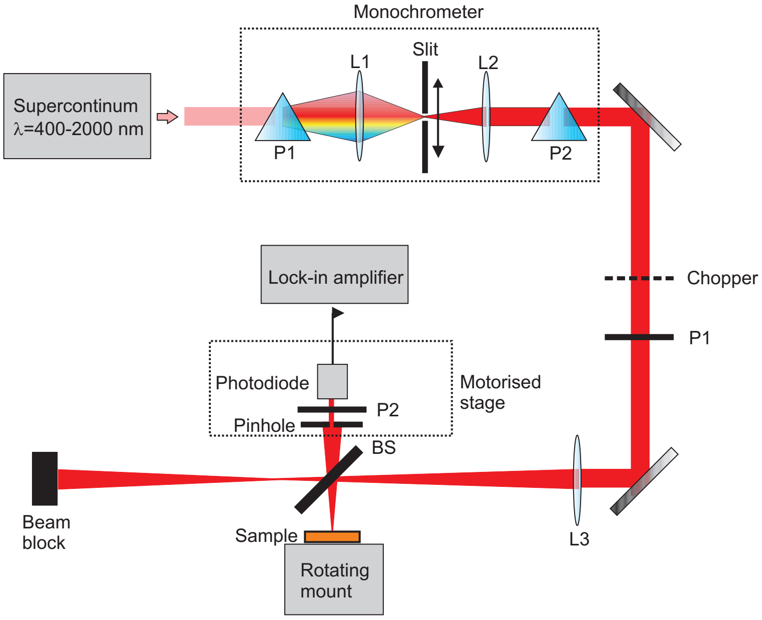

Figure 2.10: Experimental setup of CBS experiment.

The experimental setup used to measure CBS in the nanowire samples is shown in Figure 2.10. As for the total transmission experiment, light is taken from the output of a Fianium Supercontinum laser filtered by a prism based monochrometer. Light polarised by polariser P1 is directed onto the sample by a beam splitter BS (5 cm long), and the reflection is analysed by a 200 μm pinhole and second polariser P2 before being collected by a photodiode. The backscattering angle is scanned by displacing the computer controlled motorised stage the components are attached to. In order to obtain a large angular range, the distance between sample and pinhole is kept as small as possible, which in this case is 5 cm. A lock-in amplifier and optical chopper are used to improve the signal to noise ratio. The sample is mounted on a downwards tilted rotating mount. The tilt served to direct the coherent reflection from the sample surface away from the pinhole, while the rotation averages out the speckle to allow the enhancement over the diffusive background to be measured. The exact backscattering direction is found using a mirror aligned to be normal to the incoming beam in place of the sample and moving the pinhole to obtain the highest intensity.

In this experimental setup, the CBS cone exists in the polarisation parallel to that of the incident polarisation. In order to divide out the diffuse background, sequential scans are taken with the detected polarisation parallel and crossed with the incident polarisation. The data for the parallel polarisation is then normalised to that taken with the crossed polarisation in order to obtain the enhancement to the backscattering caused by the constructive interference. As the beam splitter transmits S and P polarisation differently, the choice of detection polarisation angle is important. P polarisation corresponds to a vertical polarisation with respect to the optical bench, whereas a horizontal polarisation is a combination of S and P polarisation. The desired situation is that there is no difference in transmission through the beam splitter for the detection of the parallel and crossed polarisations. This is achieved by arranging the polarisers so that the parallel and crossed cases correspond to angles of ±45 degrees to the vertical for the detecting polariser P2.

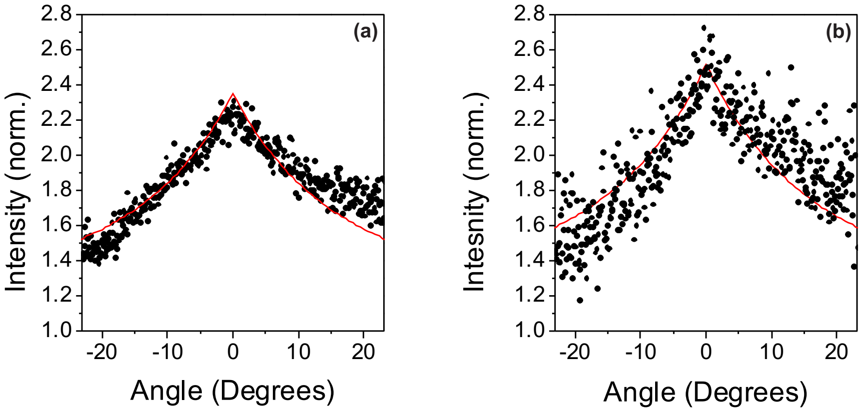

Figure 2.11: Experimental CBS cones for (a) sample 2 and (b) sample 3. Lines are fits from the theory of Ref. [1] with a mean free path of 0.13 μm

The experimental results for samples 2 and 3 using light at 633 nm are shown in Figure 2.11. A clear enhancement in the backscattering direction is observed, and due to the high scattering strength of the samples the CBS cone is extremely broad. The peak enhancement in this case is above 2, which is due to experimental factors as the theoretical maximum enhancement is 2. This could likely be avoided if it were possible to normalise to the wings of the cone as is common in other studies, however, in this case the range of the measurement is not wide enough to do this. The reflected angular intensity normalised to the diffuse background, $I(\vartheta)$, is fitted by the theory from Ref. [1]:

$$I(\vartheta) = [\gamma_l + (E-1)\gamma_c]/\gamma_l. \tag{2.1}$$

Here γ_l gives the contribution of the ladder diagrams resulting in the diffusive reflection and γ_c the contribution of the crossed diagrams leading to the constructive interference in the backscattering direction. These are defined as follows:

$$\gamma_l = 3cos[\vartheta]\left(\frac{z_e}{l} + \frac{cos[\vartheta]}{1+cos[\vartheta]}\right) \tag{2.2}$$

$$\gamma_c = \frac{3}{1/cos[\vartheta]+1}\frac{1}{(k_0 l sin[\vartheta] + 1/2(1/cos[\vartheta]+1))^2 + cos^2[\vartheta]}\left(1 + \frac{(1/cos[\vartheta]+1)z_e}{l + z_e k_0 l sin[\vartheta]}\right). \tag{2.3}$$

Here the extrapolation length z_e has been introduced, accounting for the effect of internal reflections and taken to have a value of $2l/3$ [65] in this instance. The factor E in (2.1) is a correction for the experimental enhancement of the cone. Ideally this should take a value of 2, however, as discussed earlier in this section in reality the measured enhancement is different from this. For the fitting of the experimental CBS cones E is set to the be equal to the peak intensity of the cone in order to get good agreement.

Both samples are reasonably described by fits with l=0.13 μm. This is slightly lower than the previous findings for sample 2. It can be seen that the shape of the CBS cone are asymmetric, with the wing at positive angles showing a shallower slope. This is again an experimental artifact, possibly due to spurious reflections from the edge of the beam splitter since a cut off in the observed cone due to this edge was observed at a positive angle of 26 degrees. In effect, the fit has averaged between the two wings, explaining the slightly lower than expected value of l obtained. However, the fact that the same value describes both samples reasonably indicates that sample 3 has similar scattering properties to samples 1 and 2 grown previously using the same recipe.

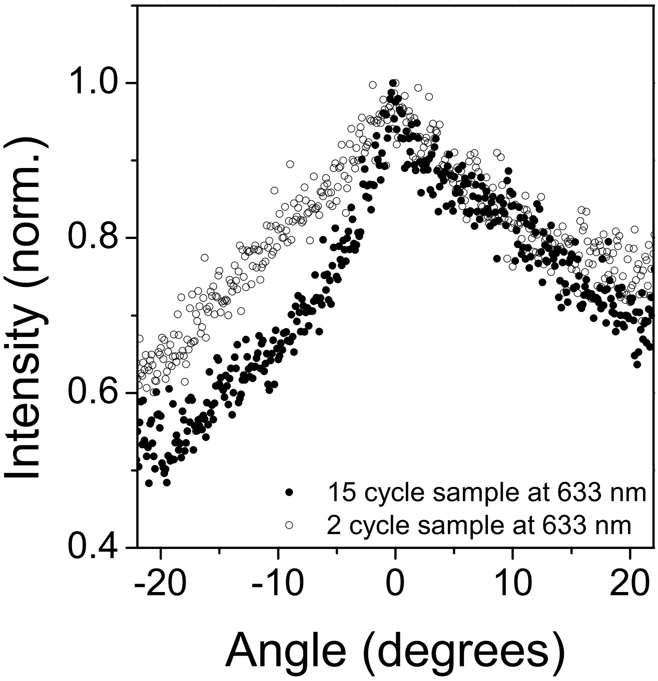

Figure 2.12: Measured CBS cone at 633 nm for the sample 6 (solid points) compared to that of sample 2 (open points). Values have been normalised to the peak intensity.

Figure 2.12 shows a comparison between the CBS cone of the 15 cycle nanowire sample grown using a 2 nm gold film and the 2 cycle nanowire sample at a wavelength of 633 nm. In order to compare the cones they have been normalised to the peak value. It can be seen the shallow slope at positive angles is similar for both samples. As discussed above, this is likely to be an experimental artifact and should be disregarded. At negative angles the 15 cycle cone is noticeably narrower than the 2 cycle sample, indicating reduced scattering strength. This is perhaps not surprising as the growth of this sample was much less controlled than that of the 2 cycle sample grown specifically to have a high scattering strength. It does not explain the large dip in transmission at 730 nm, however, the behaviour at 633 nm is not necessarily representative of that at higher wavelengths. In order to investigate whether there is a scattering resonance around 730 nm contributing to the dip in transmission, CBS cones were measured over a series of wavelengths.

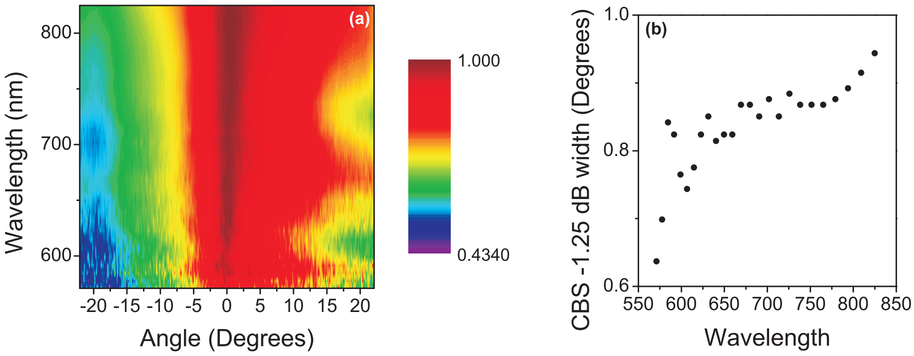

Figure 2.13: (a) Spectral dependence of CBS cone measured for sample 6. (b) Half width of the CBS cone from peak to 75% (-1.25 dB) of the peak value as function of wavelength.

In Figure 2.13 (a) it can be seen that the width of the CBS cone increases with wavelength, indicating that the scattering strength $1/kl$ increases with wavelength. However, there is no clear sharp increase in width around the wavelength region for which the dip in transmission was previously observed for this sample around wavelengths of 740 nm. In order to examine this more closely, a measure for the width of the cone is required. Considering only negative angles due to the anomalous slope at positive angles, the angle between the peak and the point at which it drops by 75% was measured as a function of wavelength and plotted in Figure 2.13 (b). No large increase in width is seen around 740 nm over the general increasing trend, in fact in this region the width of the cone appears to be relatively constant. Therefore this particular investigation shows no evidence of a scattering resonance that may lead to Anderson localisation, although there is clearly room for further refinements of the experimental setup to eliminate the artifacts observed.

2.4 Conclusion

Disordered semiconductor nanowire mats were grown in order to create strongly scattering samples, and their optical transport properties investigated through examining the total transmission and coherent backscattering of the nanowires. Sample 3, grown with

5 cycles of axial and radial growth using a 1nm gold film, was found to be thicker but have similar characteristics to samples grown previously using less growth cycles. This is of great interest for investigating mesoscopic effects, as it is expected that increasing the thickness of a sufficiently strongly scattering sample may approach the Anderson localisation condition. Nanowires were also grown using a 2 nm gold film, resulting in very thick chaotic layers with a range of nanowire diameters. While this was not the desired result samples 5 and 6, grown using 10 and 15 growth cycles respectively, show an interesting dip in the total transmission at 740 nm. However, from the coherent backscattering experiment these samples appear to be less strongly scattering at 633 nm than the samples grown with a 1 nm film, and no evidence of a scattering resonance at 740 nm. This appears to suggest the dip in transmission is not a localisation effect and may instead be attributable to absorption, although further investigation is required.

Chapter 3

Mesoscopic fluctuations

Under sufficiently strong scattering conditions, the classical diffusion description of light transport is expected to break down due to mesoscopic interference resulting from crossing light paths [41]. As the nanowire mats detailed in chapter 2 are amongst the strongest optically scattering materials available, they are promising candidates for probing the regime close to Anderson localisation. In order to do this, inspiration was taken from the studies investigating localisation of microwaves [31] by investigating the relative fluctuations in transmitted intensity. This approach has the advantage of being robust against the effects of absorption [66], as it only serves to reduce the overall transmission without increasing intensity fluctuations. Indeed, absorption acts to selectively attenuate longer light paths, reducing the probability of mesoscopic interference. As well as the nanowire mats, layers of Zinc Oxide (ZnO) were investigated using the same method. Such samples of 'white paint' are typically used in scattering experiments and have a significantly higher mean free path than the nanowire samples used.

3.1 Transmission statistics theory

Before discussing the experiment, it is helpful to discuss the theory used to assess the results. In this section a summary of the relevant theory is presented, however, it is by no means exhaustive and readers interested in further details should consult the corresponding papers.

3.1.1 Diffusive limit

As a speckle pattern is created by the interference of different light paths through a disordered medium, its appearance is that of a random distribution of intensities with a rough grainy structure due to short range correlations. The average transmission from ingoing channel a to outgoing channel b, T_{ab}, can be calculated as in chapter 1. In the diffusive limit ($g' \to \infty$), the central limit theorem applies as the transmitted intensity is obtained by summing over many different uncorrelated paths. In this case, the probability distribution of intensities in a speckle pattern is described by a negative exponential with a slope of unity. This is the well known 'Rayleigh law' (Equation 3.1):

$$P(T_{ab}) = \frac{1}{< T_{ab} >} \mathrm{Exp}[\frac{-T_{ab}}{< T_{ab} >}]. \tag{3.1}$$

The N^{th} moment $< T_{ab} >^N$ of this distribution can also be calculated in order to characterise its features [49]:

$$< T_{ab}^N >= n! < T_{ab} >^N . \tag{3.2}$$

A simple measurement of the fluctuations in T_{ab} is obtained by considering the second moment of the distribution, which defines the characteristic width of the distribution. Rather than using the raw moment given in Equation 3.2, it is more usual to use the central second moment, the variance $Var[T_{ab}]$:

$$Var[T_{ab}] =< T_{ab}^2 > - < T_{ab} >^2 . \tag{3.3}$$

By substituting Equation 3.2 into Equation 3.3, it can be seen that the fluctuations in T_{ab} are of the order of the average value $< T_{ab} >$. In order to decouple the statistics from the average transmission, which is vulnerable to effects such as absorption, T_{ab} is normalised to its average value, obtaining the normalised transmission $S_{ab} = T_{ab}/ < T_{ab} >$. The expectation in the diffusive limit is then that the relative fluctuations in speckle intensity are unity, i.e. $Var[S_{ab}] = 1$. In this regime, the variance of the normalised total transmission, $S_a = t_a/ < t_a >$ goes to zero.

3.1.2 Speckle contrast

The discussion above assumes that the transmitted speckle is fully developed, i.e. the illuminating light has a bandwidth much lower than the spectral width of the transmission modes and that the imaging is perfect. In the diffusive regime the $Var[S_{ab}]$ can be used to characterise the contrast, with a value of 1 indicating completely developed speckle. In real experiments a contrast of 1 is difficult to obtain. While using a narrow line width laser normally avoids problems with bandwidth, invariably some light is lost in the imaging system.

The effect of a reduced contrast is to 'wash out' the fluctuations in the speckle. In the extreme case of a contrast of 0, speckle is replaced by a diffuse distribution of light.

This corresponds to the disappearance of speckle when a random medium is illuminated by a broadband light source, and is a result of the superposition of many independent speckle patterns. In this thesis, the contrast is typically close to 1, and its effect is often neglected. When it is treated, the contrast is included as a factor affecting the average transmission $< T_{ab} >$. Equation 3.4 shows how Equation 3.1 is modified to include the effect of the experimental contrast, C:

$$P(S_{ab}) = \frac{1}{S_{ab}}\mathrm{Exp}[\frac{-S_{ab}}{C}]. \tag{3.4}$$

This approach relies on the deviation of the contrast from 1 being small, as it does not fully describe the probability distribution for very low values of contrast. However, this approximation is suitable for our experiments for which the contrast is taken into account. In order to see the effect of a reduced contrast, Equation 3.4 is plotted for a range of contrasts in Figure 3.1. The moments of these distributions are also plotted, and compared to the expectation of Equation 3.2 modified to contain a reduced contrast in the same way.

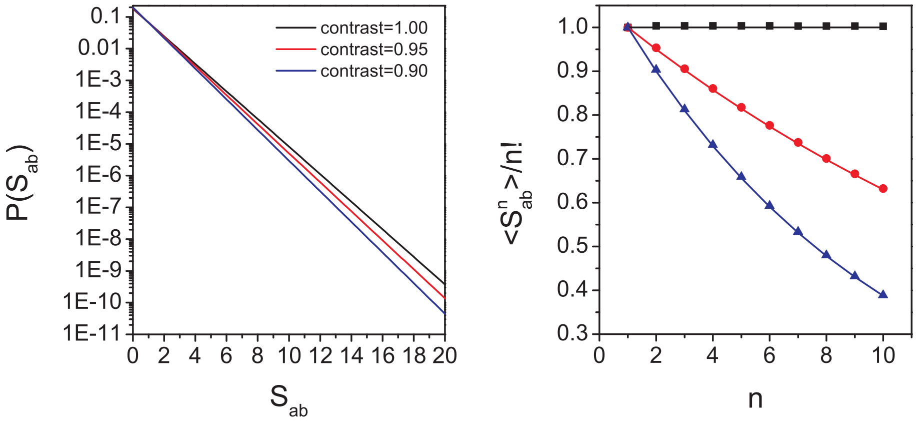

Figure 3.1: Left:Rayleigh law distributions of S_{ab} with three different values of contrast. Right: Moment distributions calculated from the probability distributions (data points) and from Equation 3.2 with an adjustment for contrast (lines).

As one might expect intuitively, the contrast has the effect of reducing the width of the distribution. While this appears to be a small effect on the probability distribution for the contrasts shown, even a 5% change in contrast has a dramatic effect on the moment distribution. The prediction of diffusive theory is that the moments $< S_{ab}^N > /N! = 1$ for a 'perfect' contrast of 1. Therefore moments beyond the first moment (which just gives the average) below unity are a good indication of a reduced experimental contrast. The other experimental factor that can result in moments below unity is a limited data set size- as each moment gives the width of the distribution at a certain probability, if there is not enough data to capture the behaviour beyond that point the corresponding moment can go below 1. However, this predominantly effects higher order moments and with careful analysis the two effects can be decoupled.

3.1.3 Mesoscopic fluctuations

While g may be large for diffusive samples, it is nonetheless finite. This alters the relative fluctuations seen in transmission, as a lower number of independent transmission channels will result in greater relative fluctuations in the transmitted intensity. This is because as more independent random variables are combined, the relative impact of 1 channel on the transmission reduces. Consequently a correction of the order $1/g$ may be expected to both $Var[S_{ab}]$ and $Var[S_a]$, while the correction for $Var[S]$ would be of the order of $1/g^2$.

The theory for this was developed mainly in the 1990's, and is closely connected with the appearance of increased correlations in speckle pattern due to interference contributions as discussed in Chapter 1. At first distributions were derived from correcting the second moment only [67]. Equation 3.5 gives the Kogan & Kaveh distribution for $P(T_{ab})$ derived under this approximation [49]:

$$P(T_{ab}) \approx \int_0^\infty dv \ \mathrm{Exp}[-\frac{(v- <T_{ab}>)^2}{2(<T_{ab}^2>/2- <T_{ab}>^2)}]\frac{1}{v}\mathrm{Exp}[-\frac{T_{ab}}{v}]. \tag{3.5}$$

It is possible to express this distribution in terms of g by using the following identity for a waveguide geometry:

$$g \approx \frac{<T_{ab}>^2}{<T_{ab}^2> -2<T_{ab}>^2}. \tag{3.6}$$

By definition $<S_{ab}>=1$, so the distribution of $P(S_{ab})$ in terms of g takes a relatively simple form:

$$P(S_{ab}) \approx \int_0^\infty \frac{dv}{v}\mathrm{Exp}[-g(v-1)^2 - \frac{-S_{ab}}{v}]. \tag{3.7}$$

As the second moment has been corrected, Equation 3.7 is wider than the Rayleigh distribution with $Var[S_{ab}] \propto 1/g$. The effect is seen predominantly in the tail of the distribution, which has the form of a stretched exponential for $S_{ab} >> g$. This can be considered to be a second order approximation of the true distribution, while Rayleigh statistics gives the first order behaviour. The full distribution was derived by Nieuwenhuizen & van Rossum [50], given by Equation 3.8 for an incoming plane wave:

$$P(S_{ab}) = \int_0^\infty \frac{dv}{v} \int_{-i\infty}^{-i\infty} \frac{dx}{2\pi i} \mathrm{Exp}[-\frac{S_{ab}}{v} + xv - gln^2(\sqrt{1+x/g} + \sqrt{x/g})]. \tag{3.8}$$

As this is obtained by summing over all of the correlated Green's functions it is very general and applies to a three dimensional geometry. It also results in a stretched exponential tail, given by Equation 3.9. As corrections to higher order moments are considered, this tail is heavier than that obtained from Equation 3.7:

$$P(S_{ab}) = \mathrm{Exp}[-2\sqrt{gS_{ab}}], S_{ab} >> g. \tag{3.9}$$

It is therefore possible to measure the number of transmission channels by fitting the distribution of the speckle intensity. A low number of independent transmission channels leads to a distribution with a much heavier tail than the Rayleigh distribution. Due to the equivalence between independent transmission channels and effective conductance discussed in Chapter 1 and invoking the Thouless criterion for Anderson Localisation of $g < 1$ [68], the statistics of the transmitted intensity is a strong tool for experimentally investigations of the localisation transition. Consequently this approach has been used to demonstrate localisation of microwaves in waveguides [31] and acoustic waves in a 3D slab geometry [30]. While it is mainly the statistics of the speckle intensity that have been discussed above, those of the total transmission are closely related and can also be used to find g.

From an experimental perspective it is sometimes cumbersome to fit the full probability distribution of every data set in order to detect a trend. It can be useful in the first instance to calculate a single moment of a distribution, such as the variance. There are a set of simple predictions from the theory that experimental results can be easily compared to. For the speckle intensity fluctuations:

$$Var[S_{ab}] = 1 + \frac{4}{3g}. \tag{3.10}$$

Additional fluctuations due to a finite g occur on top of the classical fluctuations of order unity. This holds generally as it is purely a result of the number of transmission channels contributing to the speckle. For the total intensity fluctuations:

$$Var[S_a] = \frac{2}{3g}. \tag{3.11}$$

This is for single channel illumination (plane wave), and does not hold if there are more than one incident channel. In the limit in which all incident channels are excited and the 'total transmission' becomes the conductance, which is expected to have fluctuations of the order $1/g^2$. For a single incident channel experiment, $Var[S_{ab}]$ can be related to $Var[S_a]$ in order to give a simple measure of the consistency between the two approaches:

$$Var[S_{ab}] = 2Var[S_a] + 1. \tag{3.12}$$

While these results were first derived using a diagrammatic approach to finding correlated Green's functions as in Chapter 1 [41], they have since been obtained under the framework of random matrix theory [69].

3.2 Experimental method

In the experiments, the light transmitted through the nanowire samples pressed against a glass cover slip was collected using a high-NA transmission microscope, shown in Figure 3.2. By displacing the sample across the focus using an computer controlled motorised stage, the speckle from many different sample positions was collected to obtain reliable statistics. This is an important point for such experiments, as distributions calculated from a single speckle pattern are not necessarily representative and in general do not contain enough information to calculate the higher moments corresponding to rare events.

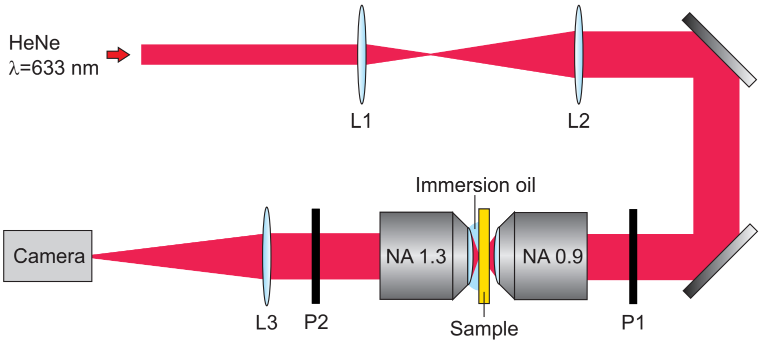

Figure 3.2: Setup used to characterise the intensity fluctuations of transmitted speckle patterns.

Polarisers P1 and P2 are used in the setup to investigate only 1 ingoing and 1 outgoing polarisation channel. This reduces the number of degrees of freedom, increasing the contrast of the transmitted speckle. Lenses L1 and L2 form a beam expander to fill the aperture of the objective, while L3 (focal length = 200 mm) images the speckle onto the camera (AVT Stingray F-033). A focal length of 200 mm was chosen for L3 in order for the speckle pattern to be over-sampled (i.e. an individual speckle is the size of a few camera pixels). This is an important point, as the contrast of a speckle pattern drops dramatically if it is under-sampled. A Helium-Neon (HeNe) laser was chosen for use due to its narrow line width and relatively good stability. Typically data sets consisted of images of the transmitted sample for between 500 and 10 000 separate sample positions, which were analysed using a Matlab script.

As well as the sample stage being mechanised, the focusing objective was also mounted on a computer controlled stage. By performing controlled displacements of the objective, the size of the sample illumination could be varied. As the number of transmission channels is expected to increase linearly with the illumination area, A, many and few channel statistics were compared on the same sample positions. Examples of the typical raw data obtained from the experiment are given in Figure 3.3 for the cases of the smallest possible incident focus ('in focus') and with the objective displaced 25 μm away from this position ('out of focus').

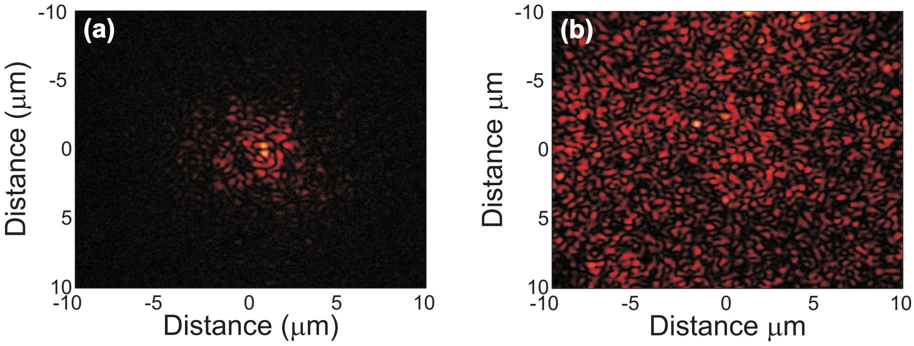

Figure 3.3: Typical images of speckle patterns transmitted through sample 3 for the in (a) and out (b) of focus cases.

The experiment differs slightly from the angular geometry often considered in the theory in that the speckle measured is in real space. However, this does not significantly alter the probability distributions discussed above, only modifying the definition of ingoing and outgoing channels (i.e. the subscripts a and b describe spatial rather than angular mode) . In order to assess relative fluctuations in intensity, some processing of the raw data was required. First a constant average background was subtracted from each image, which were then normalised to an ensemble average image to obtain $S_{ab} = T_{ab}/ < T_{ab} >$. This required a choice of an area of interest (AOI) from the image for analysis, as towards the edge of the speckle pattern the average intensity drops below the level of noise of the camera, distorting the statistics. The radius of the AOI was decided by the distance from the center of the average image corresponding to a drop of 50% in intensity for investigating the spatial speckle fluctuations. A larger AOI out to an intensity drop of $1/e^2 \approx 13.5\%$ was used for summing over in order to obtain the total intensity S_a. This larger area is used because it is important to capture a large portion of the transmitted light to reliably measure the total transmission, and by summing over many camera pixels the effect of noise should cancel out.

3.3 Mesoscopic statistics in nanowire mats

3.3.1 Spatial intensity fluctuations

As a first investigation, the probability distributions of the transmitted speckle intensity S_{ab} through samples 1, 2 and 3 (1.5, 4.5 and 6 μm thick respectively) were compared using a tightly focused illumination, as shown in Figure 3.4.

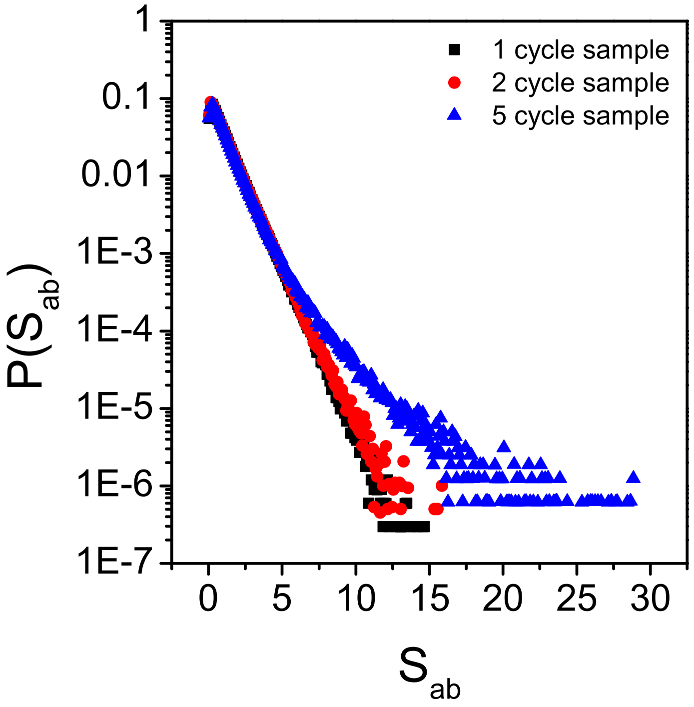

Figure 3.4: Histogram of $P(S_{ab})$ for nanowire samples of different thickness.

As the thickness of the nanowire mats increases, the relative fluctuations in the speckle intensity also increase. This is in agreement with the expectation for a disordered waveguide that $g \propto 1/L$ as a larger system results in a higher probability of crossing light paths. The distributions in Figure 3.4 are from scans over 1000 sample positions. In order to get a reliable measure of mesoscopic fluctuations, it is desirable to take much larger data sets. This is especially important for looking at effects in the tail of the distributions which correspond to rare events. In Figure 3.5 $P(S_{ab})$ is plotted for sample 3 for 12 000 sample positions separated by 1 μm in and out of focus.

Considerably greater fluctuations are seen in focus. This is in agreement with expectations, as a larger illumination size would result in more transmission channels, resulting in lower relative fluctuations. While the out of focus data is reasonably close to the prediction of diffusive Rayleigh statistics, the in focus data shows a large deviation from this behaviour due a low number of transmission channels. It can be seen from the moments of the distributions shown in Figure 3.5 (b) that moments 2-6 of the out of

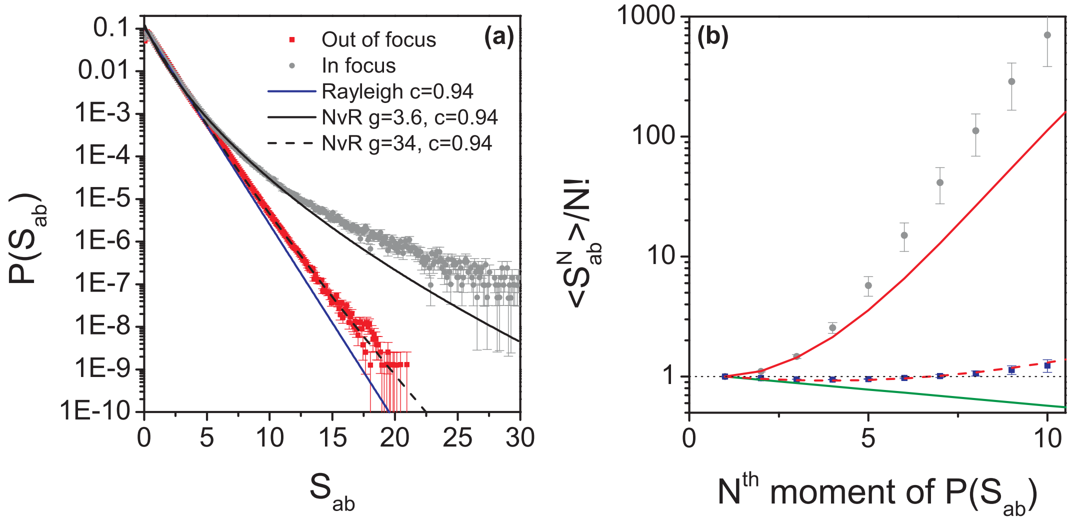

Figure 3.5: (a) Histograms of $P(S_{ab})$ transmitted through the 6 μm thick nanowire sample 3. Lines denote the expected Rayleigh law with a reduced contrast of 0.94 and fits to the mesoscopic theory of Nieuwenhuizen & van Rossum (NvR) with $g = 3.6$ and $g = 34$. (b) Moments calculated from the distributions in (a).

focus distribution are below 1. As discussed above, this is a signature of a reduced experimental contrast. Furthermore, the out of focus distribution cannot be described by Rayleigh statistics corrected for a contrast lower than one due to its higher moments.

The out of focus $P(S_{ab})$ distribution was fitted with the mesoscopic theory of Nieuwenhuizen & van Rossum (NvR) [50]with the contrast, C, and and number of independent transmission channels, g, as fitting parameters. Values of $c = 0.94$ and $g = 34 \pm 2$ were found. A contrast of 0.94 is reasonable for this experiment, and the fit describes even the higher moments relating to rare events in the tail of the distribution well. Fitting the in focus distribution with the contrast fixed at 0.94, a much lower value of $g = 3.6 \pm 0.1$ was found. This indicates that the transmission is described, on average, by less than 4 independent channels, a record low for a 3D disordered photonic medium and close to the Anderson localisation transition as defined by the Thouless criterion.

While the first few moments of the in focus distribution are well described by the fit, the theory clearly underestimates the tail of the distribution. While it is the lower moments that have the higher statistical relevance, it is interesting to investigate the possible causes of this effect. Similar behaviour was seen in a recent microwave experiment by Höhmann et al. and attributed to rare events known as 'freak waves' [70]. These are analogous to the spontaneous appearance of rouge waves in the ocean [71], and have also been observed in optical fibers [72]. Following the analysis of Höhmann et al. we find that this anomalously large tail is attributable to a small number of sample positions ($< 1\%$) with high intensity speckles termed 'hot spots'.

A hot spot is defined as a value of S_{ab} greater than a threshold. The setting of this threshold at a reasonable value is important, as mesoscopic effects also result in large intensity fluctuations. Considering the number of individual speckles measured in the experiment, a threshold of $S_{ab} > 20$ was set for hotspots. The distribution of $P(S_{ab})$ over 1000 sample positions is compared with the same data excluding positions with hot spots and for the hot spot positions themselves in Figure 3.6 (a). It should be emphasised that in this analysis the entire images containing the hot spots were excluded.

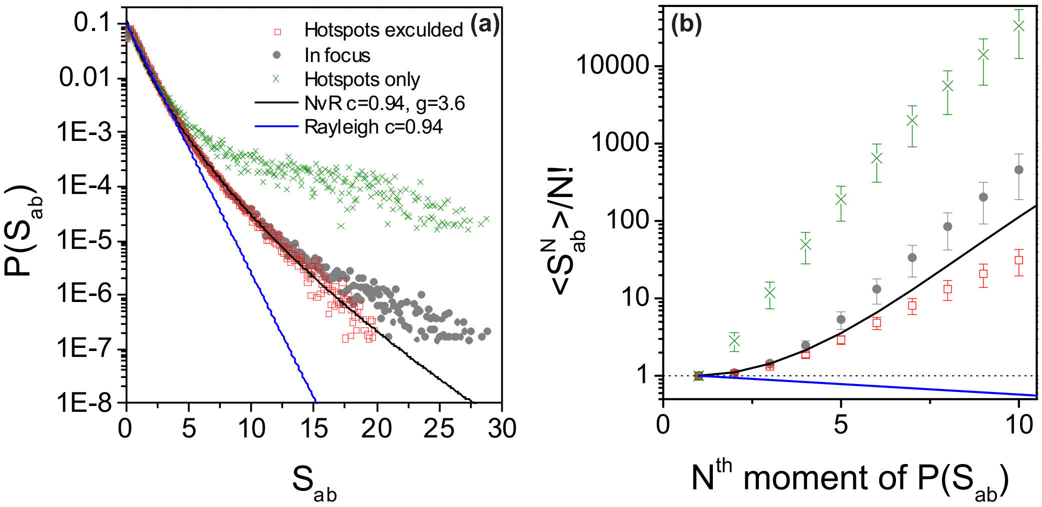

Figure 3.6: (a) Histogram showing the effect of hot spots on the distribution of $P(S_{ab})$. (b) Moments of the distributions shown in (a).

Excluding the hot spots from the distribution, a much better agreement with the theory is obtained in the slope of the tail. It is clear from Figure 3.6 (b) that artificially truncating at $S_{ab} = 20$ has a considerable impact on the higher moments of the distribution. The second moment is almost unchanged, however, showing that the comparison with the mesoscopic theory for $g = 3.6$ is still valid. This analysis suggests that freak waves are a plausible explanation for the observed behaviour, although it should be stressed that they are still not well understood and a subject of ongoing research.

3.3.2 Focus dependence

Increasing the size of the illumination results in lower fluctuations due to the larger number of transmission channels. Figure 3.7 shows the focus dependence of the crossing probability $1/g$ obtained from fitting the moment distribution.

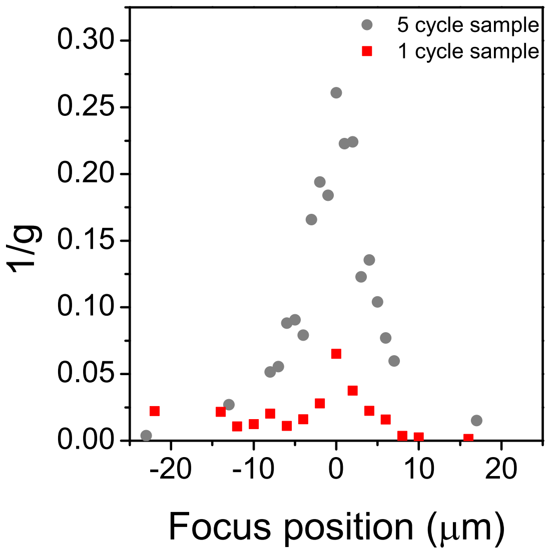

Figure 3.7: Dependence of 1/g on focus displacement (movement of focusing objective away from focal point) for samples 3 and 1.

As expected, the crossing probability increases sharply as the focal spot decreases in size, and is much lower for the thinner nanowire sample. It is of interest to compare g as a function of illumination size with a theoretical expectation. However, the waveguide prediction of $g \propto w^2$, is not suitable as it does not account for the transverse spreading of light occurring in a slab geometry. An attractive solution for this problem is the 'expanding waveguide' model of Scheffold et al. [52] in which considering as a series of infinitesimally thin waveguides with a depth dependent width $w(z)$.

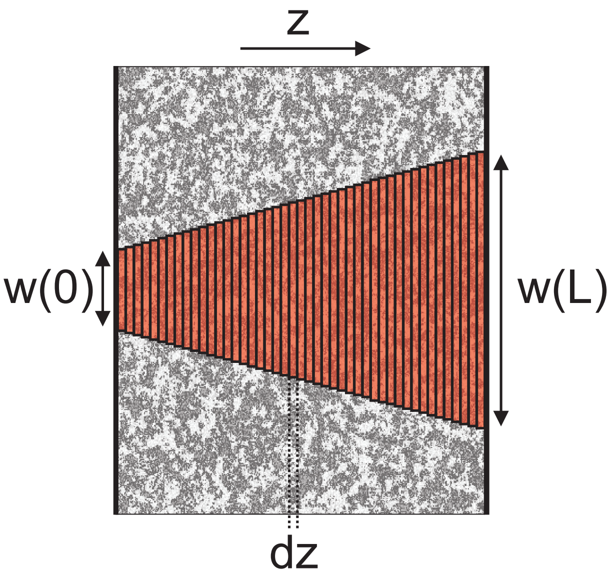

Figure 3.8: Diagram of the expanding waveguide model.

In this approach, an effective probability of light paths crossing can be defined as a function of z assuming a circular spot:

$$1/g(z) = \frac{1}{A(z)k^2 l} = \frac{4}{\pi k_n^2 l w^2}. \tag{3.13}$$

The interpretation of this statement is that as the light spreads within the slab, the probability of light paths interfering drops sharply. As a result, unlike a waveguide, increasing the thickness of the slab past a certain point has little effect and g is largely defined by the size of the incident illumination. If the growth of $w(z)$ with z is assumed to be linear, this can be defined in terms of the initial beam waist $w(0)$:

$$\frac{1}{g(z)} \propto \frac{1}{(w(0)+z)^2}. \tag{3.14}$$

The dependence of the overall crossing probability for the slab on w and L can then be found by integrating over z:

$$\frac{1}{g} = \int_0^L dz \frac{\lambda^2}{\pi^3 n^2 l (w(0)+z)^2} = \frac{4}{\pi k_n^2 l} \frac{1}{w(0) + \frac{w(0)^2}{L}}. \tag{3.15}$$

It can be seen that for $w(0) << L$ that a different dependence of the crossing probability in the slab of $1/g \propto 1/w(0)$ is obtained. However, this approach has the drawback of the crossing probability going to infinity as the beam waist goes to zero, which is unphysical. The full behaviour for a slab geometry was described by García-Martn et al. [73] by defining an effective waveguide length $L_{eff} \approx w(0)$ in which the crossings take place. The behaviour found is given in Equation 3.16.

$$\frac{1}{g} = \frac{3}{4}(\frac{9}{8})^2 \frac{[1 + L_{eff}/2]}{[1 + 3/4L_{eff}]^2} \frac{1}{k^2 l^2} \tag{3.16}$$

The illumination size as a function of objective displacement was calibrated using a camera monitoring the diffuse reflection. Although a high NA objective was used, it was found that minimum the beam waist obtained was found to be around 1 μm, considerably larger than the diffraction limit. The reasons for this are spherical aberrations in the GaP substrate limiting the NA and the diffuse spreading of the beam waist due to multiple scattering.

In Figure 3.9 the crossing probability, $1/g$, of sample 3 is compared to the theory of í et al. as a function of the size of the incident focus. It can be seen that the theory reasonably describes the behaviour with an effective length of $L_{eff} = 0.29w(0)$, which is close to the predicted value of $L_{eff} = 3/8w(0)$. However, the value of $kl = 1.3$ obtained by the fit is low compared to an estimate based on the mean free path and effective refractive index of $kl \approx 4$. This reflects that the magnitude of the effect is greater than

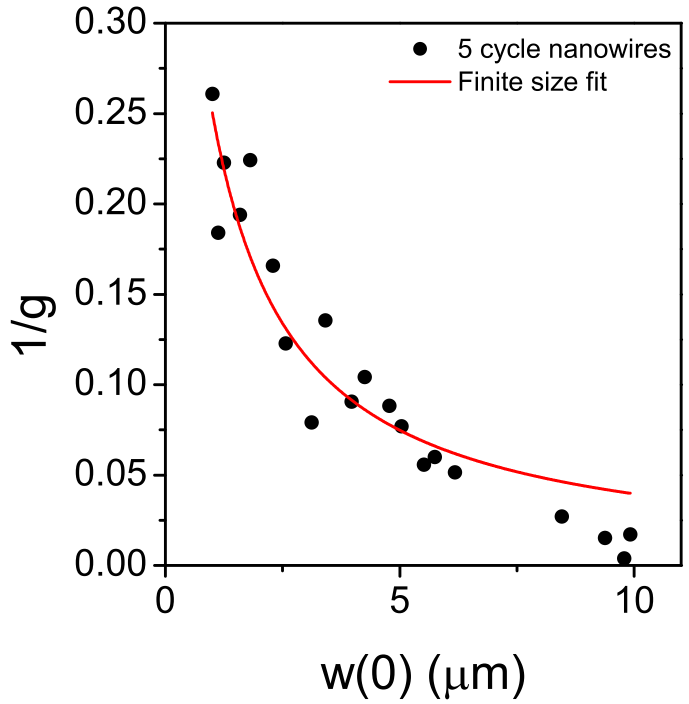

Figure 3.9: Comparison of crossing probability $1/g$ of sample 3, fitted by the theory of í et al.

predicted by theory, possibly due to the theory not taking into account the problem of a Gaussian beam waist.

3.3.3 Total transmission fluctuations

As discussed in the theory section, the total transmission S_a also exhibits fluctuations due to a limited number of transmission channels that are closely related to those of the speckle intensity S_{ab}. By summing over the collected light, the total transmission statistics through the nanowire samples were assessed simultaneously to the spatially resolved transmission. Figure 3.10 shows the total transmission data obtained over 1000 sample positions.

Again, it is clear that a smaller illumination results in much greater fluctuations. It was found that sample variations lead to fluctuations in the intensity over a longer range than the fluctuations due to mesoscopic effects. Consequently, they were successfully divided out using a moving average with a range of 10 μm. Figure 3.11(a) shows the probability distributions of the total transmission obtained from the same data used to obtain g from fitting $P(S_{ab})$ sample 3 (Figure 3.5).

The variance of the both the in and out of focus distributions of S_a yields values of g higher than those obtained from fitting the $P(S_{ab})$ distributions. Using the relation for

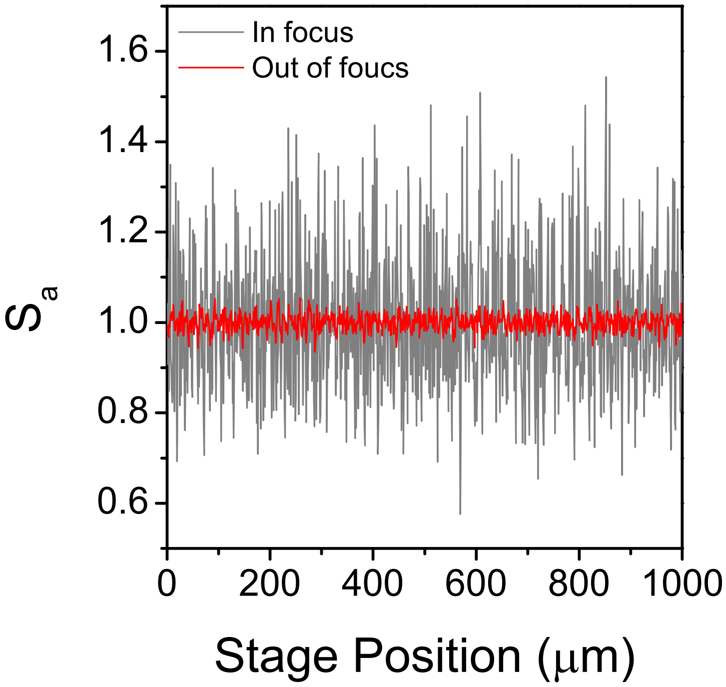

Figure 3.10: Total transmission as a function of sample displacement in and out of focus. Data has been normalised to a moving average with a span of $10\mu m$ to remove fluctuations due to the sample.

a single channel plane wave illumination $Var[S_a] = 2/3g$, a value of $g = 27$ is found in focus. While the contrast is not a consideration for the total transmission fluctuations, this apparent discrepancy is likely due to differences between the theoretical picture and the experimental situation. The first point to consider is that the illumination is not a plane wave. A Gaussian beam profile is predicted to result in reduced fluctuations [50], resulting in a different relation $Var[S_a] = 1/3g$, giving a value of $g = 13.5$ from the total transmission.

Additionally, due to the diffusive spread of the incident focus and the spherical aberrations in the GaP slab the illumination is not diffraction limited and therefore can not be considered to be a single channel. This changes the statistics as the total transmission measured is summed both over outgoing and ingoing channels. If all possible channels were excited (ie diffuse illumination) the optical conductance s would be obtained, which has a characteristic variance of $16/45g^2$ [50]. The experimental case lies in between these two cases with an intermediate variance. It can be seen that while a Gaussian distribution describes the out of focus data well, the in focus data is clearly skewed and resembles a log normal distribution, as predicted for the conductance when approaching the Anderson localisation transition [74].

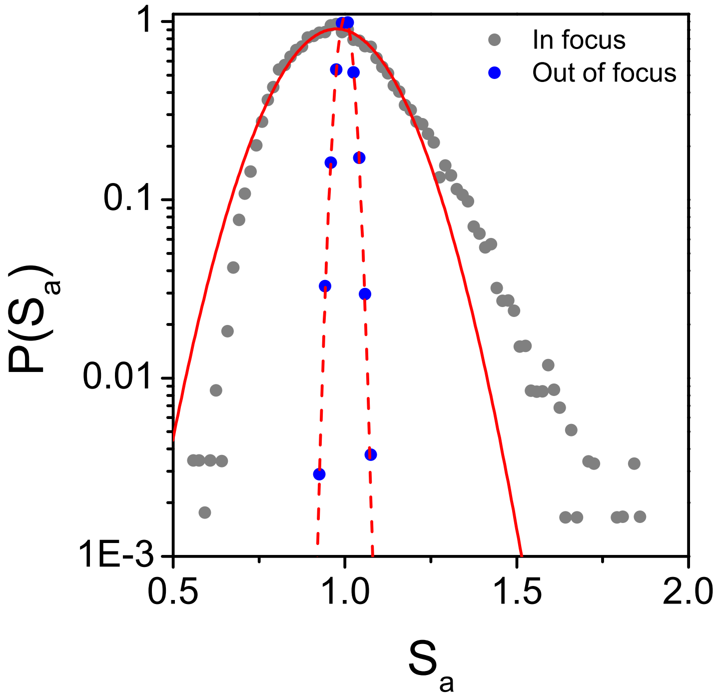

Figure 3.11: Probability distribution of S_a for sample 3 in and out of focus, with Gaussian fits of variance 0.025 and 4.2×10^{-4} respectively.

3.4 Mesoscopic statistics in layers of Zinc Oxide

As has been shown in chapter 2, the nanowire mats are an exceptional material which at the moment require an involved and relatively expensive manufacturing technique. This is in contrast to the 'white paint' which is commonly used to study multiple scattering effects. Therefore it is of interest to also investigate the transmission statistics of such samples in the same setup used for the nanowire investigations. The samples used consist of spray painted slabs of ZnO nano-particles on glass cover slides produced by Elbert van Putten and Duygu Akbulut at the University of Twente. The mean free path of such layers was previously measured in Twente to be approximately 0.6 μm. This is considerably higher than that of the nanowire samples used, consequently lower fluctuations in the statistics are expected. 3 different layer thicknesses (6.8, 11.2 and 30 μm) were used to further investigate the expectation that crossing light paths occur mainly in the first few mean free paths of a scattering medium.

As with the nanowires, it can be seen in Figure 3.12(a-c) that there is a difference in behaviour in and out of focus for all of the ZnO layers tested. However, the effect is noticeably smaller than that of the nanowires, as expected due to their comparatively low photonic strength. The difference can be seen more clearly in the distributions of the moments (Figure 3.12(d-f)). Fitting the histograms using the full mesoscopic theory was inaccurate due to the relatively small weight of the tail, which is where the effect is

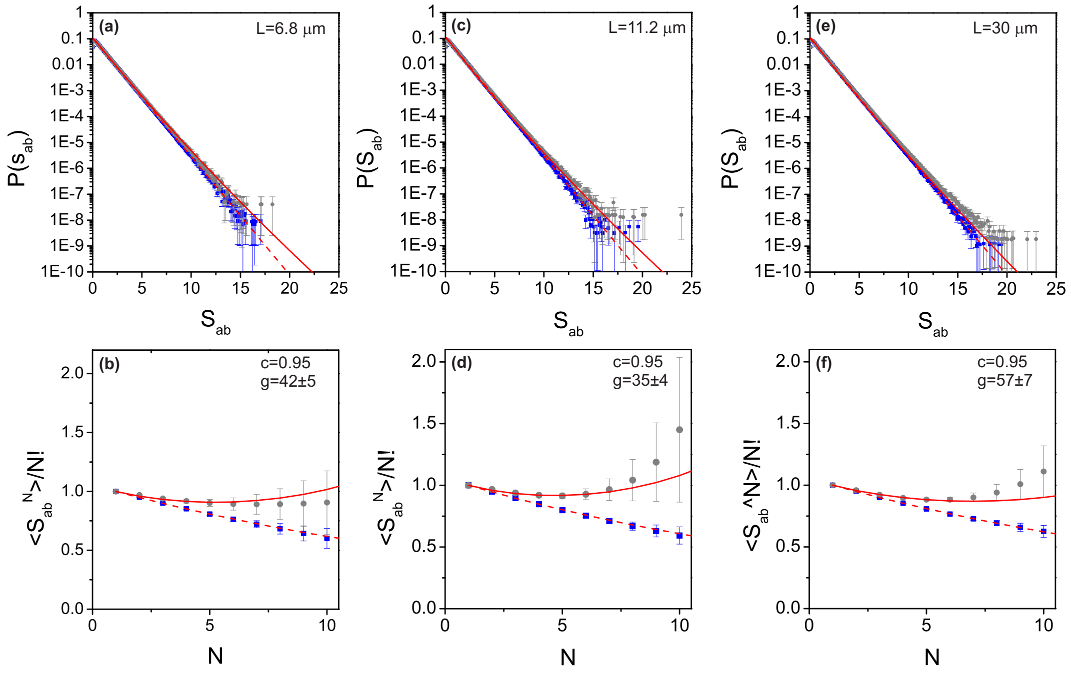

Figure 3.12: (a-c) Histograms of the distribution of S_{ab} for different thicknesses L of ZnO both in (grey) and out (blue) of focus . (b-f) Corresponding moment distributions. Dashed lines indicate expected diffusive behaviour with a contrast of 0.95, while solid lines show the mesoscopic NvR distribution for the fitted value of g.

seen. Instead, an approach of fitting the moments of the Kogan & Kaveh distribution (Equation 1.6) [49] was adopted. By fitting the out of focus moments, a contrast of 0.95 was found. This is slightly higher than the value found in the nanowire experiments, and can be attributed to small improvement in the setup (using larger optics to reduce clipping). By fitting the moments of the in focus distributions, values for g of $42 \pm 5, 35 \pm 4$ and 57 ± 7 were found for the 6.8, 11.2 and 30 μm samples respectively [4].

While the effective dimensionless conductance g of the ZnO layers is a factor of 10 higher that that measured with the nanowires, it is still considerably lower than typical diffusive media. No clear dependence on the thickness of the layer was seen, supporting the interpretation that mesoscopic effects are dominated by the first few mean free paths inside the sample. As with the nanowire samples, the total transmission through the layers was also assessed (Figure 3.13).

Using the relation $Var[S_a] = 2/3g$, an average value of $g = 73$ is obtained from the total transmission histograms. In comparison to the average value of $g = 45$ obtained from the S_{ab} histograms, the agreement between the two values is significantly better that that seen for the nanowires. Indeed, using the relation for a Gaussian focal spot $Var[S_a] = 1/3g$ [50] a value of $g = 36.5$ is found, at which point the difference between the two is likely to be within the margin of error. This better agreement can be attributed to being able to focus light directly on the ZnO layer without having to pass through

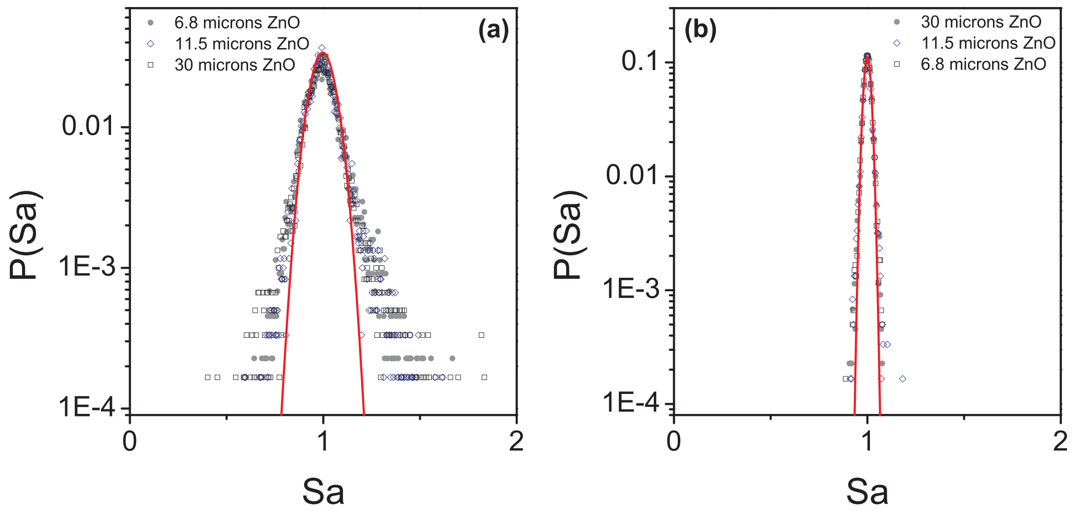

Figure 3.13: Histograms of the total transmission through ZnO layers for (a) tightly focused illumination and (b) with the illuminating objective displaced by 25 μm. Lines are Gaussian fits of the average histogram characterised by variances of 9.1×10^{-3} and 3.7×10^{-4} respectively.

a substrate as with the nanowires, which caused significant spherical aberrations. This would result in an illumination closer to the single incident channel case.

3.5 Statistics nanowires grown with 2 nm gold film

As the 25 and 30 μm thick samples 5 and 6 were found to have a large dip in transmission around 740 nm in Chapter 2, it is interesting to investigate the transmission statistics in this region. A tunable external cavity diode laser with a center wavelength of 770 nm (Thorlabs TLK-780M) was used instead of the HeNe used previously. This allowed some tuning of the laser wavelength over the long wavelength side of the dip in transmission, with a minimum achievable wavelength of 760 nm. The distributions of S_{ab} for samples 5 and 6 are shown in Figure 3.14.

Due to the thickness of the samples it was not possible to compare in and out of focus cases as in previous experiments as the out of focus speckle pattern was too large to be fully captured by the camera. However, unlike previous experiments, statistics at different wavelengths could be compared. No significant difference is seen in the statistics at 772 and 760 nm for either sample. As this is at the edge of the dip in the total transmission, if there was a localisation effect, some difference between the two may have been expected.

Fitting the distributions with the mesoscopic theory of NvR, it is found that the distributions can be described by $g = 15$ and $g = 25$ for samples 5 and 6 respectively. These measurements have been taken over only 1000 sample positions so the uncertainty on these values is larger than for the other studies in this chapter. However, the

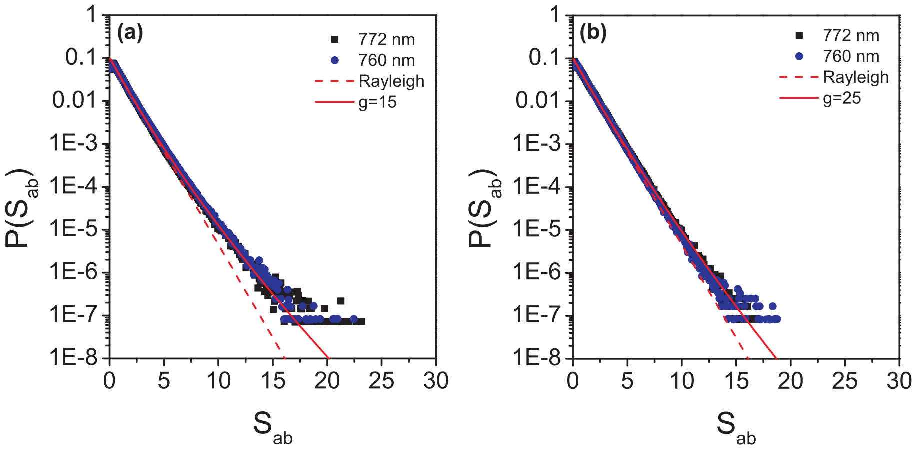

Figure 3.14: Distribution of S_{ab} for the (a) sample 5 and (b) sample 6. Solid red lines show NvR fits, dashed lines indicate Rayleigh statistics.

distributions provide a strong indication that there is no Anderson localisation in these samples since they are further from the localisation transition than sample 3, which is much thinner. Interestingly, the 25 μm thick sample 5 shows stronger fluctuations than the 30 μm thick sample 6. This may be an indication of absorption plays a role, as its effect will be greater in the thicker sample. As discussed previously, absorption reduces relative fluctuations in speckle intensity towards the diffusive case as long lived light paths characteristic of mesoscopic effects are suppressed.

3.6 Summary

The statistics of the transmission through both disordered nanowire mats and layers of ZnO were analysed for mesoscopic effects. The nanowire mats exhibited strong fluctuations in transmission characterised by a minimum of only 3.6 ± 0.1 independent open transmission channels, a record low for 3D photonic media and close to the Anderson localisation transition occurring at $g = 1$. The fluctuations in the tail of the spatial intensity distribution were stronger than predicted by theory, and possibly attributed to the interesting phenomena 'freak waves'. It was found that the theoretical expectation for the relation between the fluctuations of the spatial and total transmission did not hold, with the variance of the total transmission being a factor of 5.5 lower than predicted. This was attributed to experimental limitation resulting in a non-diffraction limited focal spot and consequently the illumination did not match the 'single channel' picture considered in theory.

Weaker mesoscopic effects were found in the ZnO samples due to their lower photonic strength, with an average of 37 ± 5 independent transmission channels found for the three different samples considered. No dependence of g was found on the thickness of the ZnO layers, despite a factor of more than 4 increase in layer thickness. This is in agreement with the prediction of Scheffold et al. [52] that in a slab geometry, mesoscopic effects are determined by the first few mean free paths of the sample due to the diffusive spreading of the light. Aside from testing this theoretical prediction, it was interesting to demonstrate mesoscopic effects in a material which is commonly used in scattering experiments due to its ease of manufacture and low cost.

The statistics of the thick nanowire samples found in Chapter 2 to have a striking dip in transmission around 740 nm were also investigated. While a laser at 760 nm rather than 740 nm was used, it was found that the fluctuations in transmission were less than that of the the 6 μm thick sample 3 and marginally greater than that of the ZnO samples. The lesser fluctuations for the thicker of these two samples is a possible indicator of absorption. While these samples show interesting behaviour that requires further investigation to understand fully, the evidence does not appear to support the interpretation that the dip in transmission through these samples at 740 nm is a signature of Anderson localisation.

Chapter 4

Mesoscopic Correlations

As well as resulting in large fluctuations in intensity, mesoscopic effects are also characterised by long range correlations in transmission. A simple explanation of the origin of these correlations is that the crossing of light paths results in two previously uncorrelated paths becoming linked. As the transmission statistics indicate that the nanowire samples investigated in Chapter 3 have a minimum of only 3.6 ± 0.1 independent transmission channels, they should also exhibit strong correlations. In this chapter both the spatial and frequency correlations of the nanowire mats are investigated. The demonstration of strong mesoscopic correlations in a 3D photonic media may open the exciting possibility of harnessing such effects in applications such as imaging through scattering media. The correlations of light transmitted through random media are of current active interest, with a new type of correlation '$C^{(0)}$', dependent on fluctuations in the local density of states [75, 76], recently having been demonstrated for acoustic waves [77].

4.1 Spatial correlations

4.1.1 Memory effect

While speckle is random in appearance, it is the presence of short range '$C^{(1)}$' correlations which give it its characteristic grainy appearance, which are a result of the speckle pattern transmitted through random media having a characteristic spectral and spatial width. This width is a small range of incident positions or frequencies over which the induced dephasing is not enough to completely change the interference between different light paths. This leads to the striking 'memory effect', in which a small shift in the angle of incident light to a diffusive medium does not destroy the speckle pattern but instead shifts the transmitted speckle by an equal angle [7]. This occurs even after a large number scattering events which would reasonably be expected to completely scramble any information about the incident light. The form of the $C^{(1)}$ correlation of transmitted speckle for position shift Δr is given in Equation 4.1 [41]:

$$C^{(1)}(\Delta r) = \left(\frac{sin[k\Delta r]}{k\Delta r}\right)^2 e^{-\Delta r/l}. \tag{4.1}$$

This correlation is expected to be independent of whether the detector or source is displaced by Δr. The memory effect through the nanowire mats was assessed with the same experimental setup used to measure intensity fluctuations in Chapter 3. Images were taken of the transmitted speckle while the sample was shifted by small increments. A large incident illumination was obtained by displacing the focusing objective by 25 μm in order to reduce the contribution of the mesoscopic effects found in Chapter 3, and all images were normalised to the ensemble average. Several images from a typical data set are shown in Figure 4.1 in which the sample was shifted in steps of 200 nm. It can be seen that the speckle completely changes within 600 nm, evidence of the short range nature of the $C^{(1)}$ correlation.

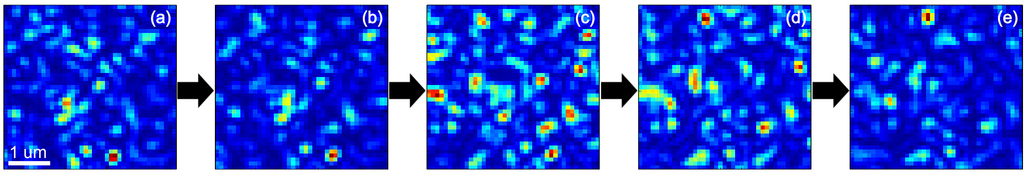

Figure 4.1: Images of transmitted speckle through the 5 cycle nanowire sample with a large illumination for sample positions separated by 200 nm. Arrows indicate the direction of the displacement.

The experimental correlation between images $I_0(x, y)$ and $I_{\Delta r}(x, y)$ was calculated as shown by Equation 4.2, where (x, y) is the spatial coordinate of the image and N is the normalisation to the number of points:

$$Corr[I_0, I_{\Delta r}] = \frac{\sum_{x,y}(I_0(x,y) - <I_0(x,y)>)(I_{\Delta r}(x,y) - <I_{\Delta r}(x,y)>)}{\sum_{x,y} <I_0(x,y)><I_{\Delta r}(x,y)>}. \tag{4.2}$$

The experimental correlation is normalised to the average rather than the variance. This is so that the $\Delta r = 0$ value of the function returns the variance of the image rather than unity, which is useful for comparison with the speckle fluctuations measured in Chapter 3.The correlation of the speckle equivalent to shifting the detector rather than the sample could be obtained using a Matlab script to calculate the correlation between a speckle pattern and a displaced version of itself. Figure 4.2 compares the experimental correlation obtained over 1000 sample positions separated by 100 nm using an out of focus illumination for both source and detector displacement to the prediction of Equation 1.1.

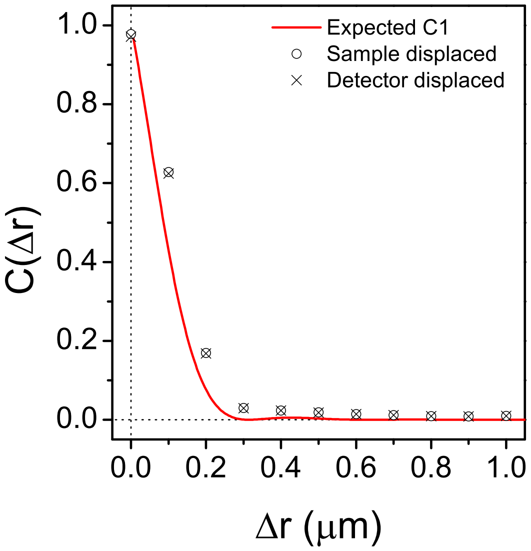

Figure 4.2: Spatial correlation of transmitted speckle through sample 3 with an out of focus illumination compared to the expected $C^{(1)}$ from theory.

It can be seen that, as expected, there is negligible difference between the correlation displacing the source and displacing the detector artificially through post processing of the images. As a result, correlations can be calculated from data sets with larger steps in the displacement of the sample. The experimental correlation decays extremely quickly, however, it is slightly longer in range than the theoretical prediction based on l=0.2 μm, $k = 10\mu\mathrm{m}^{-1}$ and a contrast of 1. While in Chapter 4 a g of around 30 was found for this sample with an out of focus illumination which is low for a 3D photonic media, this is unlikely to be a mesoscopic effect. Instead, it is suggested that this broadening is due to the diffraction limited detection.

4.1.2 Mesoscopic correlations

Additional correlations in speckle patterns arise due to crossing light paths, and are closely related to the mesoscopic fluctuations discussed in Chapter 3. As in the analysis of mesoscopic effects in Chapter 1, speckle correlations can be considered as corrections to the classical correlation in the form of a power series in $1/g$, at least in the weak scattering limit. The overall speckle can then be expressed as:

$$C = C^{(1)} + \frac{2}{3g}C^{(2)} + \frac{2}{15g^2}C^{(3)}. \tag{4.3}$$

Here $C^{(2)}$ and $C^{(3)}$ are mesoscopic contributions resulting from the crossing of 1 and 2 light paths respectively, with amplitudes determined by the variance of the associated speckle fluctuations. In the diffusive case, the $C^{(1)}$ correlation dominates the correlation of the spatial speckle pattern. However, if all outgoing paths are summed over to give the total transmission the $C^{(1)}$ is averaged out and it is the $C^{(2)}$ contribution that dominates. This is because after a crossing event propagating light paths are correlated and survive averaging. Similarly, if all ingoing and outgoing channels are summed over the $C^{(3)}$ term that dominates in the optical analogue of universal conductance fluctuations [47]. These mesoscopic correlations are of longer characteristic range than the classical $C^{(1)}$ term. Due to the dependence on g, it is expected that the $C^{(2)}$ and $C^{(3)}$ contribution would be much larger for a small illumination. The experimental correlations obtained using in and out of focus illuminations are compared in Figure 4.3(a).

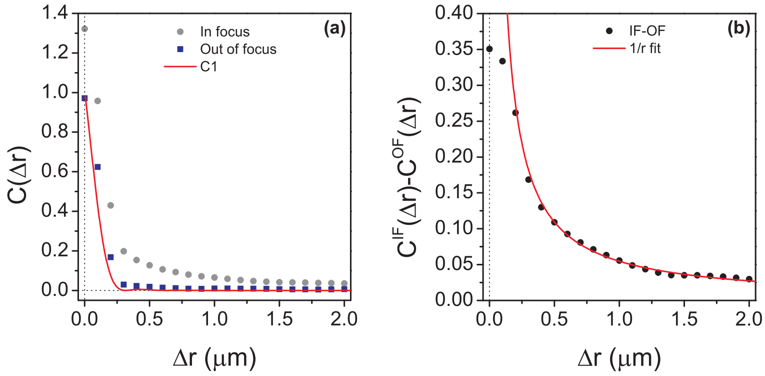

Figure 4.3: (a) Spatial correlation of the speckle transmitted through sample 3 for in and out of focus illuminations. (b) Difference between in and out of focus spatial correlations, fitted by a $1/\Delta r$ decay as expected for a $C^{(2)}$ correlation.

From the y intercept of the speckle correlations, it is clear that the variance of the speckle is much larger for the in focus illumination. The value of g obtained from this should be comparable to that obtained for the same sample in Chapter 3. Again, the contrast of the system should be taken into account, which can be done in this case by normalising to the variance of the out of focus data. This value is 0.97, slightly higher than the value for the contrast used in Chapter 3, which can be attributed to uncorrelated noise gathering in the first data point of the correlation. The corrected variance in focus is then 1.37, which using the relation $Var[S_{ab}] = 1 + 4/3g$ returns $g = 3.6$. This is in excellent agreement with the result from fitting the probability distribution of the spatial speckle.

It can also be seen that the in focus correlation exhibits a significant long range component compared to the out of focus data. In order to isolate this effect, the out of focus data is subtracted in Figure 4.3(b). The assumption here is that the out of focus data approximates the $C^{(1)}$ of the sample, which is acceptable as there is a factor of ≈ 10 larger g out of focus. The resulting plot has a different behavior to a $C^{(1)}$ type correlation, and its long range decay can be reasonably described by $C(\Delta r) \propto 1/\Delta r$, as expected for $C^{(2)}$ type behavior [46]. The approach of subtracting $C^{(1)}$ to view the $C^{(2)}$ behavior has previously been adopted in microwave measurements [78].

While the evidence from the spatial correlations is reasonably strong that the nanowire mats exhibit long range mesoscopic fluctuations consistent with the value of g found from fitting the probability distribution of S_{ab}, it is difficult to fully fit $C^2(\Delta r)$. As a result it is also difficult to assess the potential contribution of $C^{(3)}$, which is expected to have a small but possibly measurable amplitude of 10^{-2} in focus. The correlation of the total transmission, which excludes the $C^{(1)}$ correlation, is investigated later in this chapter.

4.1.3 Non-universal correlations

As well as mesoscopic terms, it has been suggested that there is an additional 'infinite range' contribution to the speckle correlation due scattering events in the vicinity of the source [75]. This non-universal term, otherwise known as $C^{(0)}$, has been shown to be equivalent to fluctuations in the local density of states (LDOS) [76] and has recently been observed for acoustic waves around the Anderson localisation transition [77]. In this case the LDOS refers to the number of available modes in proximity to the source, determined by the local configuration of scatterers. The principle of the $C^{(0)}$ correlation is that fluctuations in the LDOS between different sample realisations result in additional correlations in the transmitted speckle when the source position is scanned. These appear to be infinite in range as the LDOS at the location of the source affects the entire transmitted speckle pattern. The expected value for $C^{(0)}$ is given in Equation 4.4 for scalar waves in an infinite random medium with white-noise disorder:

$$C^{(0)} = \frac{\pi}{kl_s}. \tag{4.4}$$

Assuming an effective refractive index of $n \approx 2$ for the nanowire mats and $l = 0.2$ μm, the expected contribution of the LDOS from Equation 4.4 would be $C^{(0)} \approx 0.8$. Clearly no sign of such a large contribution has been seen in the previous analysis of the spatial correlations, however, as the value of kl for these nanowire layers is amongst the lowest available for photonic materials it is of interest to investigate whether any signs of a $C^{(0)}$ effect can be detected. Following the analysis of Hildebrand et al. [77], the $C^{(0)}$ contribution can be isolated by taking the difference between the spatial speckle correlation obtained scanning the source $C(\Delta r_s)$ to that obtained by scanning the detector $C(\Delta r_d)$. This is because keeping the source fixed does not produce any fluctuations in the LDOS in its vicinity, so this data contains only the information of the 'universal' correlations. Figure 4.4 shows the result of such analysis using both in and out of focus illumination for sample 3.

A small but clear difference can be seen between $C(\Delta r_s)$ and $C(\Delta r_d)$ which is greater for the in focus illumination. This could be explained by fluctuations in the LDOS being washed out for a larger illumination size. However, while there appears to be a

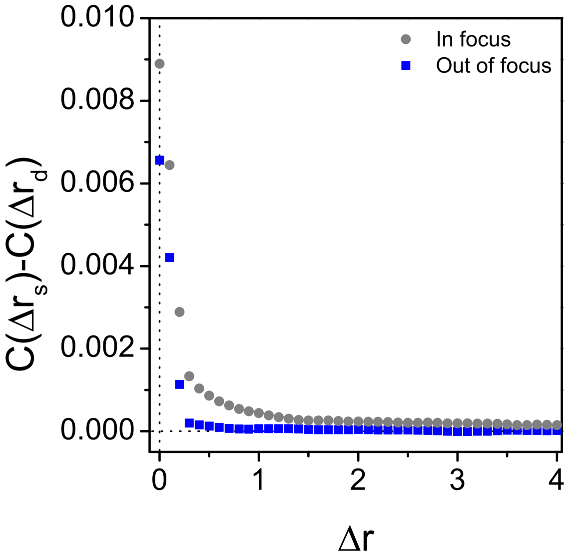

Figure 4.4: Plots of $C^{(0)}$ obtained experimentally by taking the difference between the spatial speckle correlation with detector or source fixed obtained through sample 3 for both in and out of focus illuminations.

long range component, the magnitude of this correlation is much lower than expected from Equation 4.4. This could be a result of the assumptions made in the derivation of the theory, specifically that of white-noise uncorrelated disorder. Additionally it could be argued that even in focus, the illumination cannot be considered as a point source resulting in an averaging out of LDOS fluctuations.

4.2 Spectral correlations

It is also of interest to characterise the spectral correlations $C(\Delta\nu)$ through the nanowire samples in order to find further evidence of mesoscopic effects. The expected spectral memory effect in the absence of internal reflections is given by:

$$C^{(1)}(\Delta\nu) = \frac{(L/\sqrt{2}L_\nu)^2}{cosh[L/\sqrt{2}L_\nu] - cos[L/\sqrt{2}L_\nu]}. \tag{4.5}$$

where $L_\nu = \sqrt{D/2\pi\Delta\nu}$ gives a spectral coherence length scale [41]. $C^{(1)}(\Delta\nu)$ has a dependence on the thickness L as it determines the dwell time of light within the medium, which can be inverted to obtain the spectral width. Given the high refractive index of the GaP nanowires, it is unrealistic to exclude internal reflections in these samples. It is well known that such reflections at both interfaces modify transport in strongly scattering media [79], and can crudely be considered to increase the effective length of the medium. This can be accounted for by including an 'extrapolation length' dependent on the reflection coefficient R at both surfaces [65], given by Equation 4.6:

$$z_e = \frac{2l}{3}\frac{1+R}{1-R}. \tag{4.6}$$

The $C^1(\Delta\nu)$ correlation including the effect of internal reflections is given by Equation 4.7 in the absence of absorption [51]:

$$C^{(1)}(\Delta\nu) = \frac{L^2}{z_e^2}\frac{cosh[\sqrt{2}z_e/L_\nu] - cos[\sqrt{2}z_e/L_\nu]}{cosh[\sqrt{2}L/L_\nu] - cos[\sqrt{2}L/L_\nu]}. \tag{4.7}$$

Experimentally, the spectral correlation of the transmitted speckle through the nanowire samples was obtained using the same setup as used in the spatial speckle correlations. A tunable external cavity diode laser (Thorlabs TLK-780M) with a central operating frequency of 770 nm was used instead of the HeNe operating at 633 nm. While this entails a change of the wavelength of the source, the behavior is not expected to be markedly different as the total transmission measured in Chapter 2 is relatively constant in this region. Figure 4.5 shows 3D plots of the spatial and spectral correlation $C(\Delta\nu, \Delta r)$ obtained over 1000 sample positions for sample 3.

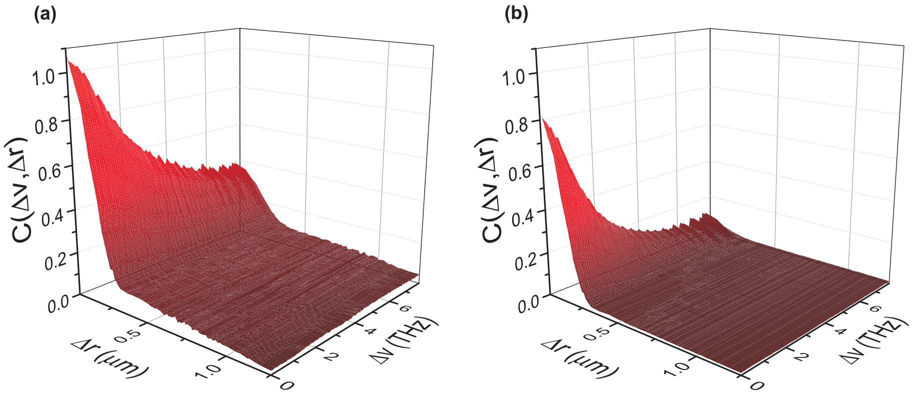

Figure 4.5: Experimental speckle correlation $C(\Delta\nu, \Delta r)$ sample 3 with (a) in and (b) out of focus illuminations obtained using tunable diode laser.

These plots show similar features to those found in the spatial correlations previously in that the smaller illumination results in much stronger long range correlations. The value of the variance is reduced compared to the investigations using the HeNe. This is attributed to a loss in speckle contrast due to the increase in wavelength and subsequent increase in the diffraction limit. It is clear that significant long range correlations also exist in the spectral correlations of the transmission. The in and out of focus spectral correlations are compared in Figure 4.6(a), with the spatial correlations plotted in Figure 4.6(c) for reference.

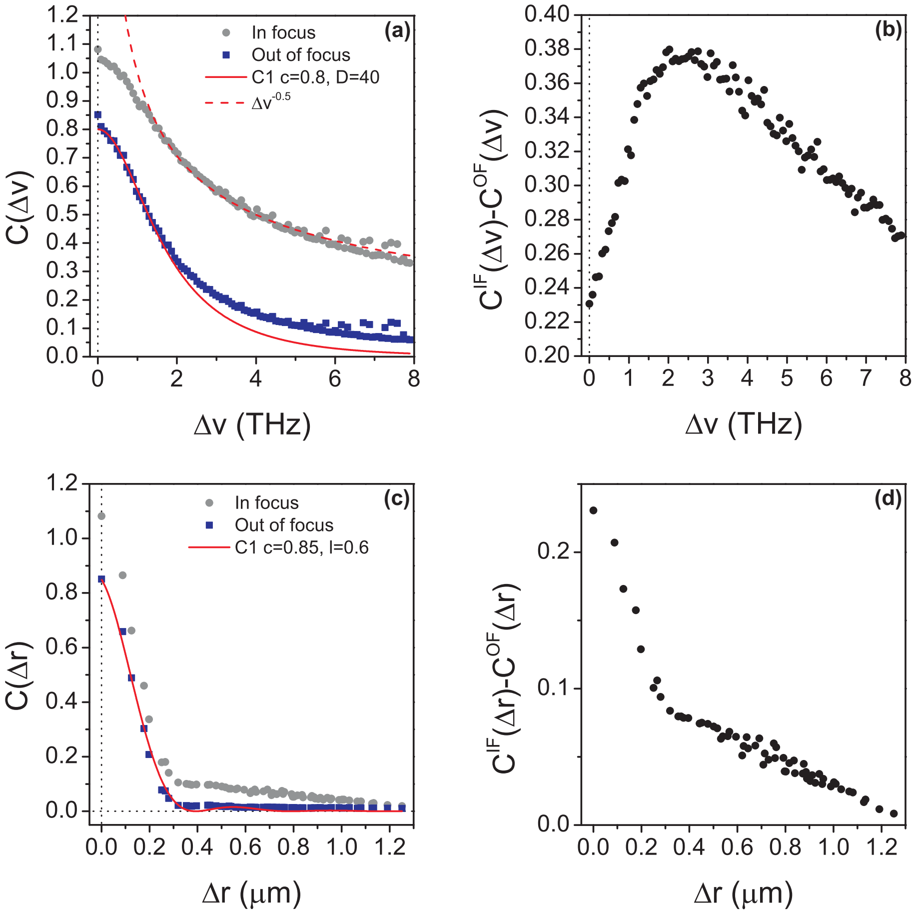

Figure 4.6: (a,c) $C(\Delta\nu)$ and $C(\Delta r)$ obtained using tunable diode laser for sample 3. (b,d) Difference between in and out of focus spectral and spatial correlations C^{IF} and C^{OF}.

Both the spectral and spatial C^{OF} can be reasonably well fitted by $C^{(1)}$ behavior, obtaining values of $l = 0.6$ μm and $D = 40\text{m}^2\text{s}^{-1}$. These are reasonable considering the increase in wavelength and are consistent with previous measurements on such nanowire mats [61]. Consequently at a wavelength of 780 nm the nanowire mat is not as strongly scattering as at 633 nm, as the key indicator of photonic strength $k_n l \approx 10$ is roughly a factor of 2.5 higher. However, this value is still low compared to other scattering mediums such as the ZnO layers studied in Chapter 3. The extrapolation length used in fitting the spectral correlation was $z_e = 1$ μm, calculated from Equation 1.7 assuming an effective refractive index $n_{eff} \approx 2$ for the nanowire mat. The difference between the contrasts used in the $C^{(1)}$ fits is due to all of the uncorrelated noise in the spectral correlation accumulating in the first data point. As a result, the higher value of $c = 0.85$ used to fit the spatial $C^{(1)}$ conceals some mesoscopic fluctuations and the value found for the diffusion constant is likely to be an overestimation.

The y intercept value of $C^{IF}(\Delta\nu)/C^{OF}(\Delta\nu)$ gives $Var[S_{ab}] = 1.29$. This gives a value of $g = 4.5$, close to that obtained using the HeNe. In order to isolate the long range contribution, the difference between C^{IF} and C^{OF} is taken for both the spectral and spatial correlations in Figure 4.6 (b) and (c) respectively. Surprising behavior is found for the spectral correlation, which exhibits a maximum in $C^{IF}(\Delta\nu) - C^{OF}(\Delta\nu)$ around $\Delta\nu = 2.5$ THz. This behavior is not replicated in the difference between the spatial correlations, although a clear slowing of the decay of $C^{IF}(\Delta r) - C^{OF}(\Delta r)$ is seen around $\Delta r = 0.3$ μm.

The difference between in and out of focus spectral correlations may be explained by different initial decay rates for the $C^{(2)}$ depending on the illumination size, as for small $\Delta\nu$ and beam waist $w < L$ a reduction in the beam waist is expected to flatten the top of the $C^{(2)}(\Delta\nu)$ correlation [51], giving an initial slower decay for the in focus illumination. However, this result may also be simply an experimental artifact, and further investigation is required. For a plane wave ($w >> L$), the expected $C^{(2)}(\Delta\nu)$ is given by Equation 4.8 in the absence of internal reflections [41]:

$$C^{(2)}(\Delta\nu) = \frac{4}{g}(\frac{L_\nu}{\sqrt{2}L})\frac{sinh[\sqrt{2}L/L_\nu] - sin[\sqrt{2}L/L_\nu]}{cosh[\sqrt{2}L/L_\nu] - cos[\sqrt{2}L/L_\nu]}. \tag{4.8}$$

For large $\Delta\nu$, it is expected that $C^{(2)}(\Delta\nu) \propto \Delta\nu^{-1/2}$ [51]. It can be seen in Figure 4.6(a) that this reasonably describes the decay of the in focus correlation. One interesting question is the effect of internal reflections upon the $C^{(2)}$ correlation, as the nanowire mats have a significantly higher refractive index than the layers of TiO_2 or ZnO in which such effects are more commonly investigated. The importance of internal reflections can be assessed by comparing the extrapolation length z_e with the spectral coherence length $L_\nu = \sqrt{D/2\pi\Delta\nu}$.

The extrapolation length is estimated as $z_e \approx 1\mu m$ from Equation 4.6, while using $D = 40$ $\mathrm{m^2s^{-1}}$ obtained from the $C^1(\Delta\nu)$ fit results in $L_\nu \approx 2.5/\sqrt{\Delta\nu}$. It can be seen that the two estimates are comparable, with $z_e > L_\nu$ for $\Delta\nu > 6.3$ THz, so it can be argued that the effect of internal reflections should be strong. Conflicting theoretical findings for the frequency dependence of $C^{(2)}$ in the presence of internal reflections exist in the literature. For $z_e > L_\nu$ behaviors $\Delta\nu^{-1/2}$ [80], $\Delta\nu^{-1}$ [81] and $\Delta\nu^{-3/2}$ [82] have been predicted. The experimental correlation supports the proposed $\Delta\nu^{-1/2}$ behavior reasonably well, although the frequency scan range is limited to relatively low values of $\Delta\nu$.

It should be stressed that this is a complex topic with many subtleties, and while the long range frequency dependence appears unchanged in the nanowire sample, it is likely that other effects due to internal reflections are present. These include a reduction in amplitude and a 'flattening' of the short range behaviour [80]. Through a combination of internal reflections and non plane wave incidence, it is difficult to fully fit the experimental data with a combination of a spectral $C^{(1)}$ and $C^{(2)}$.

4.3 Total transmission correlations

It is also of interest to investigate correlations in the total transmission of the nanowire mats. Summing over the transmitted speckle would be expected to result in $C^{(2)}$ correlations for single channel illumination, whereas for a few incident channels the correlation should be in between a $C^{(2)}$ and $C^{(3)}$, as proposed for the transmission statistics in Chapter 3. Total transmission correlations should also provide important evidence about any contribution of sample variations to the measured spatial correlations.

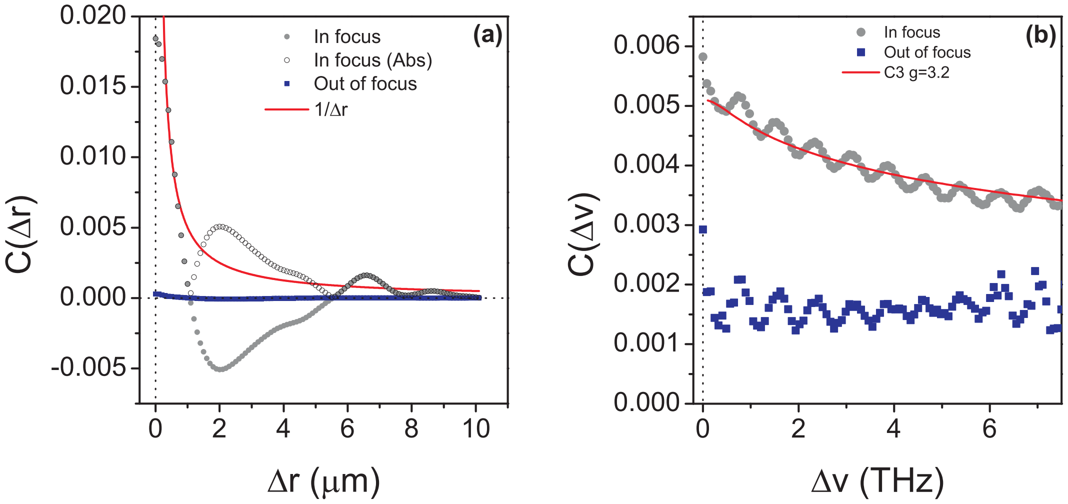

Figure 4.7: (a) Spatial correlation of the total transmission through the 5 cycle nanowire sample in and out of focus, obtained using a HeNe. (b) Spectral correlation of the total transmission through the same sample, obtained using a tunable diode laser with a center wavelength at 780 nm.

Figure 4.7(a) shows the spatial correlation of the total transmission in and out of focus taken using the HeNe with sample displacements of 100 nm over a 600 μm range. As expected, the in focus correlation initially decays to zero quickly over 1 μm, which is the size of the illuminating beam. Interestingly, the experimental correlation then goes negative, indicating that it is statistically more likely for a sample position with high transmission to be followed by one with lower transmission (and vice versa). This is not consistent with correlations that may be caused by sample variation as these would be expected to take place over larger length scales and such an anti-correlation would not be seen. It can be seen that the overall behaviour of the absolute value of the in focus correlation decays as $1/\Delta r$. The out of focus correlation has a much lower magnitude, and since the beam waist is large no oscillations are seen.

The spectral correlation of the total transmission is given in Figure 4.7(b) from the same data set used to find the spectral correlation of the transmitted speckle. The oscillations seen in the correlation are likely to be an experimental artifact from the external cavity diode laser used. The magnitude of the in focus correlation is 0.0054, which if the relation for conductance fluctuations of $Var[S] = 2/15g^2$ is used returns a value of $g = 6.2$, slightly higher than that found from the speckle correlation and likely within the error of the measurement. This supports the interpretation that due to the illumination not being single channel, the total transmission is a quantity closer to the normalised conductance S rather than the single channel transmission S_a. The in focus data can be fitted by a $C^{(3)}$ form derived by van Rossum et al. in ref. [47] with an extrapolation length of $z_e = 0.9$ μm and a beam waist of $1\mu m$, returning a value of $g = 5.0$. However, it can be seen that the out of focus correlation is essentially flat, likely indicating the noise floor of the experiment. As a consequence, the magnitude of the out of focus correlation should be subtracted from that of the in focus, which returns $g = 6.2$. Although the measured total transmission correlation appears to be close to the expectation for the effective optical conductance, as it cannot be argued that all ingoing channels are summed over it cannot be defined as the true conductance.

4.4 Conclusions

The correlations in the light transmitted through strongly scattering nanowire mats was investigated, and found to exhibit long range spatial and spectral correlations inconsistent with the classical diffusive description of light transport. These correlations are attributed to mesoscopic interference effects. As expected, the relative magnitude of the correlations in and out of focus support the finding of Chapter 3 that the transport through such mats is governed by only a few independent transmission channels. The long range correlations decay as expected for the mesoscopic $C^{(2)}$ correlation which represents the correlations due to single light path crossing events. Due to the complex dependence of $C^{(2)}(\Delta\nu)$ on the beam waist and internal reflections, it was not possible to fit the full $C^{(2)}$ behaviour. In particular, internal reflections are expected to be important for the nanowires which have a higher refractive index than other materials commonly studied. It was found that the long range decay of the spectral correlation was proportional to $\nu^{-1/2}$, supporting the finding of ref. [80] that while internal reflections do alter the shape of the correlation, the long range behavior is unchanged.

Examining the spectral correlation of the total transmission, a correlation that could be fitted by $C^{(3)}$ like behavior was found. This supports the suggestion made in Chapter 3 that as the experimental illumination is not single channel, summing over the transmitted light returns a quantity between the single channel total transmission and the optical analogue of conductance. The total transmission correlations also provide important evidence that the fluctuations seen in transmission are due to mesoscopic effects rather than sample variation, in particular the anti-correlation seen spatial total transmission correlation is inconsistent with sample variation.

The transmission was also examined for the effects of a recently proposed non-universal $C^{(0)}$ correlation arising from fluctuations in the LDOS near the source. A small difference was found in the spatial correlation depending on whether the source or detector was displaced, however its value was far below the theoretically predicted value. An explanation for this could again be that the illumination is not a point source, leading to the averaging out of LDOS fluctuations expected between different sample realisations. In conclusion, while $C^{(2)}$ and $C^{(3)}$ type correlations have been observed previously for

3D photonic media, due to the low g of the nanowire mats these correlations are the strongest reported. It is exciting to speculate that the demonstration of such strong correlations may open the way to the harnessing of mesoscopic effects as an additional tool for the many applications of disordered photonics discussed previously in Chapter 1.

Chapter 5

Wavefront shaping

In this chapter, the use of wavefront shaping techniques to focus light through disordered nanowire samples is investigated. In order to shape the incident wavefront, a modified commercial hand held projector was used which is attractive for its accessibility and low cost. It is demonstrated that a sharp focus can be formed despite the low number of transmission channels found through such samples in Chapters 3 and 4. Some of the factors influencing the setup of a wavefront shaping experiment are explored. The field of wavefront shaping is a rapidly expanding one and this chapter follows the pioneering works of others in the field. The work presented here enables the experiments presented in Chapter 6 on obtaining ultrafast control over a shaped wavefront.

5.1 Introduction

As discussed in the Chapter 4, the speckle pattern transmitted through random media contains correlations which contain a surprising amount of information about the source, even when mesoscopic correlations are removed from consideration. A closely related information preserving property of random media is that the multiple elastic scattering is in general a deterministic process. As a result, the principle of time reversal symmetry should hold- if the wavefront scattered from a random medium can be recorded perfectly then sent back, the source should be recreated. This holds regardless of the specifics of the scattering medium. Successful time reversal experiments have indeed been performed to recreate a sharp focus after propagation through a random scattering medium for acoustic [11, 12], electromagnetic [13, 14] and water waves [15]. This is of great interest as it shows it is possible to focus through diffusive media, which is an issue of importance for the use of lasers in medical imaging and treatment. However, for applications the time reversal approach has clear practical limitations due to the difficulty of recording and playing back an optical wavefront and the requirement for a source to be placed at the desired focal point.

An alternative approach is to create the correct incident wavefront to create a focus through a random medium by trail and error. It has been shown that by using a spatial light modulator (SLM) to manipulate the incident wavefront to a medium to create so called 'perfect focusing' [16, 17]. In this pioneering work, Mosk et al. implemented an iterative approach in which the effect of small changes to the incident wavefront on the transmitted light was monitored in order to find the optimum input to create a single bright focus. This approach amounts to altering the relative phase between transmission channels in order to create a condition of constructive interference at a selected point. Impressively, this method can beat the diffraction limit of traditional optics due to the larger number of degrees of freedom available to a diffusive medium to form a focus [83, 22].

It has subsequently been shown that by selectively coupling to open transmission channels, the overall transmission can be enhanced [18, 19], and that a large fraction of the transmission matrix of a random medium can be measured [20]. In principle, knowledge of the transmission matrix of a diffusive medium such as a simple layer of white paint can be used to turn it into a versatile reconfigurable optical element. As well as the ability to create arbitrary focal points in space, it is also possible to configure the incident wavefront to transmit a narrow frequency range of a broadband light source, creating a reconfigurable spectral filter [84].

The maximum possible intensity enhancement of a speckle relative to the background is given by the scenario of perfect constructive interference of all transmission channels at that point.'In the ideal case in which the transmission is dominated by open channels with transmission unity, the limit to the enhancement is simply given by the number of open transmission channels. In this chapter, wavefront shaping techniques are used to focus through the nanowire mats shown to have transmission characterised by only a few transmission channels. This is in contrast to typical optical experiments, and it is of interest to see the enhancements possible through these samples. Experiments with microwaves have demonstrated experimentally the dependence of enhancement upon number of transmission channels [85].

5.1.1 Spatial light modulators

It is possible to manipulate both the phase and amplitude of an incident wavefront using a spatial light modulator (SLM). These devices impart controllable spatial patterns onto reflected or transmitted light, and are essentially specialised display devices. SLMs fall into two broad categories: those based on liquid crystal (LC) technology and those based on digital micro-mirror displays (DMD). The easy access to phase modulation using LC SLMs has lead to their use in the majority of the pioneering investigations mentioned above. However, there are some disadvantages associated with using LCs, namely the relatively slow refresh rate of LC displays, low damage thresholds and high cost. DMDs consisting of arrays of micro-mirrors that can be individually programmed to send light either to a target or a beam dump typically outperform LCs on these criteria, at the cost of losing direct access to phase control. The high refresh rates of DMD devices is of particular interest as it enables focusing through rapidly changing turbid media [86], which is representative of the reality of applications in biological systems.

In this thesis a DMD based SLM was used. For first investigations a commercially available micro projector (Acer C20 Pico Projector) was modified to allow direct optical access to the DMD chip Figure 5.1. Patterns could be written to the DMD by using it as a second screen for a PC. While this is a rudimentary technique, limiting the refresh rate of the DMD to 60 Hz, it is nonetheless effective and considerably less expensive than purchasing a dedicated research SLM (also shown in Figure 5.1 and used in Chapter 6). Such modified projectors have a wide range of applications outside of controlling light transmission through random media, including the fabrication of micro-structures [87].

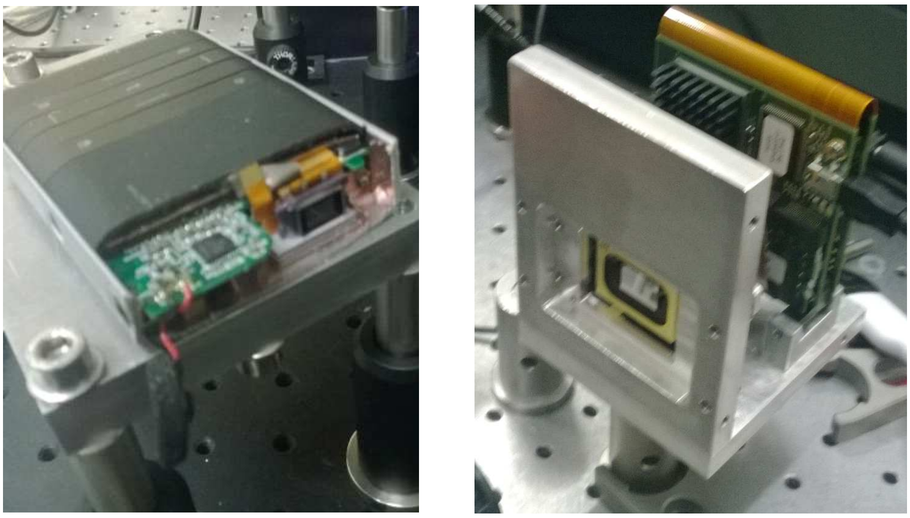

Figure 5.1: Left: Image of commercial hand-held projector modified to allow optical access to the DMD chip. Right: ViaLUX research DMD used for wavefront shaping experiments in Chapter 6.

5.1.2 Binary amplitude modulation

The general principle of all wavefront shaping schemes is similar: changes are made to the incident wavefront while the outgoing wavefront is monitored in order to find the optimum pattern for the desired result. The exact details of each scheme depends on the use of phase or amplitude modulation, the number of polarisation channels considered and the detection method. Furthermore, there are several possible choices of algorithms including controlling either single sequential elements or random subsections of the SLM [18], generating a complete basis set of random patterns to measure the transmission matrix [86] and genetic evolution of a series of random patterns in order to find the optimum [88]. Each has advantages depending on the specific situation. One scheme which is particularly attractive for its simplicity is that of binary amplitude modulation, as demonstrated by Akbulut et al [89]. This is the approach adopted in this thesis.

In binary amplitude modulation, the DMD surface is divided into a number of segments. All segments are initially set to send light to the sample, and are then sequentially turned off and on while the intensity on a selected area of interest (AOI) on a camera is monitored. The state resulting in the highest intensity is retained and the process is repeated for the next segment, resulting in a pattern that gives a bright focus in the AOI. Unlike phase modulation schemes in which the phases of transmission channels are aligned, this amounts to turning off transmission channels with a destructive contribution to the intensity of the selected speckle. The principle of this scheme is shown in Figure 5.2.

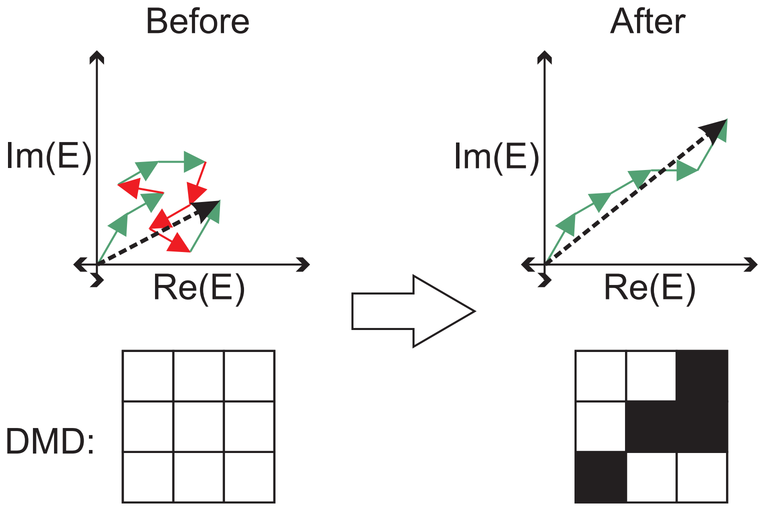

Figure 5.2: Illustration of the binary amplitude modulation wavefront shaping scheme.

As out of phase transmission channels are turned off, this approach suffers a penalty in performance compared to phase modulation schemes. If the highest enhancement attainable is the number of transmission channels N, then assuming an even distribution of phases and a large number of channels, the highest enhancement possible using binary amplitude modulation is approximately $N/4$. This is arrived at by expecting that half of the transmission channels will be turned off, and the average phase difference between the channels left on will be $\pi/4$. Of course this is an ideal case, and in reality it is expected that the details of each optimisation will have a dependence on the initial makeup of the speckle selected.

An important experimental consideration is noise, as this can mask the effect of turning segments on and off. Consequently while it would be expected that increasing the number of segments controlled on the DMD would increase the quality of an optimisation towards the ideal case, there is a limit at which the signal associated with a single segment falls below the noise floor. It has been shown that performing a pre-optimisation with larger segments than the final optimisation increases the signal to noise ratio in the AOI resulting in better enhancements [90]. Another issue of great importance is stability, as displacements of the beam or sample over distances greater than the typical speckle correlation length will result in the formation of a completely new speckle requiring a different pattern of illumination to create a sharp focus.

5.2 Experimental setup

The experimental setup used for focusing through the nanowire samples is shown in Figure 5.3.

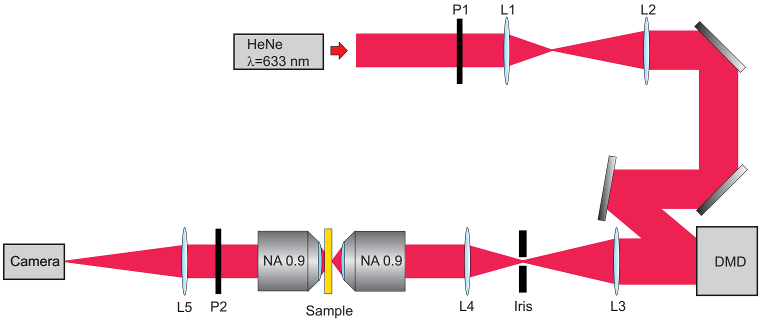

Figure 5.3: Diagram of wavefront shaping setup.

A Helium Neon (HeNe) laser was used for the initial investigations. The beam was expanded by lenses L1 and L2 to a size larger than the DMD chip to obtain a reasonably even illumination of its surface. The DMD was then imaged onto the pupil of the microscope objective focusing the light onto the sample by lenses L3 and L4. A matching pair of objectives with NA of 0.9 (Nikon CFI60 LU Plan BD) were used to image and collect light from the sample. A 200 mm lens (L5) then images the transmitted speckle onto a camera (AVT Stingray F-033). Polarisers P1 and P2 are used to select only 1 ingoing and outgoing polarisation channel, in order to improve the speckle contrast. Controlling both incident polarisations separately would allow higher enhancements, however, this would increase the complexity of the setup considerably and was not adopted for these first experiments.

It should be noted that although the DMD is divided into spatial segments, these are Fourier transformed into angular channels at the sample surface by the microscope objective. Consequently, as these channels are turned off the size of the illumination on the sample will increase as the number of angular channels available to create a focus decreases in a manner analogous to reducing the NA of the objective. Unlike previous experiments in Chapters 2-4 with these nanowires, the glass cover slip side of the sample was illuminated and the speckle was imaged through the GaP substrate. This was in order to reduce the effect of aberrations in the GaP slab on the optimisation. The sample used is the 6 μm thick nanowire sample 3 investigated in Chapters 3 and 4.

For the optimisations, an AOI is selected on the camera that is comparable in size to the typical individual speckles. While individual segments on the DMD are turned on and off, the intensity in the AOI normalised to the total transmission is monitored and for each segment the state giving the highest value is retained. Normalising to the total transmission has two benefits: it negates the effect of fluctuations in the laser intensity, and accounts for the overall reduction in transmission that results from turning off segments that do not contribute constructively to the intensity in the AOI. Without this normalisation, changes which increase the contrast between speckle and background but reduce the overall total transmission would not be accepted, resulting in a largely ineffective optimisation. The choice of segment size has a significant impact upon the optimisation process, and is investigated further later in this chapter. The imaging objective is displaced a few microns out of focus for all optimisations in order to optimised on the far field in which the transmission modes should be fully mixed.

5.3 Focusing through nanowire samples

An example of an optimisation performed using binary amplitude modulation of the incident wavefront is shown in Figure 5.4.

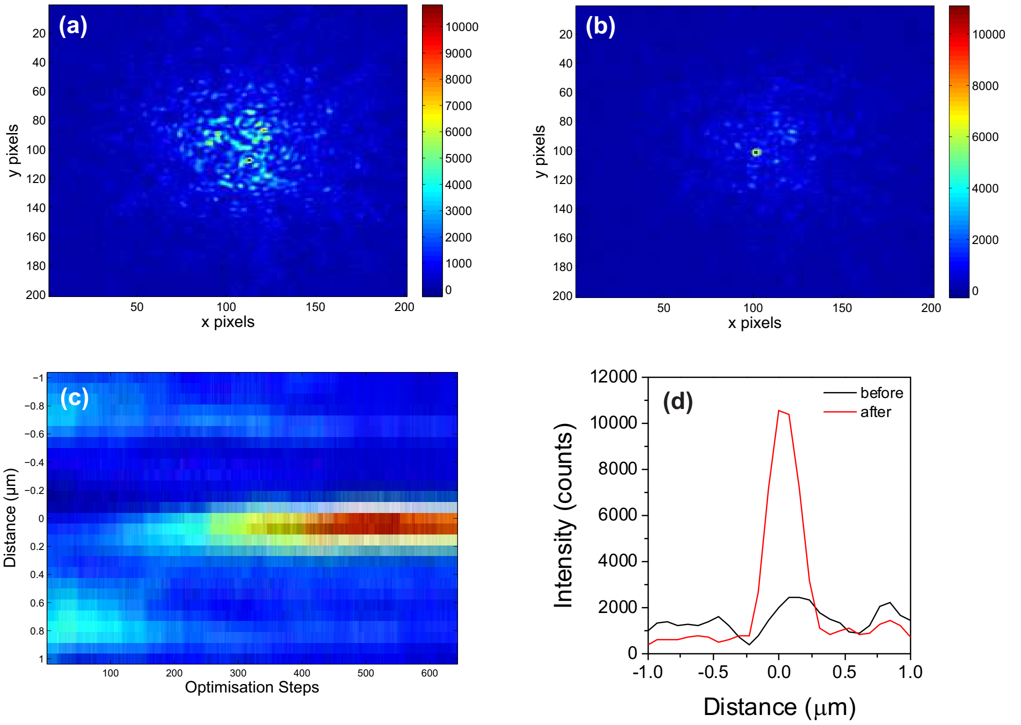

Figure 5.4: Images before (a) and after (b) optimisation using the binary amplitude modulation scheme. (c) Plot of cross-section through the AOI as a function of optimisation step. (d) Comparison of cross sections of the initial and final image.

From the images of the transmitted light are shown before and after the optimisation process in Figure 5.4 (a) and (b), it is clear that the wavefront shaping algorithm has created a single intense focus as desired. The progress of the optimisation can be visualised by the cross-sections through the AOI for each optimisation step shown in Figure 5.4 (c). From the cross-section of the final optimised spot in Figure 5.4 (d) it can be seen that a ratio of the peak to the background of approximately 15 is achieved. To obtain this result, an AOI with a radius of 2 pixels (0.2 μm on the camera) was used, with the DMD divided into 640 segments.

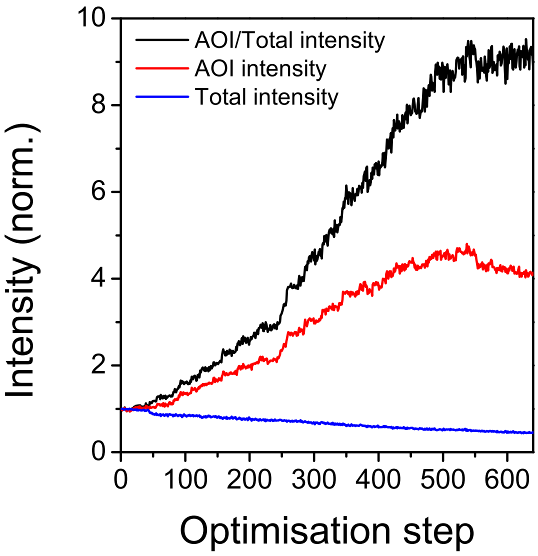

Figure 5.5: Plot of the AOI, total and AOI normalised to total intensity with optimisation step for the optimisation shown in Figure 5.4

In Figure 5.5 the evolution of AOI and total intensity with optimisation step is shown. It can be seen that there is a significant increase in intensity in the AOI over the optimisation and that the total transmission reduces by approximately a factor of 3. This means that the reduction in the total transmission plays an important role. The expectation was that approximately half of the segments on the DMD would be turned off, meaning the contribution seen from the reduction in total intensity is higher by a factor of 1.5 than this prediction. This result is representative of the large number of optimisations carried out using this setup. The reason for this larger decrease in total intensity is not known, although it is possible to speculate about about turning off transmission modes which do not fully extend to the specific point the optimisation is carried out at.

5.3.1 Effect of the number of segments

In order to assess the effect of changing the number of segments, optimisations were carried out sequentially on the same sample position with different segment sizes. The change in the intensity in the AOI normalised to the total intensity for this experiment is shown in Figure 5.6 (a), while Figure 5.6 (b) shows the final value achieved as a function of number of segments.

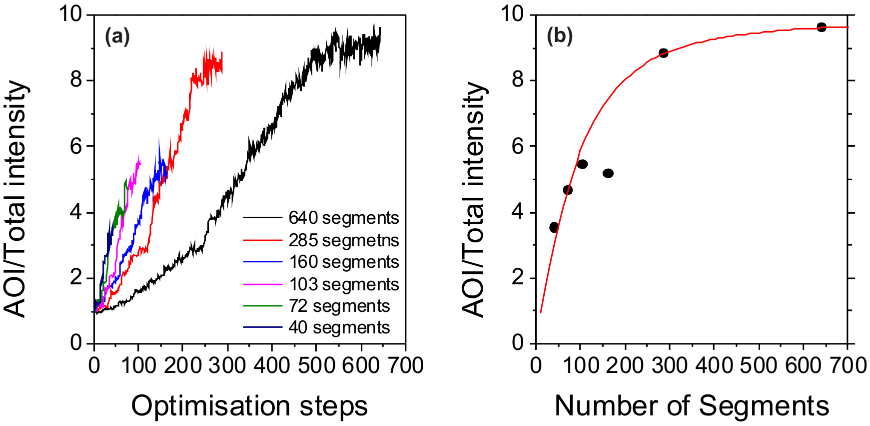

Figure 5.6: (a) Plot of the relative change in intensity in the AOI with optimisation steps for different numbers of segments. (b) Final enhancement achieved as a function of number of segments.

As expected, increasing the number of segments improves the quality of the optimisation. The exception is the optimisation carried out with 160 segments, which shows a decrease in enhancement towards the end of the scan indicating either a small shift in alignment or a bad choice by the algorithm. While the optimisation process is in general reliable, such events occur from time to time resulting in a reduced enhancement. It is clear that as the number of segments is increased that the the final enhancement achieved appears to converge towards a limiting value. This is because the signal associated with each segment drops as the number of segments is increased due to the illuminated area of the DMD being held constant. Consequently for a larger number of segments noise has a greater influence, reducing the efficiency of the algorithm.

Increasing the number of segments also increases the time taken for the optimisation to complete. This time ranged between around a minute for the lowest number of segments to approximately 10 minutes for the highest. This introduces another experimental factor in the stability of the setup. Even small relative changes between the pattern on the DMD and the sample reduce the optimisation quality as the pattern formed on the DMD is specific to the local configuration of the sample. Thus there is an advantage to be gained by performing the optimisation quickly, and conversely if the time for an optimisation to complete is greater than the decorrelation time of the system the formation of a focus by shaping the incident wavefront is not possible. A drawback to the use of the modified DMD controlled as a second screen, as presented here, is that its speed of operation is a limited to typical display refresh rates of 60 Hz. In contrast, dedicated research SLMs which have been shown to be able to perform optimisations on the timescale of milliseconds, important for use in imaging through fast changing biological systems [86].

5.3.2 Assessment of optimisation

An enhancement of 15 between the peak and background is sufficient to form a single bright spot, however, it is low compared to typical values of enhancements reported in literature of between in the range of 100-1000. In part, this is due to the choice of scheme, with phase control allowing much larger enhancements. Additionally, Akbulut et al. found that the use of a modified DMD as used here has a performance penalty compared to the implementation of the same binary amplitude modulation scheme using a LC SLM [89], attributed to details of the commercial projector used. As discussed previously, a low number of transmission channels is also expected to limit the optimisation quality. While the nanowire sample used was shown to only have a few transmission channels for a tightly focused illumination, the loss of angular information to create this focus by switching off incident channels is expected to increase the size of the illumination. Indeed, it is possible that the optimisation process works to increase the size of the illumination allowing access to additional transmission channels contributing to the intensity in the AOI. Consequently, no conclusion can be reached about the effect of a low number of transmission channels on the optimisation from this experiment.

5.4 Summary

A DMD was used to create a focus through the nanowire mats shown in Chapters 3 and 4 to have a transmission characterised by only a few transmission channels for a tightly focused illumination. Modest optimisations were found, with several possible factors including the use of a modified commercial hand-held projector and the low number of transmission channels. Further investigations are required in order to separate these factors. Ultimately, the work presented in this chapter does not give any new information about the nanowire mats used, however, the creation of a successful focus through them opens the way for performing experiments on this optimised spot in the following chapter.

Chapter 6

Ultrafast control of shaped wavefronts

As shown in Chapter 5, it is possible to create a bright focus through disordered nanowire mats by shaping the incident wavefront using a DMD based SLM. In addition to the impressive control over the transmitted light offered by wavefront shaping, it is interesting to consider how the intrinsic nonlinearity of the nanowire samples used could be used to gain an additional degree of control. In this chapter, ultrafast laser excitation is used to achieve modulations of up to $63 \pm 2\%$ of a shaped wavefront, and it is shown that the effect of dephasing can be reversed to rephase an optimised wavefront, enhancing the peak to background ratio by $20 \pm 2\%$ [3]. The principle of a reconfigurable photonic switch demonstrated here may be of interest for application in telecommunications.

6.1 Dephasing of a shaped wavefront

The basic concept of the proposed experiment is illustrated in Figure 6.1. First, a single bright focus is created at a selected point on the outgoing face of the sample using the wavefront shaping techniques detailed in Chapter 5. As a result the phases of separate transmission channels are in phase at this point. The sample is then excited in the form of an ultrafast optical pulse, which induces a series of random phase shifts between transmission channels, destroying the constructive interference creating the focus. Given the high contrast between the optimised speckle and the average background, such an approach has the potential to achieve large modulations of light sent to an arbitrarily determined position.

In this proof of principle experiment, a pump-probe scheme is used in which probe light at 633 nm is shaped to create the shaped wavefront and pump light at 400 nm is used to excite the nanowire sample. The pump light excites electrons above the indirect

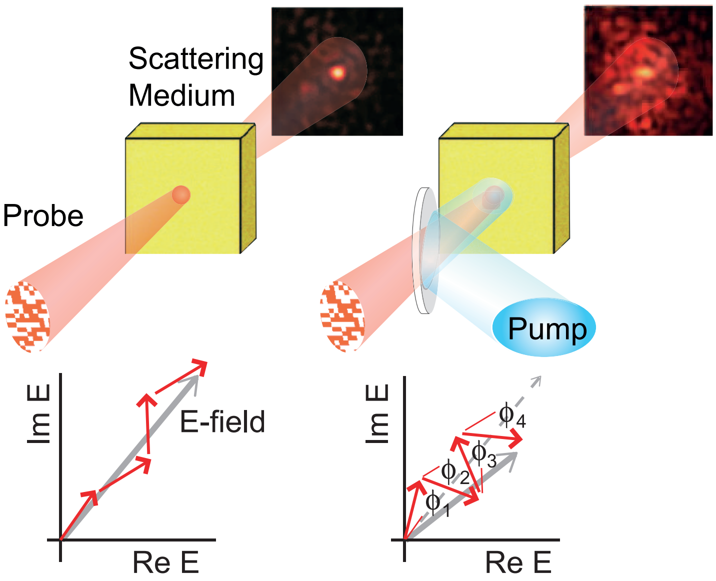

Figure 6.1: Illustration of the proposed reconfigurable photonic switch. Top: A sharp focus is created by shaping the incident wavefront, and is destroyed by excitation by an ultrafast optical pulse. Bottom: Sketch of phasor diagram contributing to the optimised spot corresponding to the cases shown above.

electronic bandgap of GaP (which is at 550 nm). This results in induced absorption of the probe by the pump, as these electrons are available to absorb the probe light. Previous work by Abb et al. investigating the dephasing of frequency speckle through similar samples identified two possible dephasing mechanisms: an induced change in refractive index and a small change in scatterer size or position [91]. Although such effects are small, the large average dwell time of light within the nanowires means the resulting phase shifts can be relatively large.

Similar experiments have demonstrated that dephasing can break time reversal symmetry in samples of porous GaP [92]. As the nanowire samples used have been shown in Chapters 3 and 4 to exhibit strong mesoscopic interference effects [2], it is interesting to consider whether these can be suppressed by dephasing. It is also interesting to consider how the presence of the pump affects the optimisation process itself, and whether an optimised spot which depends on the dephasing induced by the pump can be created. This is similar in principle to the use of a wavefront shaped pump to control the output of a random laser [26], another very exciting active field of research.

6.2 Experimental details

6.2.1 Pump probe setup

Figure 6.2 shows the experimental setup for the pump-probe experiment. The wavefront shaping part of the setup is similar to that used in Chapter 5.

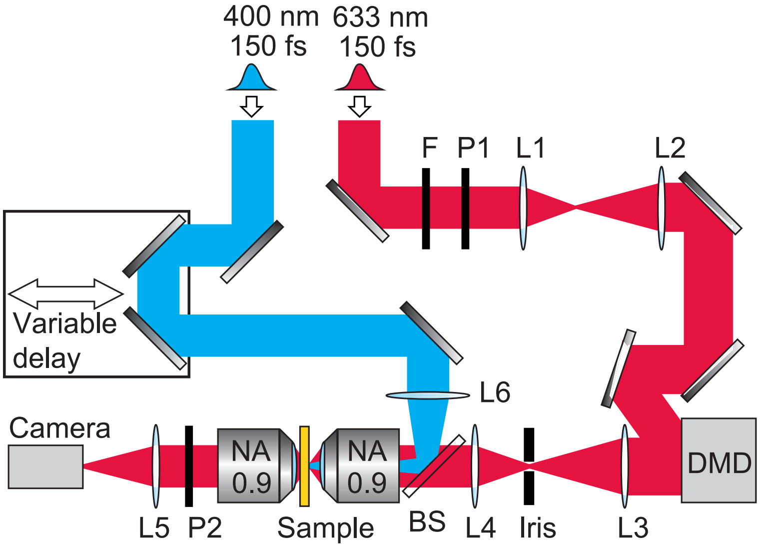

Figure 6.2: Diagram of experimental pump-probe setup used to attain ultrafast control over a shaped wavefront.

Probe light around 633 nm is obtained from the signal output of a regenerative amplifier (Coherent RegA, 250 kHz, 150 ± 10 fs pulse duration) pumped optical parametric amplifier (Coherent OPA 9400), while the pump at 400 nm is obtained from the second harmonic. An interference filter (F) is used to reduce the bandwidth of the probe light to 632.8 ± 1 nm, at the cost of increasing the pulse length (as seen in the following section). Polarisers P1 and P2 are used to select a single ingoing and outgoing polarisation channel. Light is focused onto the sample and collected by a matching pair of microscope objectives (Nikon CF160 LU Plan BD, NA=0.9), and imaged onto a 16 bit monochrome camera (AVT Stingray F-033) by a 500 mm focal length lens (L5). A 250 mm focal length lens (L6) focuses the pump light onto the objective pupil, ensuring that the illumination size of the pump is greater than that of the probe. This is important as it means the effect of the pump is almost uniform for all the input channels accessible by the DMD. In this chapter, a ViaLUX v7000 DMD was used, containing a Texas Instruments DLP discovery chip-set. Compared to the modified projector used in the previous chapter controlled as a second screen, the ViaLUX DMD is completely programmable allowing faster, more controlled operation.

The relative delay between the pump and probe pulses is controlled by a computer controllable mechanised stage that changes the length of the pump path. The maximum effect from the pump is expected when the pump and probe pulses overlap. Defining this zero delay position is important to the experiment as it gives information about the time dynamics of the effect of the pump, and is addressed in the following section. A computer controlled shutter on the pump path (not shown in the diagram) allows the pump to be blocked and unblocked allowing the relative change induced by the pump to be measured. In order to observe the highest possible effects from the pump, all experiments were carried out using a total pump power of 8 mW incident on the sample. This is approximately 70% of the power for which slow degradation of the sample was deserved. In comparison, the average power in the probe beam was less than 0.1 mW. The use of higher pump powers did not result in reproducible results. Due to the large illumination size of the pump light, the pump fluence was estimated to be no higher than 15 Jcm^{-2}.

For these experiments the nanowire sample used is the 4.5 μm thick sample 2. While the bandwidth of the probe pulse is narrow (0.75 THz), it is comparable to the characteristic spectral width of speckle transmitted through the nanowire mats [91, 2] and consequently the contrast of the transmitted speckle is an issue. A measure of the spectral width is given by the inverse of the Thouless time $\tau_D = L^2/D$ [41]. As a result, sample 2 results in a better speckle contrast than the 6 μm thick sample 3, and is more suited to this initial investigation as mesoscopic effects are not expected to be as strong.

6.2.2 Calibrating pump probe zero delay

The zero pump probe delay position was found by replacing the nanowire sample with a bare GaP slab and measuring the induced change in the transmission of the probe by the pump as a function of the delay stage position. In order to measure this as accurately as possible the setup shown in Figure 6.2 was modified by replacing the camera with a silicon photodiode and using a chopper and lock-in amplifier. As the 300 μm thick GaP slab absorbs all of the pump light, the signal detected by the lock-in when the pump is modulated by the chopper is purely the effect of the probe upon the pump. This was checked by placing an additional blue filter in front of the photodiode, and no change in the signal was seen. This pump-probe signal is plotted in Figure 6.3 for both the GaP slab and the 4.5 μm thick nanowire sample.

The pump-probe signal is a convolution of the response function of the material and the probe pulse, with the pump pulse determining the resolution possible. In this case, because of the filter reducing the bandwidth of the probe pulse, the pump is much shorter than the probe. The response of the slab can be assumed to be a step function, with no induced absorption when the probe arrives before the pump and a constant value of absorption if the pump arrives before the probe. This is because excited charge carriers in the GaP require a phonon to relax back to the ground state which typically occurs on timescales of 10s to 100s of picoseconds compared to the 150 fs probe pulse. In this

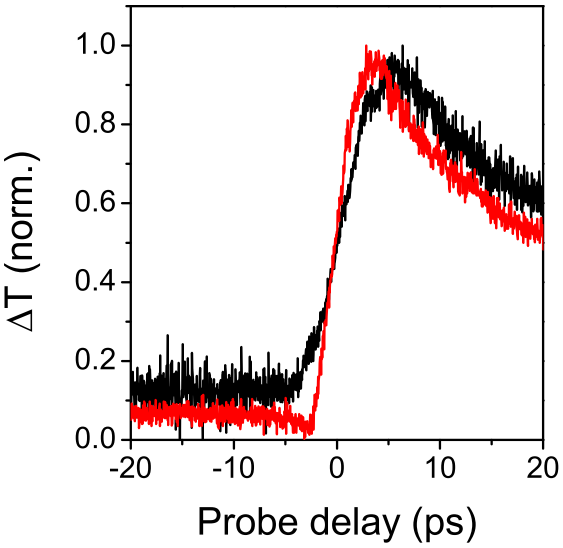

Figure 6.3: Comparison of the pump-probe signal ΔT normalised to the maximum value for the 2 cycle nanowire sample (black line) and a plain GaP slab (red line).

case, with a Gaussian probe pulse, the zero delay position is defined as being halfway up the rising slope of the pump-probe signal ΔT.

In Figure 6.3, the absolute value of ΔT is normalised to a peak signal in order to compare the nanowire mat and the GaP slab. It can be seen that the response of the slab is not a step function, however, the decay of the signal is slow compared to the rising edge meaning the definition of the zero remains valid. The effect of reducing the bandwidth of the probe can be clearly seen, as the probe pulse duration extends to approximately 5 ps. The response function of the nanowire sample is different to that of the GaP slab due to the strong light trapping effect of the wires. In principle it is possible to extract information about the light path distribution through this technique, however, as in this case the dwell time is less than the probe pulse duration it is difficult to draw any concrete conclusions.

6.2.3 Dephasing of plain speckle

Before investigating the switching of a shaped wavefront was investigated, the effect of the pump on an unshaped plain speckle pattern was examined. The speckle transmitted through the nanowires was captured by the camera with pump blocked and unblocked for different relative delays between the probe and pump. The relative change in the total transmission $\Delta T/T$ was calculated by taking the difference of the total transmission with pump blocked and unblocked, normalised to the image with pump blocked, and captures the effect of induced absorption Figure 6.3. The correlation between these images reveals any effect of dephasing, as the effect of absorption alone is expected to only reduce the average transmitted intensity, not change the transmitted speckle pattern. The correlation between images with and without pump $I(x,y)_P$ and $I(x,y)_{NP}$ was defined as follows:

$$Corr[I(x,y)_{NP}, I(x,y)_P] = \frac{\sum_{x,y}(I(x,y)_{NP} - <I(x,y)_{NP}>)(I(x,y)_P - <I(x,y)_P>)}{\sqrt{\sum_{x,y}(I(x,y)_{NP} - <I(x,y)_{NP}>)^2 \sum_{x,y}(I(x,y)_P - <I(x,y)_P>)^2}}. \tag{6.1}$$

The speckle correlation and $\Delta T/T$ are plotted as a function of pump-probe delay in Figure 6.4.

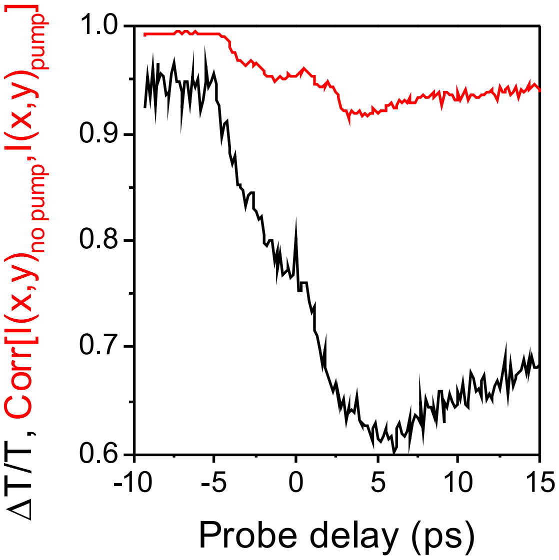

Figure 6.4: Plot of relative change in transmission $\Delta T/T$ (black line) and speckle correlation function (red line) for an unshaped wavefront transmitted through the 2 cycle nanowire sample.

The main effect induced by the pump is the absorption, which a decrease in around 40% of the total transmission observed, with a maximum effect around 5 ps. The extension of the effect into negative delays, in which the probe arrives before the pump, is a result of both the long dwell time of the probe light within the nanowires and the duration of the probe pulse itself. There is also a clear reduction in the correlation of the speckle with a maximum around 3 ps that has a different behavior to that of the absorption. This is attributable to the dephasing of different light paths by the pump, which results in a change in the spatial speckle distribution rather than the average transmission. Both effects are expected to be significant for the switching of an optimised spot.

6.3 Switching shaped wavefront

The optimised wavefront was created using the binary amplitude modulation technique outlined in Chapter 5. Optimisations were performed using 900 segments on the DMD with the pump beam blocked, with a second optimisation being carried out immediately afterward taking advantage of the increased signal to noise ratio to improve the focus quality. Performing additional optimisations after this was observed not to improve the quality of the focus further. Images of the transmitted speckle were then taken with pump on and off for different delay positions. The details of one of the best results obtained is shown in Figure 6.5.

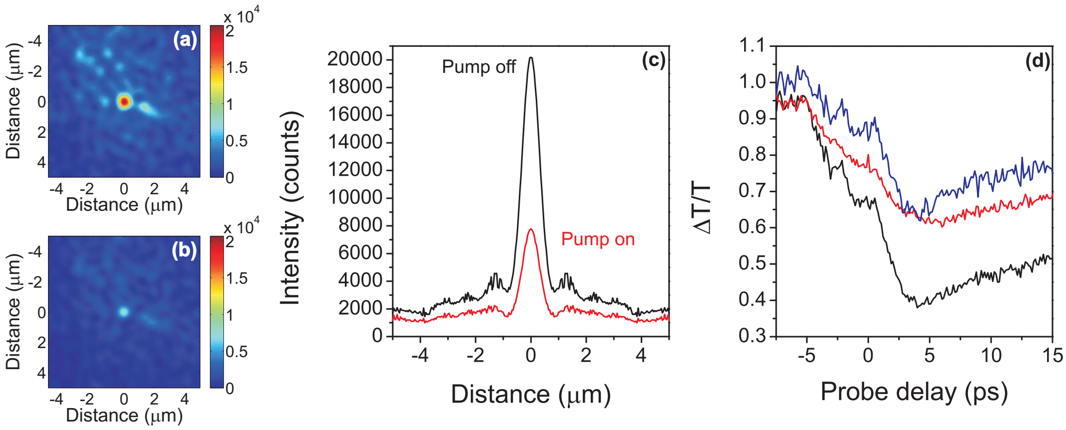

Figure 6.5: Images showing optimised spot with pump off (a) and on (b) with a pump-probe delay of 2 ps. (c) Radially averaged cross-sections of image (a) and (b) (black and red lines respectively). (d) Background $\Delta T/T$ (red line), peak change (black line) and peak to background modulation (blue line) as a function of pump-probe delay.

Figure 6.5(a) and (b) show images of an optimised spot with and without pump respectively with a pump probe delay of 2 ps. It is clear that the pump causes a large reduction in the amplitude of the optimised speckle. This is shown in more detail by the radially averaged cross-sections of these images in Figure 6.5(c), with a change in peak intensity of 63%. This is much larger than the average modulation of the background intensity of around 35%, indicating that dephasing plays an important role.

In order to assess the roles of dephasing and induced absorption further, quantities representative of these two effects should be defined. The relative change $\Delta T/T$ in the background intensity, calculated by excluding an area of 1 μm in diameter around the AOI of the optimisation, is expected to reflect the effect of induced absorption. If this was the only effect, it would be expected that the modulation of the peak intensity would follow that of the background. Consequently, changes to the peak to background ratio are taken to be indicative of the effect of dephasing. These quantities are plotted in Figure 6.5(d) as a function of pump-probe delay. The change in the background has a smooth behavior similar to that seen for the plain speckle with a maximum change around 5 ps. In comparison, the change in the peak to background ratio has more features and peaks earlier than the background. At the delay of 2 ps for which the modulation of 63% is observed, the contribution of absorption and dephasing appears to be equal.

The exact behavior of the change in the peak to background ratio is interesting, as it reflects the path distribution contributing to the optimised spot, and may be considered to be a unique fingerprint of that individual speckle. To investigate this, experiments were carried out on many different sample positions. This also provides an important measure of the typical result obtainable, in contrast to the best result shown in Figure 6.5. Histograms of the distributions of results obtained are shown in Figure 6.6.

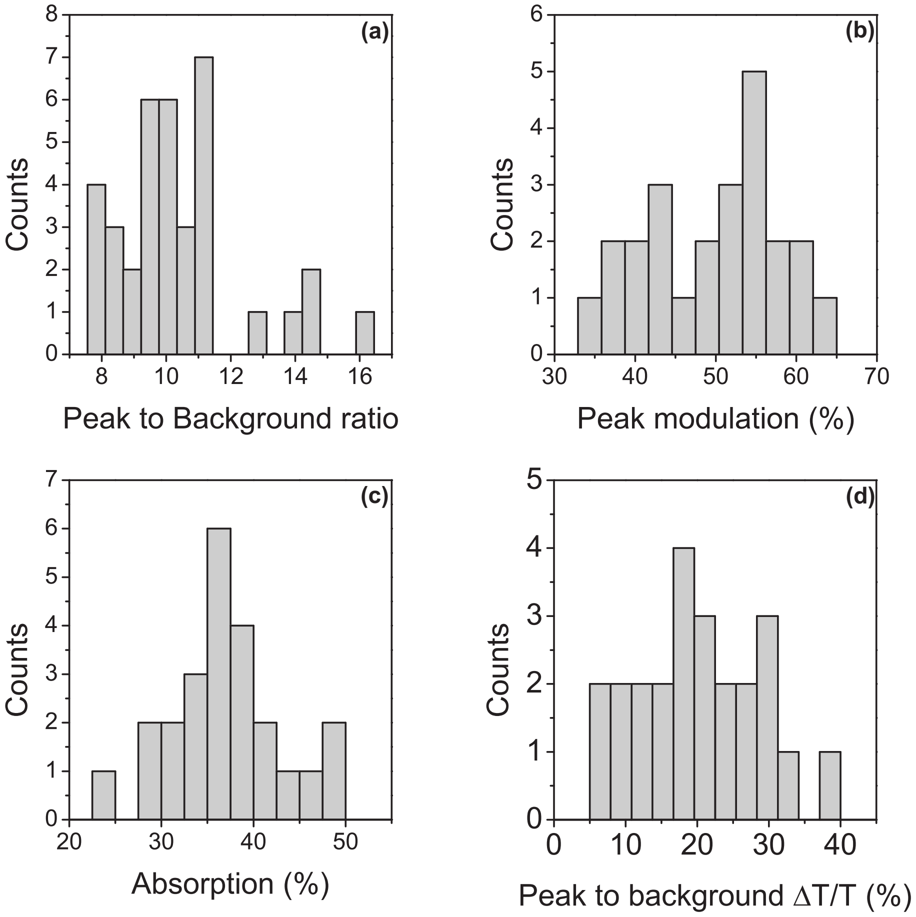

Figure 6.6: Histograms showing the experimental variation found in optimisation quality (a), peak modulation (b), maximum absorption (c) and maximum peak to background $\Delta T/T$.

Over 36 optimisations, there was a large variation in optimisation quality as shown in Figure 6.6(a). The average peak to background ratio obtained was 10.4 ± 0.3. This is worse than typical optimisations with peak to background enhancements of around 20 achieved using a HeNe in Chapter 5. This can be attributed to the higher bandwidth of the probe light decreasing the speckle contrast and the increased noise present in the OPA system, which relies on a series of nonlinear effects and is consequently extremely sensitive to small environmental changes. The few higher enhancements in peak to background ratio correspond to times at which the experimental setup was at its most stable. While the quality of the optimisations achieved was not high, most were sufficient to test the principle of the switching of an optimised spot.

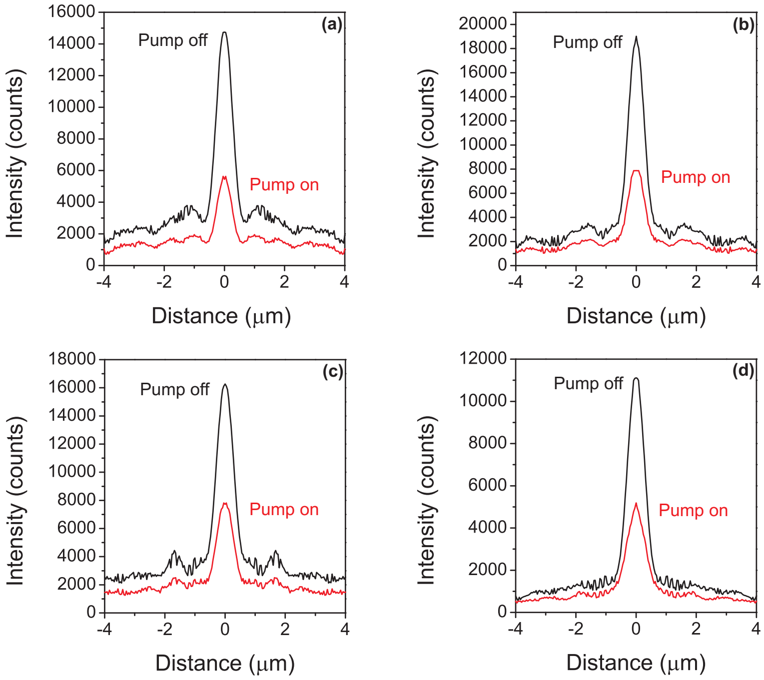

Figure 6.7: (a-d) Radially averaged cross-sections of modulations above 55% attained on four separate sample positions. Black lines and red lines represent the situation with pump blocked and unblocked respectively.

Figure 6.6(b-d) show the distribution of the maximum peak modulation, absorption and peak to background modulation effects observed for 24 separate data sets. The average peak modulation achieved was 50 ± 2% with an average contribution from absorption of 37 ± 1% and dephasing of 20 ± 2%. A significant reason for the variation seen in results is likely to be attributable to the spatial overlap between pump and probe for each data set, which remains a critical experimental factor despite the large size of the pump illumination compared to that of the probe due to the pump illumination not being entirely uniform. Additionally, variations in the peak to background modulations are also expected to depend on the details of the speckle optimised on. Despite the experimental variation apparent from the histograms, high peak modulations of above 55% were reproduced on 4 separate sample positions as shown in Figure 6.7.

The dynamics of the peak modulation, absorption and peak to background modulation as a function of pump delay are shown in Figure 6.8. Similar traits can be seen to Figure 6.5(d). The behavior of the absorption is smooth and relatively consistent, while the modulation of the peak to background ratio shows additional features, and in general peaks before the maximum absorption effect which corresponds with the position of maximum switching of the peak. It can be seen that the behavior of the peak to

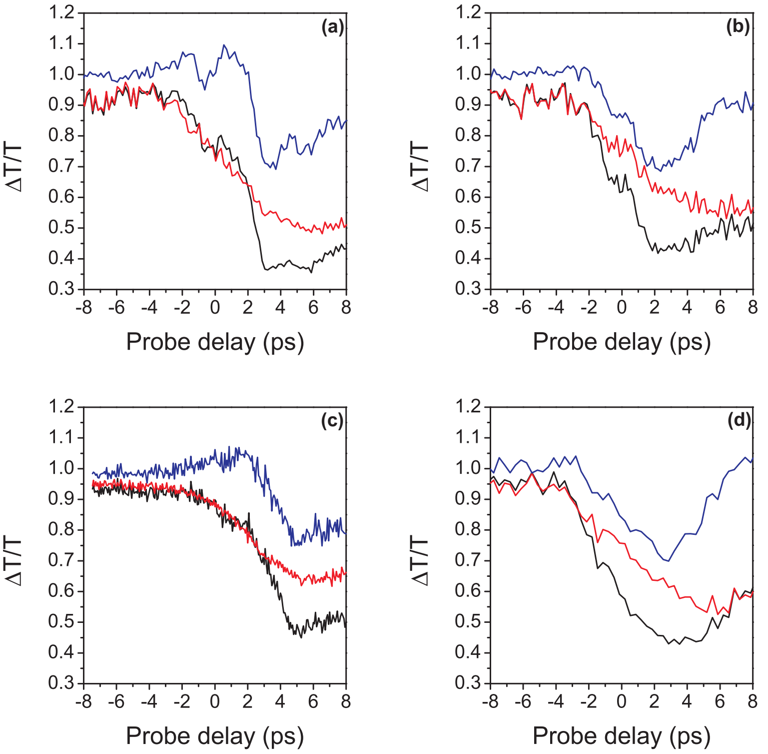

Figure 6.8: (a-d) Plots of $\Delta T/T$ of the background (red lines), peak modulation (black lines) and peak to background $\Delta T/T$ as a function of pump-probe delay at the four sample positions shown in Figure 6.7 (a-d)

background modulation is different between all four sample positions, with the maximum effect for pump probe delays between 2 and 4 ps. This is likely to reflect the individual path distribution contributing to each speckle.

Aside from the peak to background modulation ratio, another quantity that reflects the effect of dephasing is the speckle correlation. The speckle correlation functions corresponding to the data in Figure 6.8 and Figure 6.7 are shown in Figure 6.9. In all cases, the trends seen in the correlation plots resemble closely the features of the plots of the modulations in the peak to background ratio of Figure 6.8. However, the maximum value of the peak to background modulations seen are slightly higher than those seen in the corresponding correlations. A possible explanation is that a frequency shift may also be induced by the excitation of the sample which is not picked up by examining the spatial correlations alone, but does act to reduce the constructive interference contributing to the optimised spot.

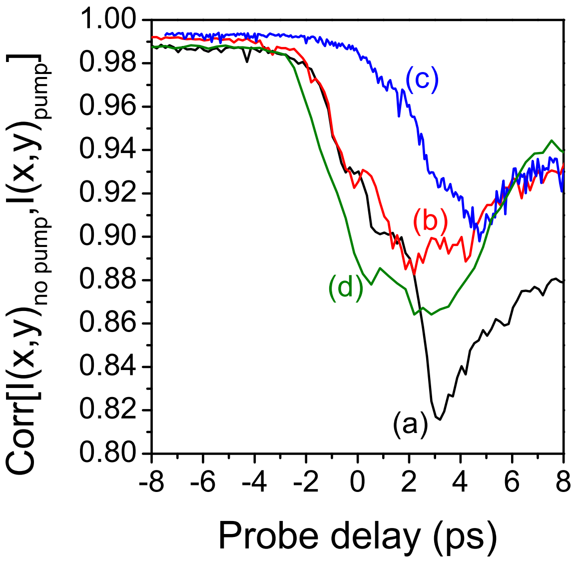

Figure 6.9: Speckle correlations as a function of pump-probe delay corresponding to the data shown in Figure 6.8 and Figure 6.7 (a-d).

6.4 Rephasing of shaped wavefront

As an additional experiment, it is interesting to consider how performing an optimisation with the pump on at different delay positions changes the optimisation process. If an optimised spot can be created which depends on the phase shifts induced by the pump, the opposite case to the previous experiment could be created. Instead switching off the optimised spot, in this case the excitation by the pump would act to 'rephase' the created focus. Besides demonstrating beyond doubt the importance of dephasing to the effects seen previously as the effect of absorption could not be reversed in this way, this would also demonstrate that the phase shifts induced by the pump are stable over the time period of an optimisation.

As seen in the previous section, the exact behavior of the dephasing observed varied greatly between different sample positions. Therefore, the pump-probe delay at which the maximum effect of the pump available for the desired rephasing effect was uncertain. The experiment was performed by carrying out optimisations with the pump on at a range of different pump probe delays on the same sample position, then scanning the pump-probe delay taking images with pump on and off as for the previous experiment. The results of this approach are shown in Figure 6.10.

Figure 6.10(a) shows the modulation of the background for each optimisation, with the pump probe delay for each data set indicated by the black arrows. As expected. the behavior of the background shows no dependence on the pump probe delay used for the optimisation. In constant, increases in the peak to background ratio can be seen at the pump-probe delay at which the optimisation was carried out in Figure 6.10(b).

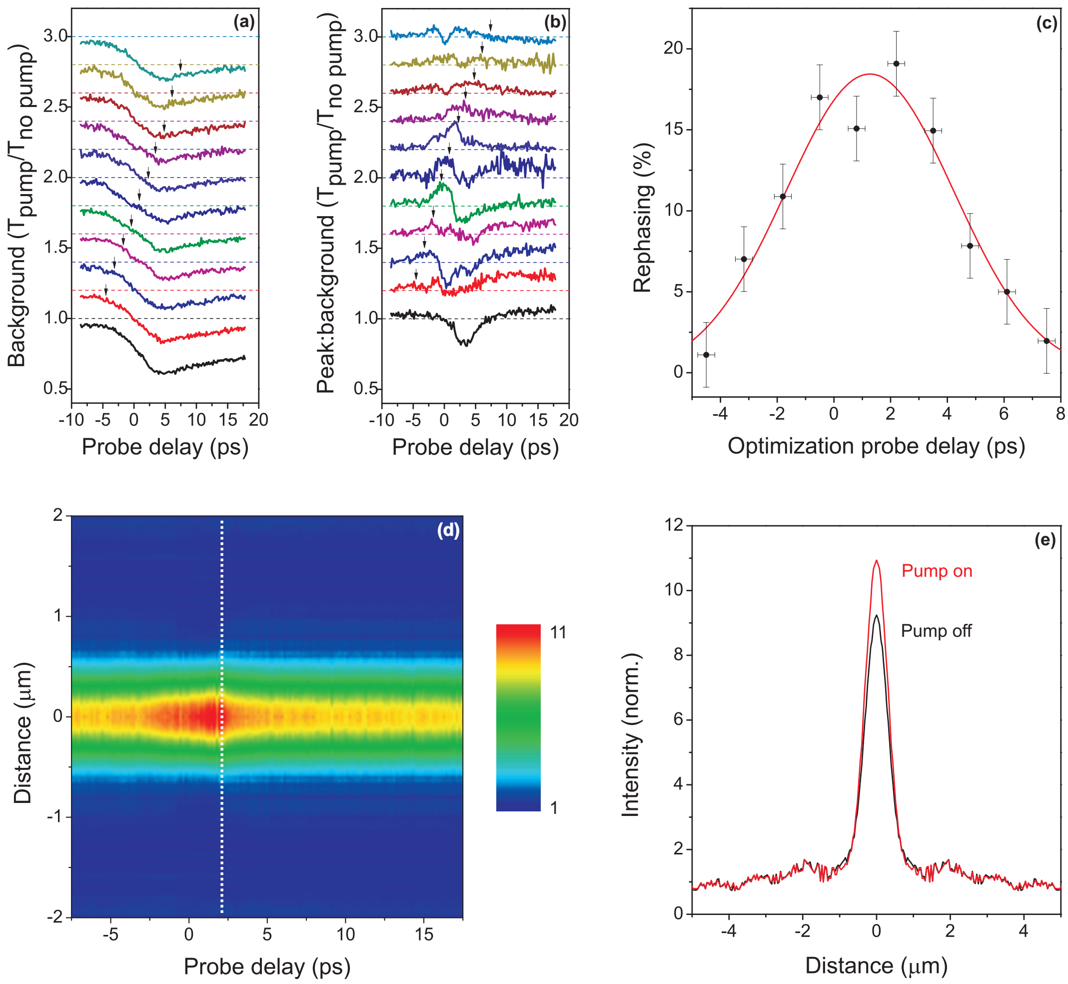

Figure 6.10: Plots of the background and peak to background $\Delta T/T$ as a function of pump-probe delay for optimisations carried out with the pump on with different delays (indicated by black arrows). Black line shows an optimisation carried out with pump blocked for reference. (c) Maximum rephasing effects as a function of delay for which optimisation is carried out at. Radially averaged cross-section (normalised to average background)of spot optimised at a pump-probe delay of 2.2 ps as a function of pump-probe delay (d) and with pump blocked (black line) and unblocked (red line) (d).

Figure 6.10(c) shows the rephasing effect attained for each optimisation probe delay. The effect has a maximum of $18 \pm 2\%$ around a delay of 2 ps.

Figure 6.10(d) and (e) show radially averaged cross sections of the optimisation carried out at a delay of 2.2 ps both as a function of probe delay and with pump on and pump off. Both are normalised to the average background in order to show the effect on the peak, as the effect of absorption is sufficiently strong to prevent the effect resulting in an absolute increase in peak intensity. It is clear that the quality of the optimised spot is increased by the presence of the pump in the reverse of experiments in the previous chapter, and this improvement is dependent on the exact delay between pump and probe. This is striking evidence of a rephasing effect, and the magnitude of the effect and its presence at a delay of 2 ps is consistent with the features seen for the dephasing effect previously.

Similar effects were reproduced on four separate sample positions, as shown by the cross-sections in Figure 6.11. In all cases, a rephasing above 17 ± 2 was achieved.

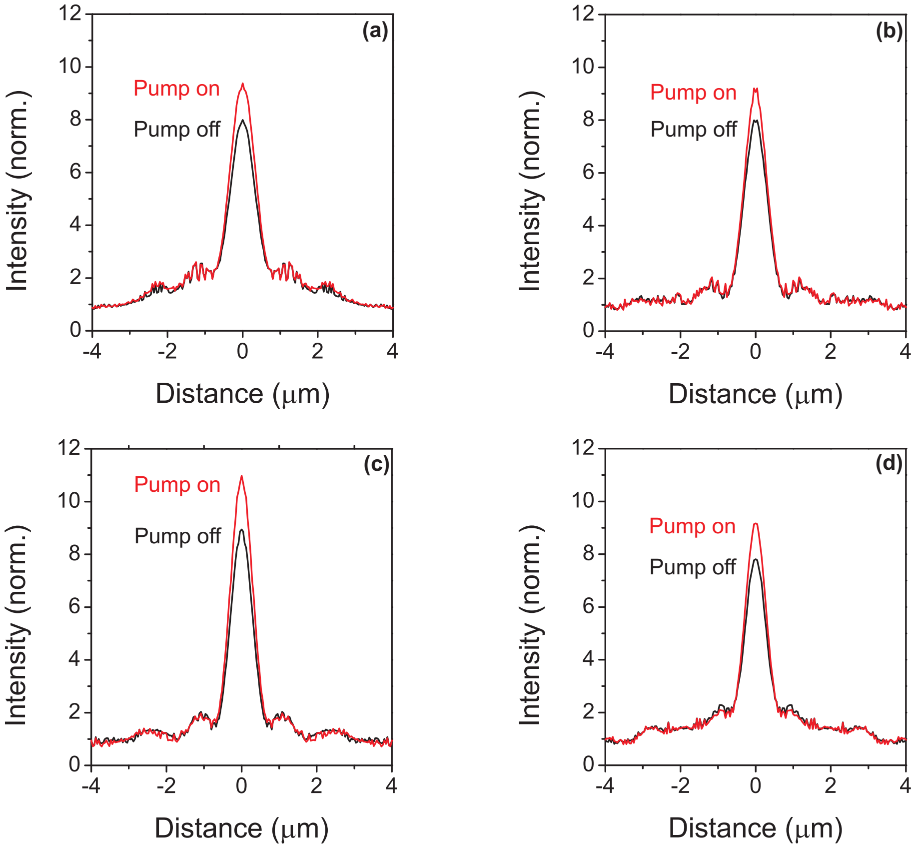

Figure 6.11: (a-d) Radially averaged cross-sections normalised to average background showing rephasing effects above 17% achieved on four separate sample positions.

Examining the dynamics of this rephasing shown in Figure 6.12, it is again apparent that the exact behavior depends on the local sample configuration. The delay resulting in the peak rephasing effect varies between 1.1 and 4.2 ps for these 4 sample positions.

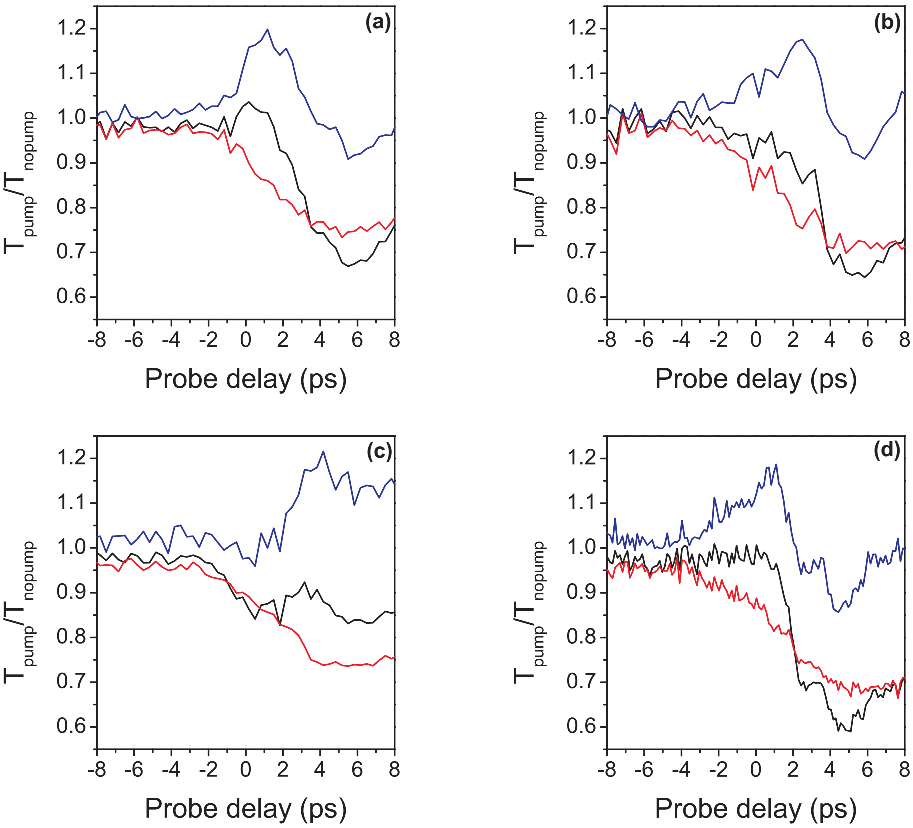

Figure 6.12: (a-d) Plots of background $\Delta T/T$ (red lines), peak modulation (black lines) and peak to background $\Delta T/T$(blue lines) as a function of pump-probe delay, showing the dynamics of the rephasing on different sample positions of Figure 6.11 (a-d)

6.5 Conclusion

The switching of an optimised speckle created through wavefront shaping techniques was achieved by harnessing the intrinsic nonlinearity of disordered semiconductor nanowire mats with ultrafast optical excitation. Modulations in the peak intensity of up to 63±2% were achieved, with induced absorption and dephasing found to have approximately equal contributions. It was found that most of the dephasing effect could be reversed in a striking rephasing effect in which an optimised spot was created which depended upon the phase shifts induced by the pump light. Interestingly, the exact details of the dephasing and rephasing effects were found to vary considerably between sample positions, indicating that their exact behavior contains information about the exact speckle optimised on.

The quality of optimisation achieved were relatively low compared to those in literature, especially compared to results using phase modulation. However, it is exciting that such a relatively simple and accessible method is sufficient to demonstrate the principle of a reconfigurable photonic switch which may have applications in telecommunications. It is anticipated that the use of more complex schemes such as off axis holography to allow phase modulation with the DMD [88] would result in much higher enhancements of the optimised spot. While nanowire samples were used for this investigation, they are by no means certain to be the best candidates, and it is likely that materials designed to maximise the effects demonstrated here could achieve higher modulations.

Chapter 7

Summary

In this thesis the transport of light through dense disordered mats of nanowires was investigated. The scattering strength of these samples is such that a 6 μm thick layer is an impressive 30 optical mean free paths thick, allowing the fundamental properties of light in the presence of strong disorder to be investigated. It was found that the transport through such layers is described by only a few independent transmission channels, indicating these samples are close to the Anderson localisation transition. While this does not answer the question of whether localisation of light is possible in three dimensions, it does show that it is possible to approach it. However, the fact that localisation is not seen in a sample at the limit of scattering strength currently achievable once more underlines the difficulty in chasing Anderson localisation of light. It should also be noted that a tightly focused illumination was used to achieve this result, meaning the spread of light within the medium plays an important role. While the expanding waveguide model used to account for this is attractive, it poses a conceptual difficulty as the number of transmission channels can always be increased by increasing the illumination area. It could then be argued that in order to conclusively demonstrate localisation an illumination larger than the width of the slab should be used.

The nonlinearity due to the semiconductor nature of the nanowire samples allowed the switching of an optimised wavefront by ultrafast optical excitation to be investigated. The maximum modulation achieved in the proof of principle experiment of around 60% is promising, and it is exciting to consider how this could be combined with the exciting possibilities offered by wavefront shaping for possible applications as a reconfigurable photonic switch. It is expected that with the use of a phase modulation scheme a much higher quality of optimisation could be achieved. It is also entirely possible that the nanowire samples optimised for high scattering strength are not the ideal material for this application and a larger effect is possible in a different system. The exact dynamics of the excitation of the nanowires is also not fully understood, which is another potential avenue for future investigations.

In summary, the Author feels privileged to have had the opportunity to work with samples with such interesting properties, allowing a variety of different physical effects to be explored. The field of disordered photonic media is a fascinating one, addressing both the fundamental properties of light transport and the advantages of harnessing disorder for applications. There are many interesting potential avenues of investigation following on from the work presented here, and it seems to the Author that three and a half years has passed all too quickly.

References

[1] Otto L Muskens, Jaime Gómez Rivas, Rienk E Algra, Erik P A M Bakkers, and Ad Lagendijk. Design of light scattering in nanowire materials for photovoltaic applications. *Nano letters*, 8(9):2638–42, September 2008. ISSN 1530-6984. doi: 10.1021/nl0808076. URL `http://dx.doi.org/10.1021/nl0808076`.

[2] Tom Strudley, Tilman Zehender, Claire Blejean, Erik P A M Bakkers, and Otto L Muskens. Mesoscopic light transport by very strong collective multiple scattering in nanowire mats. *Nature Photonics*, (5):1–6, 2013. doi: 10.1038/NPHOTON.2013.62. URL `http://dx.doi.org/10.1038/nphoton.2013.62`.

[3] Tom Strudley, Roman Bruck, Ben Mills, and Otto L Muskens. An ultrafast reconfigurable nanophotonic switch using wavefront shaping of light in a nonlinear nanomaterial. *Light: Science and Applications*, 2014.

[4] T. Strudley, D. Akbulut, W. L. Vos, A. Lagendijk, A. P. Mosk, and O. L. Muskens. Observation of Intensity Statistics of Light Transmitted Through 3D Random Media. *ArXiv e-prints*, July 2014.

[5] United Nations. International Years, United Nations Observances, 2014. URL `http://www.un.org/en/events/observances/years.shtml`.

[6] Diederik S Wiersma. Disordered photonics. *Nature Photonics*, 7(3), 2013. doi: 10.1038/NPHOTON.2013.29.

[7] Isaac Freund, Michael Rosenbluh, and Shechao Feng. Memory Effects in Propagation of Optical Waves through Disordered Media. *Physical Review Letters*, 61(20): 2328–2331, November 1988. ISSN 0031-9007. doi: 10.1103/PhysRevLett.61.2328. URL `http://link.aps.org/doi/10.1103/PhysRevLett.61.2328`.

[8] Jacopo Bertolotti, Elbert G van Putten, Christian Blum, Ad Lagendijk, Willem L Vos, and Allard P Mosk. Non-invasive imaging through opaque scattering layers. *Nature*, 491(7423):232–4, November 2012. ISSN 1476-4687. doi: 10.1038/nature11578. URL `http://dx.doi.org/10.1038/nature11578`.

[9] Ori Katz, Eran Small, and Yaron Silberberg. Looking around corners and through thin turbid layers in real time with scattered incoherent light. *Nature Photonics*,

6(8):549–553, July 2012. ISSN 1749-4885. doi: 10.1038/nphoton.2012.150. URL `http://dx.doi.org/10.1038/nphoton.2012.150`.

[10] Emmett N. Leith and Juriso Upatnieks. Holographic Imagery Through Diffusing Media. *Journal of the Optical Society of America*, 56(4):523, April 1966. ISSN 0030-3941. doi: 10.1364/JOSA.56.000523. URL `http://www.opticsinfobase.org/abstract.cfm?URI=josa-56-4-523`.

[11] Arnaud Derode, Philippe Roux, and Mathias Fink. Robust Acoustic Time Reversal with High-Order Multiple Scattering. *Physical Review Letters*, 75(23):4206–4209, December 1995. ISSN 0031-9007. doi: 10.1103/PhysRevLett.75.4206. URL `http://link.aps.org/doi/10.1103/PhysRevLett.75.4206`.

[12] Fabrice Lemoult, Mathias Fink, and Geoffroy Lerosey. Acoustic Resonators for Far-Field Control of Sound on a Subwavelength Scale. *Physical Review Letters*, 107 (6):064301, August 2011. ISSN 0031-9007. doi: 10.1103/PhysRevLett.107.064301. URL `http://link.aps.org/doi/10.1103/PhysRevLett.107.064301`.

[13] G. Lerosey, J. de Rosny, A. Tourin, A. Derode, G. Montaldo, and M. Fink. Time Reversal of Electromagnetic Waves. *Physical Review Letters*, 92(19): 193904, May 2004. ISSN 0031-9007. doi: 10.1103/PhysRevLett.92.193904. URL `http://link.aps.org/doi/10.1103/PhysRevLett.92.193904`.

[14] Geoffroy Lerosey, Julien de Rosny, Arnaud Tourin, and Mathias Fink. Focusing beyond the diffraction limit with far-field time reversal. *Science (New York, N.Y.)*, 315(5815):1120–2, February 2007. ISSN 1095-9203. doi: 10.1126/science.1134824. URL `http://www.sciencemag.org/content/315/5815/1120.abstract`.

[15] a. Przadka, S. Feat, P. Petitjeans, V. Pagneux, a. Maurel, and M. Fink. Time Reversal of Water Waves. *Physical Review Letters*, 109(6):064501, August 2012. ISSN 0031-9007. doi: 10.1103/PhysRevLett.109.064501. URL `http://link.aps.org/doi/10.1103/PhysRevLett.109.064501`.

[16] I. M. Vellekoop and A. P. Mosk. Focusing coherent light through opaque strongly scattering media. *Optics Letters*, 32(16):2309, 2007. ISSN 0146-9592. doi: 10.1364/OL.32.002309. URL `http://ol.osa.org/abstract.cfm?URI=ol-32-16-2309`.

[17] I. M. Vellekoop, A. Lagendijk, and A. P. Mosk. Exploiting disorder for perfect focusing. *Nature Photonics*, 4(5):320–322, February 2010. ISSN 1749-4885. doi: 10.1038/nphoton.2010.3. URL `http://dx.doi.org/10.1038/nphoton.2010.3`.

[18] I. Vellekoop and A. Mosk. Universal Optimal Transmission of Light Through Disordered Materials. *Physical Review Letters*, 101(12):120601, September 2008. ISSN 0031-9007. doi: 10.1103/PhysRevLett.101.120601. URL `http://link.aps.org/doi/10.1103/PhysRevLett.101.120601`.

[19] S.M. Popoff, A. Goetschy, S.F. Liew, A.D. Stone, and H Cau. Focusing coherent light through opaque strongly scattering media. *Physical Review Letters*, (112):133903, 2014. ISSN 0146-9592. doi: 10.1103/PhysRevLett.112.133903. URL `http://journals.aps.org/prl/abstract/10.1103/PhysRevLett.112.133903`.

[20] S. M. Popoff, G. Lerosey, R. Carminati, M. Fink, A. C. Boccara, and S. Gigan. Measuring the Transmission Matrix in Optics: An Approach to the Study and Control of Light Propagation in Disordered Media. *Physical Review Letters*, 104 (10):100601, March 2010. ISSN 0031-9007. doi: 10.1103/PhysRevLett.104.100601. URL `http://link.aps.org/doi/10.1103/PhysRevLett.104.100601`.

[21] Moonseok Kim, Youngwoon Choi, Changhyeong Yoon, Wonjun Choi, Jaisoon Kim, Q-Han Park, and Wonshik Choi. Maximal energy transport through disordered media with the implementation of transmission eigenchannels. *Nature Photonics*, 6(9):583–587, July 2012. ISSN 1749-4885. doi: 10.1038/nphoton.2012.159. URL `http://dx.doi.org/10.1038/nphoton.2012.159`.

[22] Allard P. Mosk, Ad Lagendijk, Geoffroy Lerosey, and Mathias Fink. Controlling waves in space and time for imaging and focusing in complex media. *Nature Photonics*, 6(5):283–292, May 2012. ISSN 1749-4885. doi: 10.1038/nphoton.2012.88. URL `http://dx.doi.org/10.1038/nphoton.2012.88`.

[23] Brandon Redding and Hui Cao. Using a multimode fiber as a high-resolution, low-loss spectrometer. *Optics letters*, 37(16):3384–6, August 2012. ISSN 1539-4794. doi: 10.1364/OL.37.003384. URL `http://ol.osa.org/abstract.cfm?URI=ol-37-16-3384`.

[24] S. Mokkapati and K. R. Catchpole. Nanophotonic light trapping in solar cells. *Journal of Applied Physics*, 112(10):101101, November 2012. ISSN 00218979. doi: 10.1063/1.4747795. URL `http://scitation.aip.org/content/aip/journal/jap/112/10/10.1063/1.4747795`.

[25] Diederik S. Wiersma. The physics and applications of random lasers. *Nature Physics*, 4(5):359–367, May 2008. ISSN 1745-2473. doi: 10.1038/nphys971. URL `http://dx.doi.org/10.1038/nphys971`.

[26] N. Bachelard, J. Andreasen, S. Gigan, and P. Sebbah. Taming Random Lasers through Active Spatial Control of the Pump. *Physical Review Letters*, 109(3): 033903, July 2012. ISSN 0031-9007. doi: 10.1103/PhysRevLett.109.033903. URL `http://link.aps.org/doi/10.1103/PhysRevLett.109.033903`.

[27] N. Bachelard, S. Gigan, X. Noblin, and P. Sebbah. Adaptive pumping for spectral control of random lasers. *Nature Physics*, page 033903, April 2014. doi: 10.1038/nphys2939. URL `http://www.nature.com/nphys/journal/vaop/ncurrent/full/nphys2939.html`.

[28] PW Anderson. Absence of diffusion in certain random lattices. *Physical review*, 1958. URL `http://prola.aps.org/abstract/PR/v109/i5/p1492_1`.

[29] Ad Lagendijk, Bart van Tiggelen, and Diederik S. Wiersma. Fifty years of Anderson localization. *Physics Today*, 62(8):24, August 2009. ISSN 00319228. doi: 10.1063/1.3206091. URL `http://scitation.aip.org/content/aip/magazine/physicstoday/article/62/8/10.1063/1.320609`

[30] Hefei Hu, A. Strybulevych, J. H. Page, S. E. Skipetrov, and B. A. van Tiggelen. Localization of ultrasound in a three-dimensional elastic network. *Nature Physics*, 4(12):945–948, October 2008. ISSN 1745-2473. doi: 10.1038/nphys1101. URL `http://arxiv.org/abs/0805.1502`.

[31] A A Chabanov, M Stoytchev, and A Z Genack. Statistical Signatures of Photon Localization. *Nature*, 404(6780):5, 2001. URL `http://arxiv.org/abs/cond-mat/0108182`.

[32] Juliette Billy, Vincent Josse, Zhanchun Zuo, Alain Bernard, Ben Hambrecht, Pierre Lugan, David Clément, Laurent Sanchez-Palencia, Philippe Bouyer, and Alain Aspect. Direct observation of Anderson localization of matter waves in a controlled disorder. *Nature*, 453(7197):891–4, July 2008. ISSN 1476-4687. doi: 10.1038/nature07000. URL `http://dx.doi.org/10.1038/nature07000`.

[33] Jongchul Park, Sheng Zhang, and Azriel Z. Genack. Intensity statistics and photon localization beyond one dimension. *Physical Review E*, 82(4):045101, October 2010. ISSN 1539-3755. doi: 10.1103/PhysRevE.82.045101. URL `http://link.aps.org/doi/10.1103/PhysRevE.82.045101`.

[34] Tal Schwartz, Guy Bartal, Shmuel Fishman, and Mordechai Segev. Transport and Anderson localization in disordered two-dimensional photonic lattices. *Nature*, 446(7131):52–5, March 2007. ISSN 1476-4687. doi: 10.1038/nature05623. URL `http://dx.doi.org/10.1038/nature05623`.

[35] Hans De Raedt, Ad Lagendijk, and Pedro de Vries. Transverse Localization of Light. *Physical Review Letters*, 62(1):47–50, January 1989. ISSN 0031-9007. doi: 10.1103/PhysRevLett.62.47. URL `http://link.aps.org/doi/10.1103/PhysRevLett.62.47`.

[36] Diederik S. Wiersma, Paolo Bartolini, Ad Lagendijk, and Roberto Righini. Localization of light in a disordered medium. *Nature*, 390(6661):671–673, December 1997. ISSN 0028-0836. doi: 10.1038/37757. URL `http://dx.doi.org/10.1038/37757`.

[37] C. M. Aegerter, M. Störzer, W. Bührer, S. Fiebig, and G. Maret. Experimental signatures of Anderson localization of light in three dimensions. *Journal of Modern Optics*, 54(16-17):2667–2677, November

2007. ISSN 0950-0340. doi: 10.1080/09500340701627206. URL `http://www.tandfonline.com/doi/abs/10.1080/09500340701627206`.

[38] T. Sperling, W. Bührer, C. M. Aegerter, and G. Maret. Direct determination of the transition to localization of light in three dimensions. *Nature Photonics*, 7(1): 48–52, December 2012. ISSN 1749-4885. doi: 10.1038/nphoton.2012.313. URL `http://dx.doi.org/10.1038/nphoton.2012.313`.

[39] Frank Scheffold, Ralf Lenke, Ralf Tweer, and Georg Maret. Localization or classical diffusion of light? *Nature*, 72(1998), 1999. URL `http://www.nature.com/nature/journal/v398/n6724/abs/398206a0.html`.

[40] S.E. Skipetrov and I.M. Sokolov. Absence of Anderson Localization of Light in a Random Ensemble of Point Scatterers. *Physical Review Letters*, 112(2):023905, January 2014. ISSN 0031-9007. doi: 10.1103/PhysRevLett.112.023905. URL `http://link.aps.org/doi/10.1103/PhysRevLett.112.023905`.

[41] E Akkermans and G Montambaux. *Mesoscopic Physics of Electrons and Photons*. Cambridge University Press, 2007. ISBN 9780521855129. URL `http://books.google.com/books?id=cs7AVel15TAC&pgis=1`.

[42] R. Gómez-Medina, L. S. Froufe-Pérez, M. Yépez, F. Scheffold, M. Nieto-Vesperinas, and J. J. Sáenz. Negative scattering asymmetry parameter for dipolar particles: Unusual reduction of the transport mean free path and radiation pressure. *Physical Review A*, 85(3):035802, March 2012. ISSN 1050-2947. doi: 10.1103/PhysRevA.85.035802. URL `http://link.aps.org/doi/10.1103/PhysRevA.85.035802`.

[43] O.N. Dorokhov. On the coexistence of localized and extended electronic states in the metallic phase. *Solid State Communications*, 51(6):381–384, August 1984. ISSN 00381098. doi: 10.1016/0038-1098(84)90117-0. URL `http://www.sciencedirect.com/science/article/pii/0038109884901170`.

[44] C. Beenakker. Random-matrix theory of quantum transport. *Reviews of Modern Physics*, 69(3):731–808, July 1997. ISSN 0034-6861. doi: 10.1103/RevModPhys.69.731. URL `http://link.aps.org/doi/10.1103/RevModPhys.69.731`.

[45] Y Imry. Active Transmission Channels and Universal Conductance Fluctuations. *Europhysics Letters (EPL)*, 1(5):249–256, March 1986. ISSN 0295-5075. doi: 10.1209/0295-5075/1/5/008. URL `http://iopscience.iop.org/0295-5075/1/5/008`.

[46] MJ Stephen and G Cwilich. Intensity correlation functions and fluctuations in light scattered from a random medium. *Physical review letters*, 1987. URL `http://link.aps.org/doi/10.1103/PhysRevLett.59.285`.

[47] M. van Rossum, Th. Nieuwenhuizen, and R. Vlaming. Optical conductance fluctuations: Diagrammatic analysis in the Landauer approach and nonuniversal effects. *Physical Review E*, 51(6):6158–6176, June 1995. ISSN 1063-651X. doi: 10.1103/PhysRevE.51.6158. URL `http://link.aps.org/doi/10.1103/PhysRevE.51.6158`.

[48] B. Shapiro. Large Intensity Fluctuations for Wave Propagation in Random Media. *Physical Review Letters*, 57(17):2168–2171, October 1986. ISSN 0031-9007. doi: 10.1103/PhysRevLett.57.2168. URL `http://link.aps.org/doi/10.1103/PhysRevLett.57.2168`.

[49] Eugene Kogan, Moshe Kaveh, Rene Baumgartner, and Richard Berkovits. Statistics of waves propagating in a random medium. *Physical Review B*, 48(13):9404–9410, October 1993. ISSN 0163-1829. doi: 10.1103/PhysRevB.48.9404. URL `http://link.aps.org/doi/10.1103/PhysRevB.48.9404`.

[50] Th. Nieuwenhuizen and M. van Rossum. Intensity Distributions of Waves Transmitted through a Multiple Scattering Medium. *Physical Review Letters*, 74(14): 2674–2677, April 1995. ISSN 0031-9007. doi: 10.1103/PhysRevLett.74.2674. URL `http://link.aps.org/doi/10.1103/PhysRevLett.74.2674`.

[51] Johannes de Boer, Meint van Albada, and Ad Lagendijk. Transmission and intensity correlations in wave propagation through random media. *Physical Review B*, 45(2): 658–666, January 1992. ISSN 0163-1829. doi: 10.1103/PhysRevB.45.658. URL `http://link.aps.org/doi/10.1103/PhysRevB.45.658`.

[52] Frank Scheffold, Wolfram Härtl, Georg Maret, and Egon Matijević. Observation of long-range correlations in temporal intensity fluctuations of light. *Physical Review B*, 56(17):10942–10952, November 1997. ISSN 0163-1829. doi: 10.1103/PhysRevB.56.10942. URL `http://link.aps.org/doi/10.1103/PhysRevB.56.10942`.

[53] Frank Scheffold and Georg Maret. Universal Conductance Fluctuations of Light. *Physical Review Letters*, 81(26):5800–5803, December 1998. ISSN 0031-9007. doi: 10.1103/PhysRevLett.81.5800. URL `http://link.aps.org/doi/10.1103/PhysRevLett.81.5800`.

[54] Georg Maret, Tilo Sperling, Wolfgang Bührer, Andreas Lubatsch, Regine Frank, and Christof M. Aegerter. Inelastic scattering puts in question recent claims of Anderson localization of light. *Nature Photonics*, 7(12):934–935, November 2013. ISSN 1749-4885. doi: 10.1038/nphoton.2013.281. URL `http://dx.doi.org/10.1038/nphoton.2013.281`.

[55] Erik Garnett and Peidong Yang. Light trapping in silicon nanowire solar cells. *Nano letters*, 10(3):1082–7, March 2010. ISSN 1530-6992. doi: 10.1021/nl100161z. URL `http://dx.doi.org/10.1021/nl100161z`.

[56] Michael D Kelzenberg, Daniel B Turner-Evans, Brendan M Kayes, Michael A Filler, Morgan C Putnam, Nathan S Lewis, and Harry A Atwater. Photovoltaic measurements in single-nanowire silicon solar cells. *Nano letters*, 8 (2):710–4, March 2008. ISSN 1530-6984. doi: 10.1021/nl072622p. URL `http://dx.doi.org/10.1021/nl072622p`.

[57] Thomas J Kempa, Bozhi Tian, Dong Rip Kim, Jinsong Hu, Xiaolin Zheng, and Charles M Lieber. Single and tandem axial p-i-n nanowire photovoltaic devices. *Nano letters*, 8(10):3456–60, October 2008. ISSN 1530-6984. doi: 10.1021/nl8023438. URL `http://dx.doi.org/10.1021/nl8023438`.

[58] Bozhi Tian, Xiaolin Zheng, Thomas J Kempa, Ying Fang, Nanfang Yu, Guihua Yu, Jinlin Huang, and Charles M Lieber. Coaxial silicon nanowires as solar cells and nanoelectronic power sources. *Nature*, 449(7164):885–9, October 2007. ISSN 1476-4687. doi: 10.1038/nature06181. URL `http://dx.doi.org/10.1038/nature06181`.

[59] Jesper Wallentin, Nicklas Anttu, Damir Asoli, Maria Huffman, Ingvar Aberg, Martin H Magnusson, Gerald Siefer, Peter Fuss-Kailuweit, Frank Dimroth, Bernd Witzigmann, H Q Xu, Lars Samuelson, Knut Deppert, and Magnus T Borgström. InP nanowire array solar cells achieving 13.8% efficiency by exceeding the ray optics limit. *Science (New York, N.Y.)*, 339(6123):1057–60, March 2013. ISSN 1095-9203. doi: 10.1126/science.1230969. URL `http://www.sciencemag.org/content/339/6123/1057.abstract`.

[60] Peter Krogstrup, Henrik Ingerslev Jø rgensen, Martin Heiss, Olivier Demichel, Jeppe V Holm, Martin Aagesen, Jesper Nygard, and Anna Fontcuberta. Single-nanowire solar cells beyond the Shockley-Queisser limit. *Nature Photonics*, (7): 306–310, 2013. doi: 10.1038/NPHOTON.2013.32.

[61] Otto L Muskens, Silke L Diedenhofen, Bernard C Kaas, Rienk E Algra, Erik P A M Bakkers, Jaime Gomez Rivas, and Ad Lagendijk. Large photonic strength of highly tunable resonant nanowire materials. *Nano letters*, 9(3):930–4, March 2009. ISSN 1530-6984. doi: 10.1021/nl802580r. URL `http://dx.doi.org/10.1021/nl802580r`.

[62] Meint Albada and Ad Lagendijk. Observation of Weak Localization of Light in a Random Medium. *Physical Review Letters*, 55(24):2692–2695, December 1985. ISSN 0031-9007. doi: 10.1103/PhysRevLett.55.2692. URL `http://link.aps.org/doi/10.1103/PhysRevLett.55.2692`.

[63] E Akkermans, PE Wolf, and R Maynard. Coherent backscattering of light by disordered media: Analysis of the peak line shape. *Physical review letters*, 56(14):1471–1474, 1986. URL `http://link.aps.org/doi/10.1103/PhysRevLett.56.1471`.

[64] R. Corey. Coherent backscattering of light. *American Journal of Physics*, 63(6):560, June 1995. ISSN 00029505. doi: 10.1119/1.17868. URL `http://scitation.aip.org/content/aapt/journal/ajp/63/6/10.1119/1.17868`.

[65] JX Zhu, DJ Pine, and DA Weitz. Internal reflection of diffusive light in random media. *Physical review. A*, 44(6):3948–3959, September 1991. ISSN 1050-2947. URL `http://www.ncbi.nlm.nih.gov/pubmed/9906412`.

[66] a Z Genack and a a Chabanov. Signatures of photon localization. *Journal of Physics A: Mathematical and General*, 38(49):10465–10488, December 2005. ISSN 0305-4470. doi: 10.1088/0305-4470/38/49/002. URL `http://stacks.iop.org/0305-4470/38/i=49/a=002?key=crossref.63bd132bff62cf6033d985146b0f`

[67] N. Shnerb and M. Kaveh. Non-Rayleigh statistics of waves in random systems. *Physical Review B*, 43(1):1279–1282, January 1991. ISSN 0163-1829. doi: 10.1103/PhysRevB.43.1279. URL `http://link.aps.org/doi/10.1103/PhysRevB.43.1279`.

[68] D.J. Thouless, R. Balian, R. Maynard, and G. Toulouse. *Ill-condensed Matter*. North-Holland Publishing Company and World Scientific Publishing Co., 1983. ISBN 997195060X. URL `http://books.google.com/books?id=J4Q9oElF9h8C&pgis=1`.

[69] Eugene Kogan and Moshe Kaveh. Random-matrix-theory approach to the intensity distributions of waves propagating in a random medium. *Physical Review B*, 52(6): R3813–R3815, August 1995. ISSN 0163-1829. doi: 10.1103/PhysRevB.52.R3813. URL `http://link.aps.org/doi/10.1103/PhysRevB.52.R3813`.

[70] R. Höhmann, U. Kuhl, H.-J. Stöckmann, L. Kaplan, and E. J. Heller. Freak Waves in the Linear Regime: A Microwave Study. *Physical Review Letters*, 104 (9):093901, March 2010. ISSN 0031-9007. doi: 10.1103/PhysRevLett.104.093901. URL `http://link.aps.org/doi/10.1103/PhysRevLett.104.093901`.

[71] A. Chabchoub, N. P. Hoffmann, and N. Akhmediev. Rogue Wave Observation in a Water Wave Tank. *Physical Review Letters*, 106(20):204502, May 2011. ISSN 0031-9007. doi: 10.1103/PhysRevLett.106.204502. URL `http://link.aps.org/doi/10.1103/PhysRevLett.106.204502`.

[72] D R Solli, C Ropers, P Koonath, and B Jalali. Optical rogue waves. *Nature*, 450 (7172):1054–7, December 2007. ISSN 1476-4687. doi: 10.1038/nature06402. URL `http://dx.doi.org/10.1038/nature06402`.

[73] A. García-Martín, F. Scheffold, M. Nieto-Vesperinas, and J. Sáenz. Finite-Size Effects on Intensity Correlations in Random Media. *Physical Review Letters*, 88 (14):143901, March 2002. ISSN 0031-9007. doi: 10.1103/PhysRevLett.88.143901. URL `http://link.aps.org/doi/10.1103/PhysRevLett.88.143901`.

[74] K. Muttalib, P. Markoš, and P. Wölfle. Conductance distribution in strongly disordered mesoscopic systems in three dimensions. *Physical Review B*, 72(12): 125317, September 2005. ISSN 1098-0121. doi: 10.1103/PhysRevB.72.125317. URL `http://link.aps.org/doi/10.1103/PhysRevB.72.125317`.

[75] B. Shapiro. New Type of Intensity Correlation in Random Media. *Physical Review Letters*, 83(23):4733–4735, December 1999. ISSN 0031-9007. doi: 10.1103/PhysRevLett.83.4733. URL `http://link.aps.org/doi/10.1103/PhysRevLett.83.4733`.

[76] B A van Tiggelen and S E Skipetrov. Fluctuations of local density of states and C0 speckle correlations are equal. *Physical review. E, Statistical, nonlinear, and soft matter physics*, 73(4 Pt 2):045601, April 2006. ISSN 1539-3755. URL `http://www.ncbi.nlm.nih.gov/pubmed/16711869`.

[77] W.K. Hildebrand, A. Strybulevych, S.E. Skipetrov, B.A. van Tiggelen, and J.H. Page. Observation of Infinite-Range Intensity Correlations above, at, and below the Mobility Edges of the 3D Anderson Localization Transition. *Physical Review Letters*, 112(7):073902, February 2014. ISSN 0031-9007. doi: 10.1103/PhysRevLett.112.073902. URL `http://link.aps.org/doi/10.1103/PhysRevLett.112.073902`.

[78] P. Sebbah, B. Hu, A. Genack, R. Pnini, and B. Shapiro. Spatial-Field Correlation: The Building Block of Mesoscopic Fluctuations. *Physical Review Letters*, 88(12): 123901, March 2002. ISSN 0031-9007. doi: 10.1103/PhysRevLett.88.123901. URL `http://link.aps.org/doi/10.1103/PhysRevLett.88.123901`.

[79] Ad Lagendijk, Rob Vreeker, and Pedro De Vries. Influence of internal reflection on diffusive transport in strongly scattering media. *Physics Letters A*, 136(1-2): 81–88, March 1989. ISSN 03759601. doi: 10.1016/0375-9601(89)90683-X. URL `http://adsabs.harvard.edu/abs/1989PhLA..136...81L`.

[80] M.C.W. van Rossum and Th.M. Nieuwenhuizen. Influence of skin layers on speckle correlations of light transmitted through disordered media. *Physics Letters A*, 177 (6):452–458, June 1993. ISSN 03759601. doi: 10.1016/0375-9601(93)90976-7. URL `http://www.sciencedirect.com/science/article/pii/0375960193909767`.

[81] A. Lisyansky and D. Livdan. Influence of internal reflection on correlation of intensity fluctuation in random media. *Physical Review B*, 47(21):14157–14164, June 1993. ISSN 0163-1829. doi: 10.1103/PhysRevB.47.14157. URL `http://link.aps.org/doi/10.1103/PhysRevB.47.14157`.

[82] L. V. Korolev and D. B. Rogozkin. Long-range correlations upon wave propagation in random media under the conditions of strong internal reflection from their boundaries. *Journal of Experimental and Theoretical Physics*, 86

(1):164–176, January 1998. ISSN 1063-7761. doi: 10.1134/1.558486. URL `http://link.springer.com/10.1134/1.558486`.

[83] Mathias Fink. Imaging: Sharper focus by random scattering. *Nature Photonics*, 4(5):269–271, May 2010. ISSN 1749-4885. doi: 10.1038/nphoton.2010.95. URL `http://dx.doi.org/10.1038/nphoton.2010.95`.

[84] Eran Small, Ori Katz, Yefeng Guan, and Yaron Silberberg. Spectral control of broadband light through random media by wavefront shaping. *Optics letters*, 37 (16):3429–31, August 2012. ISSN 1539-4794. doi: 10.1364/OL.37.003429. URL `http://ol.osa.org/abstract.cfm?URI=ol-37-16-3429`.

[85] Matthieu Davy, Zhou Shi, and Azriel Genack. Focusing through random media: Eigenchannel participation number and intensity correlation. *Physical Review B*, 85(3):035105, January 2012. ISSN 1098-0121. doi: 10.1103/PhysRevB.85.035105. URL `http://link.aps.org/doi/10.1103/PhysRevB.85.035105`.

[86] Donald B Conkey, Antonio M Caravaca-Aguirre, and Rafael Piestun. High-speed scattering medium characterization with application to focusing light through turbid media. *Optics express*, 20(2):1733–40, January 2012. ISSN 1094-4087. doi: 10.1364/OE.20.001733. URL `http://www.opticsexpress.org/abstract.cfm?URI=oe-20-2-1733`.

[87] Benjamin Mills, James A Grant-Jacob, Matthias Feinaeugle, and Robert W Eason. Single-pulse multiphoton polymerization of complex structures using a digital multimirror device. *Optics express*, 21(12):14853–8, June 2013. ISSN 1094-4087. doi: 10.1364/OE.21.014853. URL `http://www.opticsexpress.org/abstract.cfm?URI=oe-21-12-14853`.

[88] Donald B Conkey, Albert N Brown, Antonio M Caravaca-Aguirre, and Rafael Piestun. Genetic algorithm optimization for focusing through turbid media in noisy environments. *Optics express*, 20(5):4840–9, March 2012. ISSN 1094-4087. doi: 10.1364/OE.20.004840. URL `http://www.opticsexpress.org/abstract.cfm?URI=oe-20-5-4840`.

[89] D Akbulut, T J Huisman, E G van Putten, W L Vos, and A P Mosk. Focusing light through random photonic media by binary amplitude modulation. *Optics express*, 19(5):4017–29, March 2011. ISSN 1094-4087. doi: 10.1364/OE.19.004017. URL `http://www.opticsexpress.org/abstract.cfm?URI=oe-19-5-4017`.

[90] Hasan Ylmaz, Willem L Vos, and Allard P Mosk. Optimal control of light propagation through multiple-scattering media in the presence of noise. *Biomedical optics express*, 4(9):1759–68, January 2013. ISSN 2156-7085. doi: 10.1364/BOE.4.001759. URL `http://www.pubmedcentral.nih.gov/articlerender.fcgi?artid=3771846&tool=pmcentrez&rendert`

[91] Martina Abb, Erik Bakkers, and Otto Muskens. Ultrafast Dephasing of Light in Strongly Scattering GaP Nanowires. *Physical Review Letters*, 106(14):143902, April 2011. ISSN 0031-9007. doi: 10.1103/PhysRevLett.106.143902. URL `http://link.aps.org/doi/10.1103/PhysRevLett.106.143902`.

[92] Otto Muskens, Paul Venn, Timmo van der Beek, and Thomas Wellens. Partial Nonlinear Reciprocity Breaking through Ultrafast Dynamics in a Random Photonic Medium. *Physical Review Letters*, 108(22):223906, May 2012. ISSN 0031-9007. doi: 10.1103/PhysRevLett.108.223906. URL `http://link.aps.org/doi/10.1103/PhysRevLett.108.223906`.